

K-band integral field spectroscopy and optical spectroscopy of massive young stellar objects in the Small Magellanic Cloud ^{*}

J.L. Ward¹†, J.M. Oliveira¹, J.Th. van Loon¹ and M. Sewiło²

¹*Physics and Astrophysics, Lennard-Jones Laboratories, Keele University, Keele, ST5 5BG, UK*

²*NASA Goddard Space Flight Center, 8800 Greenbelt Rd, Greenbelt, MD 20771, USA*

Accepted 2016 September 16. Received 2016 September 1; in original form 2016 April 28

ABSTRACT

We present *K*-band integral field spectroscopic observations towards 17 massive young stellar objects (YSOs) in the low metallicity Small Magellanic Cloud (SMC) and two YSO candidates in the compact H II regions N81 and N88 A (also in the SMC). These sources, originally identified using *Spitzer* photometry and/or spectroscopy, have been resolved into 29 *K*-band continuum sources. By comparing Br γ emission luminosities with those presented for a Galactic sample of massive YSOs, we find tentative evidence for increased accretion rates in the SMC. Around half of our targets exhibit emission line (Br γ , He I and H₂) morphologies which extend significantly beyond the continuum source and we have mapped both the emission morphologies and the radial velocity fields. This analysis also reveals evidence for the existence of ionized low density regions in the centre outflows from massive YSOs. Additionally we present an analysis of optical spectra towards a similar sample of massive YSOs in the SMC, revealing that the optical emission is photo-excited and originates near the outer edges of molecular clouds, and is therefore consistent with a high mean-free path of UV photons in the interstellar medium (ISM) of the SMC. Finally, we discuss the sample of YSOs in an evolutionary context incorporating the results of previous infrared and radio observations, as well as the near-infrared and optical observations presented in this work. Our spectroscopic analysis in both the *K*-band and the optical regimes, combined with previously obtained infrared and radio data, exposes differences between properties of massive YSOs in our own Galaxy and the SMC, including tracers of accretion, discs and YSO–ISM interactions.

Key words: Magellanic Clouds – stars: formation – circumstellar matter – infrared: stars – stars: protostars – H II regions.

1 INTRODUCTION

The formation of massive stars relies on the balance between mass loss and accretion (see Zinnecker & Yorke 2007 for a review). Both processes are heavily dependent on radiation pressure (Krumholz, Klein & McKee 2012), the effects of which depend on the dust content of the circumstellar medium. The metallicity of massive star forming regions is an important parameter to consider; the heat dissipation necessary to develop dense pre-stellar cores relies on radiation via the fine-structure lines of carbon and oxygen and

the rotational transitions of metallic molecules such as water and CO. Dust also plays a key role in massive star formation, driving the chemistry of molecular clouds, forming self-shielding dusty discs, and allowing continued accretion to form stars in excess of 10 M_⊙ (Kuiper et al. 2010). It is therefore expected that massive star formation is influenced by the initial conditions of the natal molecular cloud. However the effects of metallicity on massive star formation remain poorly understood with the majority of studies being carried out in Galactic, approximately solar metallicity environments. As a nearby (~60 kpc) gas-rich galaxy, the Small Magellanic Cloud (SMC) provides a valuable opportunity to study the formation of stars at lower metallicity ($Z_{\text{SMC}} \approx 0.2 Z_{\odot}$; Peimbert, Peimbert & Ruiz 2000) than in the Milky Way on both the scale of an entire galaxy and on the scale of individual stars.

^{*} Based on data obtained with SINFONI at the European Southern Observatory’s Very Large Telescope under programme 092.C-0723(A).

† E-mail: j.l.ward@keele.ac.uk

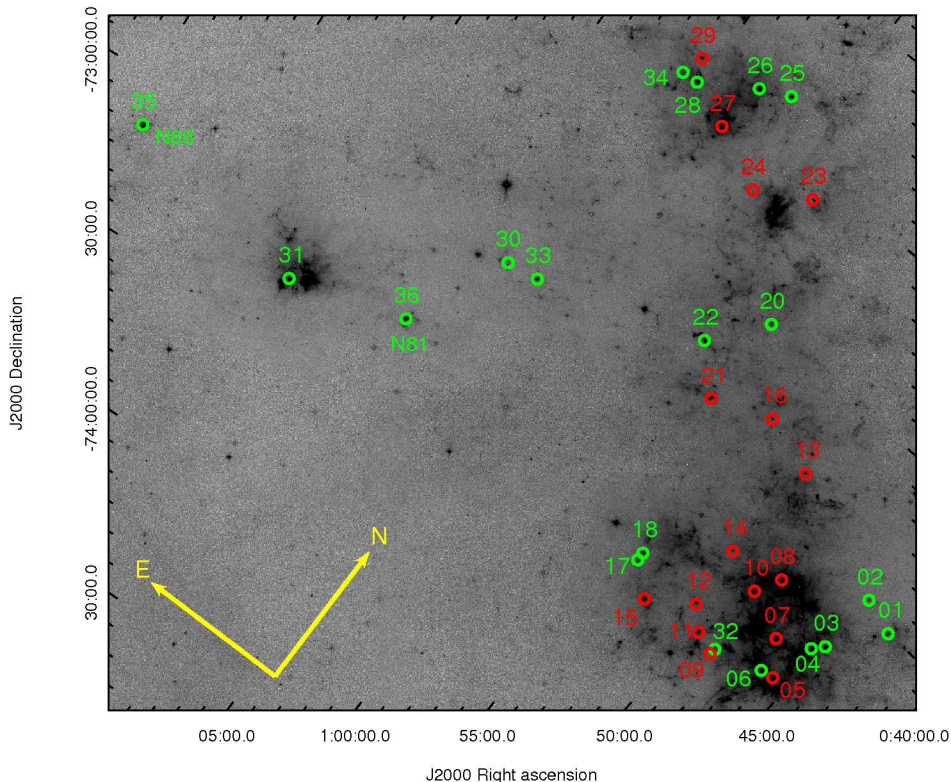


Figure 1. SAGE-SMC $8.0\ \mu\text{m}$ mosaic of the Small Magellanic Cloud (Gordon et al. 2011) showing the positions of all 33 spectroscopic massive YSOs presented in Oliveira et al. (2013) with the addition of sources #35 and 36. The sources observed with SINFONI are in green with the remaining sources marked in red. The H II regions N81 (#36) and N88 (#35) are also labelled.

The metallicity of a star forming region also has a profound effect on the structure and porosity of the interstellar medium (ISM). The lower dust abundance in low metallicity environments leads to a porous ISM and thus a larger mean free path length of UV photons (Madden et al. 2006; Cormier et al. 2015; Dimaratos et al. 2015) meaning that UV photons can permeate over longer distances and excite gas which lies farther from the source of the excitation. This in turn will have a significant effect on the feedback mechanisms we observe towards massive star forming regions as well as the formation of the stars themselves. Furthermore, the CO emission in the SMC is thought to arise only from high density clumps (Rubio et al. 2004) and the ISM in the similarly low metallicity galaxy NGC 1569 appears to be very clumpy (Galliano et al. 2003).

The “*Spitzer* Survey of the Small Magellanic Cloud” (S³MC, Bolatto et al. 2007) and the *Spitzer* “Surveying the Agents of Galaxy Evolution in the Tidally Stripped, Low Metallicity Small Magellanic Cloud” (SAGE-SMC, Gordon et al. 2011) survey have allowed the identification of a sample of YSO candidates in the SMC, Sewilo et al. (2013) identifying 742 high-reliability YSOs and 242 possible YSOs based on colour-magnitude cuts, visual inspection of multi-wavelength images and spectral energy distribution (SED) fits to near-IR and mid-IR photometry. A sample of 33 massive YSOs has been spectroscopically confirmed and studied by Oliveira et al. (2013); a brief overview of this analysis is provided in Section 2.

In order to determine whether massive YSO properties vary between the Milky Way and the Magellanic Clouds, we

will compare our results for massive YSOs in the SMC with those of the Red MSX¹ Source Survey (RMS Survey; Lumsden et al. 2013). The RMS survey provides the most comprehensive catalogue of massive YSOs and Ultra-Compact H II regions (UCHIIs) to date. *H*- and *K*-band infrared spectroscopy of a large sample of these objects has been carried out by Cooper et al. (2013) which we will use as a Galactic dataset to compare our results to. A similar analysis for a small sample of Large Magellanic Cloud YSOs in LHA120-N113 was performed in Ward et al. (2016) and is also included in our comparison.

In this work we present the *K*-band integral field spectroscopic observations of 17 previously confirmed YSOs and two YSO candidates in the compact H II regions N81 and N88 A in the SMC, obtained with SINFONI (Spectrograph for Integral Field Observations in the Near Infrared; Eisenhauer et al. 2003) at the European Southern Observatory’s (ESO) Very Large Telescope (VLT). We also present an analysis of previously obtained optical long slit spectroscopic observations of the H II regions surrounding our *K*-band targets (originally presented in Oliveira et al. 2013), obtained with the Double-Beam spectrograph (DBS) at the Australian National University Telescope. New spectroscopic data for N88 A and N81 from the Robert Stobie Spectrograph (RSS) at the Southern African Large Telescope (SALT) are also presented.

Section 2 summarises the results of previous observa-

¹ Midcourse Space Experiment (Egan et al. 2003)

tions towards our sources and Section 3 describes the SINFONI observations presented in this work and the data reduction procedure. The results of the SINFONI observations are presented in Section 4, with an analysis of the optical spectra in Section 5. Discussion and conclusions follow in Sections 6 and 7.

2 PREVIOUS OBSERVATIONS AND ANALYSIS

The majority of the *Spitzer* sources presented in this paper are a subset of the sample presented in Oliveira et al. (2013). They used the S³MC catalogue (Bolatto et al. 2007) and colour and flux cuts to select YSO candidates yielding 31 YSO candidates. Also added to the sample of Oliveira et al. (2013) were three YSOs identified serendipitously by van Loon et al. (2008) providing a total sample of 34 YSO candidates, all but one of which were spectroscopically confirmed as YSOs based on properties of *Spitzer* InfraRed Spectrograph (IRS) spectra. Oliveira et al. (2013) also presented ancillary optical spectra which we perform additional analysis for in Section 5.

A simplified and truncated version of Table 3 from Oliveira et al. (2013) is given in Table 1 of this paper, showing only those *Spitzer* YSOs for which SINFONI data were obtained. This table includes identified emission and absorption features based on *Spitzer* and ground-based data including ice absorption features as well as types based on the classification systems applied to LMC YSOs of Seale et al. (2009) and Woods et al. (2011). The S, P and O types by Seale et al. (2009) indicate spectra dominated by silicate absorption, Polycyclic Aromatic Hydrocarbon (PAH) emission and silicate emission respectively, whilst an E following the primary classification indicates the presence of fine structure emission. Note that the Seale et al. (2009) classification scheme does not consider the presence of ices, which are indicative of shielded colder regions and are thus expected to be found in early stage YSOs. The spectral types for YSOs from Woods et al. (2011)² are also based on the spectral features detected; ice absorption (G1), silicate absorption (G2), PAH emission (G3) and silicate emission (G4). Also included in Table 1 are the bolometric luminosities of the *Spitzer* sources obtained from SED fitting and whether or not radio emission is detected towards the source. Optical types are also given in Table 1 based on the identification of emission lines in the optical spectra presented in Oliveira et al. (2013); type evolution I to V represents an increase in the number of high excitation energy transitions detected.

Point source catalogues (Wong et al. 2011b, 2012) and high-resolution radio 20, 6 and 3 cm continuum images (Wong et al. 2011a; Crawford et al. 2011) of the SMC have shown that 11 of the 33 YSOs in Oliveira et al. (2013) exhibit radio continuum emission. Radio free-free emission is commonly detected towards UCHIIIs (e.g. Hoare et al. 2007) which are formed in the later stages of massive star formation. Of these 11 YSOs associated with radio emission, 7 are discussed in this work.

² The G1, G2, G3 and G4 notation used in this paper and in Oliveira et al. (2013) is equivalent to the YSO-1, YSO-2, YSO-3 and YSO-4 classes in Woods et al. (2011)

We have selected the subset of 17 spectroscopically confirmed YSOs from Oliveira et al. (2013) to form a sample of reasonable size which includes a wide variety of *Spitzer* classifications (Seale et al. 2009; Woods et al. 2011) in order to create a relatively unbiased sample. In addition to the 17 confirmed YSOs, we include in the sample two sources within the compact H II regions LHA 115-N81 and LHA 115-N88 A (Henize 1956; assigned the numbers 36 and 35, respectively in Table 1). Both of these regions have been previously studied and are known to be associated with young massive main sequence stars and massive star formation. The locations of all of the sources discussed in Oliveira et al. (2013) with the addition of sources #35 and 36 are marked on an 8.0 μ m mosaic of the SMC in Fig. 1.

N81, located in the Wing of the SMC was found by Koornneef & Israel (1985) to be relatively free of dust and excited primarily by a central bright star of spectral type O6. Heydari-Malayeri, Le Bertre & Magain (1988) characterised N81 as a young, compact H II “blob” with an extinction of $A_V = 1.4$ mag. N81 has been studied in the Far-UV (Heydari-Malayeri et al. 2002), confirming the presence of very young O-type stars in the H II region and with *JHK* imaging (Heydari-Malayeri et al. 2003) resolving the central region into two sources (which we now resolve into five individual components; Section 4.1).

Since its identification by Testor & Pakull (1985) as a high-excitation compact H II region, N88 A has become one of the best studied objects in the SMC and has been the subject of numerous imaging and spectroscopic studies (Roche, Aitken & Smith 1987; Kurt et al. 1999; Heydari-Malayeri et al. 1999; Testor, Lemaire & Field 2003; Testor et al. 2005, 2010; Martín-Hernández, Peeters & Tielens 2008). N88 A is a compact H II region ionized by four central stars with an H₂ emission shell approximately 3 arcsec in diameter. All four of these sources exhibit near-IR colours consistent with massive YSOs, but could also be consistent with reddened massive main sequence stars (Testor et al. 2010). N88 A appears to be an exceptionally bright high-excitation blob in the SMC and would rival many of the H II regions in the LMC in this respect (Charmandaris, Heydari-Malayeri & Chatzopoulos 2008).

Masers are one of the key phenomena associated with massive star formation; however, relatively few masers have been discovered in the SMC. Of particular interest are water masers, associated with outflows as observed in the earliest stage YSOs, and OH masers which are strongly associated with H II regions. Methanol masers also are one of the key tracers of massive star forming regions (Ellingsen 2006). To date six interstellar water masers have been detected towards the SMC (Scalise & Braz 1982; Oliveira et al. 2006; Breen et al. 2013), only one of which lies close enough to one of the sources from Oliveira et al. (2013), source #03, to possibly be associated with it. To date, no OH or methanol masers have been detected in the SMC (van Loon 2012).

3 OBSERVATIONS AND DATA REDUCTION

3.1 SINFONI *K*-band spectroscopy

K-band integral field spectroscopic observations were carried out for 19 *Spitzer* YSO targets in the SMC using SINFONI at the VLT under program 092.C-0723(A) (PI: Joana

Table 1. Previously known properties of YSOs in the SMC from Oliveira et al. (2013), truncated to show only the YSOs observed with SINFONI. The presence or absence of a feature is indicated by ✓ and ✗, ? indicating doubt. Silicate emission is identified with \wedge . For H₂ emission, ✓/? indicates objects for which only two emission lines were detected in the *Spitzer*-IRS range, rather than three to five. Also shown are the detections of either H₂O or CO₂ ice features at 3 μ m and 15.2 μ m, respectively. The optical ionization classes are defined according to the emission lines present in the spectrum: Type I objects exhibit Balmer, Paschen and O I, Type II objects show hydrogen, O I, [N II], [O II] and [S II] emission, Type III objects show the same lines plus [O III], Type IV objects further add [S III] and finally Type V objects show all these lines plus He I emission. Some objects exhibit a stellar absorption spectrum and others only H α in emission (see Oliveira et al. 2013 for discussion). The following column indicates whether the object has been detected at radio wavelengths; * signals an extended source. The sources are classified using features in their IRS spectrum, according to two classification schemes previously applied to samples of LMC YSOs (Seale et al. 2009; Woods et al. 2011). The last column provides the luminosities determined from the SED fits. See Section 2 for further information.

#	PAH emission	Silicate	H ₂ emission	H ₂ O/CO ₂ ice 3 μ m / 15.2 μ m	Optical type	Radio source	YSO class.		L (10 ³ L _☉)
							S09	W11	
01	✓	✗	✓	✗	IV/V	Y	PE	G3	16
02	✓	✓	✓	✓	Only H α emission	Y	S	G1	19
03	✓	✓	✓?	✓	V	Y	S	G1	61
04	✓	✗	✓	✗	II	N	P	G3	2.3
06	✓	✓	✓	✓	Absorption lines	N	S	G1	5.8
17	✓	✓	✓?	✓	Only H α emission	N	S	G1	22
18	✗	✓	✗	✓	Only H α emission	N	S	G1	28
20	✓	\wedge	✓?	✗	I	N	O	G4	1.5
22	✓	✗	✓	✓	IV/V	N	PE	G1	9.1
25	✓	✗	✓	✗	IV	Y	P	G3	17
26	✓	✗	✓	✗	V	Y	PE	G3	12
28	✓	✓	✓?	✗	IV/V	Y	S	G2	140
30	✓	✓?	✓	✓	I	N	P	G1	7.9
31	✓	✗	✓?	✗	No spectrum	Y*	PE	G3	6.7
32	✓	✓	✓	✓	I/II	N	S	G1	3.5
33	✓	✓	✓?	✗	I/II	N	S	G2	26
34	✓	✓	✓?	✓	Only H α emission	N	S	G1	23

Oliveira). Each object was observed with a minimum of four 300 second integrations along with sky offset position observations in an ABBA pattern with jittering. Telluric B-type standard stars were also observed at regular intervals throughout each night in order to provide standard star spectra for telluric correction and flux calibration. Dark, flat lamp, arc lamp and fibre calibration frames were observed during the daytime and linearity lamp frames were obtained from the ESO archive. Observations were carried out with a 0.1 \times 0.05 arcsec spatial scale, providing a 3.2 \times 3.2 arcsec field-of-view (FOV) for the spectral range 1.95–2.45 μ m and with a spectral resolving power of $\lambda/\Delta\lambda = 4000$, yielding a velocity resolution of ~ 70 km s⁻¹ (and therefore allowing the determination of Gaussian centroid positions to < 4 km s⁻¹). Where possible the adaptive optics (AO) module was used. For sources #17, 18 and 22 we were not able to use AO, yielding a seeing limited spatial resolution for these sources (useful morphological information was still obtained).

The raw data were reduced using the standard SINFONI pipeline recipes in GASGANO. Telluric and flux calibration were performed simultaneously for each cube using an IDL script. For each pixel in the target cube, the target spectrum is divided through by the telluric spectrum removing the telluric spectral features. The target spectrum was then multiplied by a blackbody with a temperature appropriate for the spectral type of the standard star used. The blackbody spectra used in this calibration were generated

using PYRAF³. This process was looped to apply the same procedure to each spatial pixel (spaxel) in the cube.

SINFONI is a Cassegrain focus mounted instrument and as such it does suffer from a systematic time-dependent wavelength shift during each night due to flexure. This is always small (less than 3 resolution elements) so it only presents an issue when determining accurate absolute centroid velocity measurements. In order to account for this effect, a second wavelength calibration was performed on the final data cubes using the OH emission lines in the sky data cubes produced in the SINFONI pipeline.

Although sky line subtraction does form part of the standard SINFONI data reduction pipeline, due to the relatively long observing times in this study (8 \times 5 minute exposures plus overheads), the variation in sky line intensities leads to sky line residuals remaining in the final data cubes. The positions of these lines are shown in Ward et al. (2016; Fig. B2). Whilst aesthetically displeasing, the impact of these residuals on the spectral analysis is actually small as none are coincident with any emission lines of interest and the continuum measurements are calculated from models fitted to the continuum so noise and residuals are not an issue.

For source #25 the data reduction sequence has yielded a data cube which exhibits negative continuum flux towards the red end of the spectrum. On inspection of the sky cube this appears to be caused by an unusually strong, red contin-

³ PYRAF is a product of the Space Telescope Science Institute, which is operated by AURA for NASA.

uum in the sky frames most likely caused by contamination from a red continuum source nearby (see Fig. C1 in Oliveira et al. 2013). Whilst this has made continuum flux measurements of source #25 unusable, it is unlikely to have affected the measurements of emission lines towards the source.

Following the data reduction we applied a process of re-sampling, Butterworth spatial filtering and instrumental fingerprint removal following the procedure outlined in Menezes, Steiner & Ricci (2014) and Menezes et al. (2015). First re-sampling was carried out with a 2×2 rebin and a cubic spline interpolation. This introduces a high spatial-frequency component which can be removed using Butterworth Spatial Filtering (BSF; Gonzalez & Woods 2002) through the following steps.

- Calculation of the Fourier transform of the image, $F(u, \nu)$.
- Multiplication of the Fourier transform by the corresponding Butterworth filter, $H(u, \nu)$.
- Calculation of the inverse Fourier transform of the product $F(u, \nu) \cdot H(u, \nu)$.
- Extraction of the real part of the calculated inverse Fourier transform.

Menezes et al. (2015) determined that a squared circular filter is most appropriate for K -band SINFONI data at the 100 mas pixel scale;

$$H(u, \nu) = \left\{ 1 + \left[\sqrt{\left(\frac{u - u_0}{a}\right)^2 + \left(\frac{\nu - \nu_0}{b}\right)^2} \right]^{2n} \right\}^{-2} \quad (1)$$

where $n=2$ and $a=b=0.26 N_y$ (where N_y is the number of spaxels in the vertical direction).

The final stage of our truncated version of the data treatment procedure of Menezes et al. (2015) is instrumental fingerprint removal using Principal Component Analysis (PCA) as summarised in the following steps.

- All spectral lines are fitted and removed from the input data cube using Gaussian line profiles. The average pixel value for each slice, Q_λ is then subtracted from every pixel in that slice.
- The 3D datacube, D_0 is converted into a two dimensional array, I ; $I[\beta, \lambda] = D_0[i, j, \lambda]$ where $\beta_{i,j} = \mu(i - 1) + j$ and μ is equal to the number of elements in the first dimension.
- Application of PCA tomography to the 2D matrix as outlined in Steiner et al. (2009). This yields the 2D tomogram matrix, T , and the eigenvector matrix, E .
- Selection of the eigenvectors related to the instrumental fingerprint. This is done by eye on the basis that the spectral signature will be that of the fingerprint and that the corresponding tomogram must have a spatial morphology including a large horizontal stripe at the bottom of the image (see Menezes et al. 2015 for details).
- Reconstruction of the datacube, excluding the eigenvector and tomogram related to the instrumental fingerprint; $I_{out} = \sum_k T_{\beta,K} \cdot [E_{\lambda,K}]^T$ for $K \neq K_{inst}$.
- The 2D array is converted back into a data cube and the properties subtracted in the first step are now added back in; $D_{out} = I_{i,j,\lambda} + \text{emission lines} + Q_\lambda$.

The total flux is conserved through this process within a fraction of a percent. Whilst this procedure does not improve

the spatial resolution nor change the observed morphologies and kinematics, it does provide cleaner intensity and velocity maps.

1D spectra were extracted using GASGANO for each of the detected continuum sources in the final data cubes. Emission lines detected in these spectra were fitted with a Gaussian profile using the Starlink spectral analysis package SPLAT. The measured emission line fluxes are listed in Table C1.

3.2 RSS optical spectroscopy

In addition to the DBS optical spectra first presented in Oliveira et al. (2013), optical spectra have been obtained for sources #35 (N88 A) and 36 (N81) using the Robert Stobie Spectrograph (RSS; Kobulnicky et al. 2003) at the Southern African Large Telescope (SALT; Buckley, Swart & Meiring 2006) under program 2014-1-UKSC-003 (PI: Jacob Ward) and these are also presented here (shown in Figs. B2, B3 and B4). The optical spectra for N81 and N88 A were obtained using both the pg900 grating centred at 6318.9 Å to obtain a broad band low resolution spectrum for each source and the pg1800 grating centred on the positions of H α and H β to obtain medium resolution spectra for these regions. A slit width of 1 arcsec was used for all RSS spectroscopy presented here whilst the slit width used to obtain the DBS spectra was 2 arcsec.

The RSS spectra were reduced using the data reduction package FIGARO for flat field correction, extraction and wavelength calibration. Flux calibration was carried out using standard stars observed with RSS within one month of the observations.

4 RESULTS

4.1 Continuum emission and photometry

For each spaxel in the final flux calibrated cubes, the continuum was fitted and summed for the spectral region spanning 2.028–2.290 μm to produce continuum flux maps without any contribution from line emission. The J2000 RA and Dec positions of each K -band continuum source resolved in this work are given in Table 2. The positions of each continuum source are marked in Fig. A1, the green circles show the regions from which 1D spectra were extracted from the cubes. Values for the K -band apparent magnitude (using the CIT photometric system where the K -band zero point is at 620 Jy) of each of the sources were determined by fitting a polynomial to the continuum of the 1D spectrum for each source and summing the total flux of the fitted continuum (Table 2).

Out of 19 observed sources, 14 consist of a single continuum source at the resolution obtained with this study (0.1–0.2 arcsec with AO and ~ 0.6 arcsec seeing limited), whilst the remaining five targets consist of multiple continuum sources. Sources #02, 22 and 28 are resolved into two components whilst sources #35 and 36 are resolved into four and five K -band continuum components, respectively (see Table 2 & Fig. A1).

Table 2. Positions of each of the K -band continuum sources as determined from the SINFONI continuum images, and the K -band apparent magnitude for each source with the visual extinction value determined from the ratio between the 1-0Q(3) and 1-0S(1) H_2 emission lines.

Source	J2000		K (mag)	A_V (mag)
	RA (h:m:s)	Dec ($^{\circ}$: $'$: $''$)		
01	00:43:12.885	-72:59:58.18	16.1 ± 0.01	2.6 ± 10.9
02 A	00:44:51.878	-72:57:33.81	15.14 ± 0.01	9.3 ± 8.7
02 B	00:44:52.094	-72:57:34.06	15.75 ± 0.01	4.3 ± 24.4
03	00:44:56.571	-73:10:14.37	13.51 ± 0.01	13.7 ± 10.8
04	00:45:21.283	-73:12:18.39	14.52 ± 0.01	
06	00:46:24.348	-73:22:06.47	17.51 ± 0.02	7.2 ± 6.4
17	00:54:02.269	-73:21:19.02	15.87 ± 0.01	47.5 ± 10.0
18	00:54:03.277	-73:19:39.12	15.88 ± 0.01	18.7 ± 10.1
20	00:56:06.411	-72:28:27.62	15.96 ± 0.01	24.1 ± 13.2
22 A	00:57:56.959	-72:39:16.14	15.96 ± 0.01	9.9 ± 6.4
22 B	00:57:57.182	-72:39:15.54	17.6 ± 0.01	22.5 ± 16.6
25	01:01:31.678	-71:50:38.48		<12.0
26	01:02:48.441	-71:53:17.15	16.68 ± 0.03	14.2 ± 16.6
28 A	01:05:07.229	-71:59:42.54	14.98 ± 0.01	19.5 ± 9.3
28 B	01:05:07.315	-71:59:41.85	17.63 ± 0.01	25.2 ± 12.5
30	01:06:59.656	-72:50:42.82	14.22 ± 0.01	13^{+55}_{-25}
31	01:14:39.284	-73:18:28.21	15.08 ± 0.02	1.5 ± 7.9
32	00:48:39.662	-73:25:00.69	14.66 ± 0.01	22.2 ± 22.1
33	01:05:30.015	-72:49:51.90	11.5 ± 0.01	<5.0
34	01:05:49.349	-71:59:48.59	14.12 ± 0.01	16.0 ± 8.0
35 A	01:24:07.982	-73:09:03.81	13.47 ± 0.04	1.2 ± 17.0
35 B	01:24:07.901	-73:09:03.66	14.65 ± 0.06	<22.5
35 C	01:24:07.867	-73:09:04.36	14.85 ± 0.08	<10.1
35 D	01:24:07.982	-73:09:03.06	14.91 ± 0.06	$1.8^{+12.0}_{-15.8}$
36 A	01:09:12.912	-73:11:38.53	14.93 ± 0.01	<32.5
36 B	01:09:12.889	-73:11:38.28	15.48 ± 0.01	13.3 ± 12.8
36 C	01:09:13.212	-73:11:38.68	16.08 ± 0.01	21.6 ± 32.5
36 D	01:09:13.131	-73:11:38.68	16.54 ± 0.01	35.3 ± 23.3
36 E	01:09:12.693	-73:11:38.58	16.56 ± 0.02	19.9 ± 21.1

4.2 Extinction

In order to calculate values of extinction towards our sources, we utilise the H_2 lines in the extracted spectra. The 1-0S(1) / 1-0Q(3) flux ratio (I_{S1}/I_{Q3} in equation 2) is used due to its insensitivity to temperature and relatively large wavelength separation (e.g., Davis et al. 2011). Visual extinction is given by:

$$A_V = -114 \times \log(0.704[I_{S1}/I_{Q3}]) \quad (2)$$

Extinction corrections were calculated for each emission line individually using the Galactic mean R_V dependent extinction law:

$$[A(\lambda)/A(V)] = a(x) + b(x)/R_V \quad (3)$$

where $x = 1/\lambda$, $a(x) = 0.574x^{1.61}$ and $b(x) = -0.527x^{1.61}$ for the K -band (Cardelli, Clayton & Mathis 1989). An R_V value of 3.1 has been adopted although R_V has been found to range from 2.05 ± 0.17 to 3.30 ± 0.38 in the SMC (Gordon et al. 2003).

The calculated extinction values using this method are given in the final column of Table 2. We find that the mean extinction value towards the SMC sources (excluding limits and null values) presented here is $A_V = 15.8 \pm 3.3$ mag, significantly lower than the average towards 139 Galactic massive YSOs obtained from HK photometry (45.7 ± 1.5 mag; Cooper et al. 2013) and that of N113 in the LMC (22.3 ± 3.8 mag; Ward et al. 2016). Furthermore, the median values for extinction are $A_V = 43.8$, 20.0 and 14.2 mag for the Galactic sample, the N113 sample and the SMC sample, respectively. This is consistent with the lower dust to gas ratio in the

SMC and suggests that extinction scales with metallicity. It should be noted that N113 may not be representative of the LMC (see Ward et al. 2016).

4.3 K -band emission features

4.3.1 $H1$ emission

$Br\gamma$ emission ($2.166 \mu\text{m}$) is most commonly associated with accretion in star formation studies. For intermediate mass YSOs the relation from Calvet et al. (2004) can be used to estimate the accretion luminosity from $Br\gamma$ luminosity:

$$\log(L_{\text{acc}}) = -0.7 + 0.9(\log(L_{Br\gamma}) + 4) \quad (4)$$

It is possible that this relation breaks down for massive stars due to an additional emission component originating from the strong stellar winds associated with hot stars. Furthermore, Herbig Be stars do not appear to be modelled successfully through magnetospheric accretion, suggesting a change of accretion mechanism at high masses (e.g., Fairlamb et al. 2015). For the purposes of comparing our sample with a Galactic sample, however, the above relation can be applied to gain an equivalent accretion luminosity assuming that both samples cover the same range of evolutionary states and YSO masses. The models of Kudritzki (2002) make the prediction that the effect of metallicity on the production of photons capable of ionizing hydrogen is almost negligible due to the cancelling effect of metal line blocking and metal line blanketing, and thus the lower metallicity of the SMC should not affect this relationship.

$Br\gamma$ emission is detected towards 28 of the 29 SINFONI K -band sources observed in this work, making it the most common spectral feature in the data set. Only the spectrum towards source #02 B does not exhibit $Br\gamma$ emission. Figure 2 shows the extinction corrected $Br\gamma$ luminosities plotted against absolute K -band magnitude for all sources where $Br\gamma$ was detected. Also included in this plot are the results of Cooper et al. (2013) and Ward et al. (2016) for YSOs in the Milky Way and N113 in the LMC, respectively, along with extinction tracks which show the allowed positions of points in the diagram based on the uncertainty of the extinction correction (see Table 2).

Akritas-Theil-Sen (ATS; Akritas, Murphy & Lavalley 1995) regressions were fitted to the SMC sample and the Galactic sample. The ATS regressions and Kendall's τ values were computed in the R-project statistics package using the CENKEN function from the NADA library (Helsel 2005). The ATS regression fit takes the form $y = 10^{ax+b}$; we compute the values of $a_{SMC} = -0.39$ and $b_{SMC} = -2.46$ for the SMC sample whilst the Galactic sample yielded values of $a_{MW} = -0.37$ and $b_{MW} = -2.69$. The associated Kendall's τ values are $\tau_{SMC} = -0.50$ and $\tau_{MW} = -0.70$ for the SMC and the Cooper et al. (2013) samples respectively, indicating a stronger correlation for the Galactic sample than for the SMC sample. The p values, which represent the likelihood of there being no correlation between $L_{Br\gamma}$ and K -band magnitude, are 0.0004 and $<1 \times 10^{-8}$ for the SMC and Galactic samples respectively, indicative of a definite correlation for both sets of data.

Whilst consistent with the Galactic sample, our sample of SMC sources exhibit $Br\gamma$ emission luminosities that are high for their absolute K -band magnitudes compared

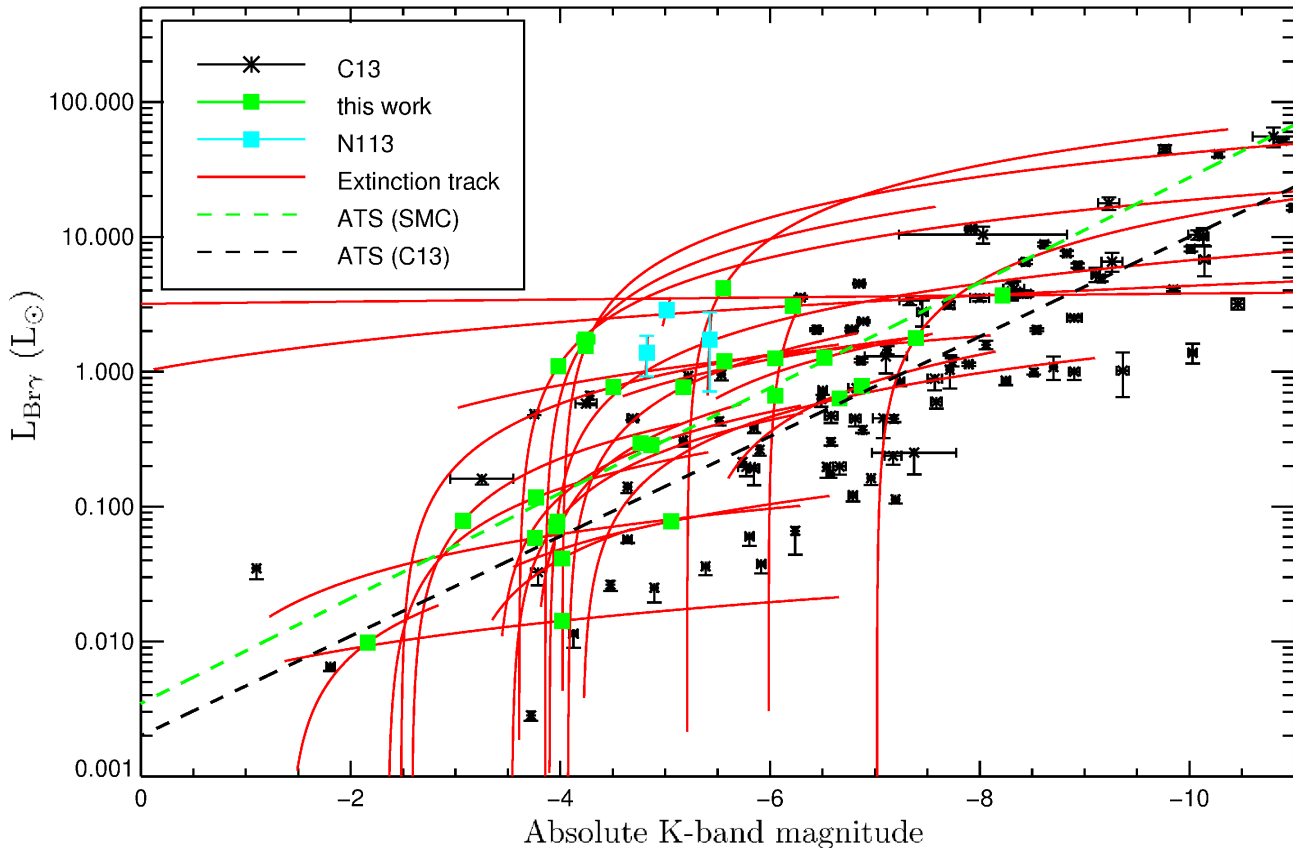


Figure 2. Br γ luminosity against absolute K -band magnitude. Data from Cooper et al. (2013) and Ward et al. (2016) are also included for comparison, labelled as C13 and N113, respectively. The red extinction tracks are representative of the uncertainty due to the extinction correction (Table 2). The green and black dashed lines indicate the ATS regressions fitted to the SMC and the Cooper et al. (2013) sources respectively.

with the Cooper et al. (2013) data. Not accounting for any difference in the K -band continuum emission or additional sources of excitation, assuming that Eqn. 4 holds true this suggests that YSOs in the SMC exhibit higher accretion rates than their counterparts in the Milky Way causing higher levels of Br γ emission. This is discussed in detail in Section 6.1.

In the majority of sources, the Br γ emission is compact but in 7 of the 19 FOVs we see evidence of extended H I emission as shown in Fig. 3. In sources #01, 28 and 35 (N88 A) it extends roughly symmetrically from a central continuum source whilst in sources #03 and 31 it is extended over a significant area and offset to one side of a continuum source. Source #28 also exhibits weak elongated Br γ emission extending to the south of the continuum source (Fig. 3, red contour). Source #02 exhibits relatively compact and collimated extended Br γ emission in one direction from the continuum source. Finally for source #36 (N81), there appears to be relatively high levels of ambient Br γ emission which is unsurprising given the nature of the N81 H II region (see Section 2). The extended Br γ emission to the west most likely originates outside the FOV as the peak of the emission is at the edge of the observed region whilst that in the east appears to be associated with (or have a component associated with) source #36 C and possibly #36 D.

In addition to analysing Br γ emission morphologies and

fluxes, the centroid velocity of the emission has also been calculated using the centroid of the Gaussian profile fitted to the emission line at every spaxel to create velocity maps. Figure 4 shows the Br γ centroid velocity maps for sources #01, 02, 03, 28, 35 and 36 relative to the brightest K -band continuum source in each field. Sources #02 and 28 exhibit similar velocity fields surrounding the continuum source with no clear gradient in Br γ emission velocity; to the south of source #28 the weak, elongated Br γ component (red contour in Fig. 3 and black contour in Fig. 4) appears to be red-shifted with respect to the continuum source by 5–10 km s $^{-1}$. For sources #01 and 35 the velocity maps show velocity gradients of 5–10 km s $^{-1}$ which are consistent with an expanding ionized medium surrounding the continuum sources. Source #03 exhibits a wide extended and blue shifted region of Br γ emission. The map of source #36 shows a significant velocity gradient across the FOV; however, it remains unclear whether this is directly influenced by the continuum sources or whether it is more representative of larger scale motions of ionized gas in the region. Sources #36 C and 36 B appear in regions of Br γ emission which are slightly blue shifted with respect to the emission towards 36 A. Although Br γ emission is extended in source #31, the signal-to-noise ratio is not sufficient to map the velocity field of the emitting gas.

The Pfund series (between 2.37 μ m and 2.44 μ m) has only been detected and measured towards sources in #35,

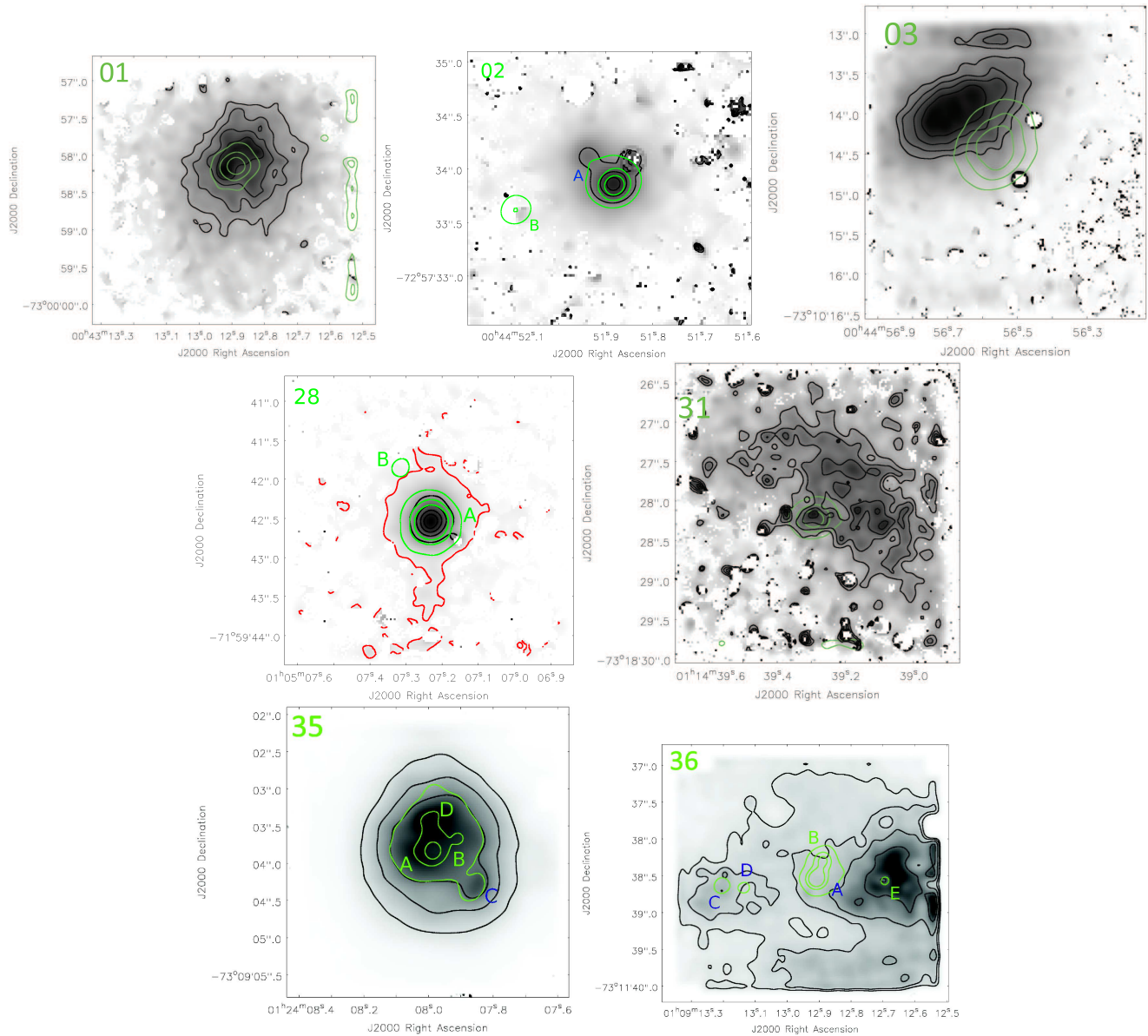


Figure 3. Extended Br γ emission line morphologies for sources #01, 02, 03, 28, 31, 35 (N88 A) and 36 (N81). Black contours - $[0.2, 0.4, 0.6, 0.8] \times$ maximum Br γ 2.1661 μm integrated flux, green contours - $[0.25, 0.5, 0.75] \times$ maximum continuum integrated flux. The red contours in source #28 indicate significantly weaker ($4 \times 10^{-22} \text{ Wm}^{-2}/\text{spaxel}$), more extended Br γ emission.

the compact H II region N88 A. However due to the relatively large uncertainties in extinction towards N88 A and the poor signal-to-noise (S/N) in this region, physical properties cannot be determined from the Pfund emission.

4.3.2 He I emission

He I emission is produced from the ionization and subsequent recombination of helium atoms, a significant process at the ionization boundary of H II regions and potentially also in areas of collisional excitation (Porter, Drew & Lumsden 1998). The strongest and most commonly detected helium emission line in the K -band towards massive YSOs is the 2.059 μm line produced by the $2^1\text{P}^0 - 2^1\text{S}$ transition. This emission line has been detected towards 15 of our K -band

continuum sources, nine of which lie in the FOVs of targets #35 and 36 (N88 A and N81, respectively).

Figure 5 plots the He I 2.059 μm emission line luminosity against the absolute K -band luminosity, analogous with Fig. 2. Also included are the results for Galactic sources from Cooper et al. (2013) and those for sources in N113 in the LMC from Ward et al. (2016). Despite the large uncertainties originating in the extinction calculation, it certainly appears that all of the He I fluxes fall within the range observed in the Milky Way and in N113 in the LMC. This suggests that the mechanism causing the increased Br γ emission in the SMC does not appear to affect the He I emission in the same way. Furthermore the ATS regressions fitted to these data also suggest no significant increase is seen in the He I fluxes towards the SMC compared to the Galactic sample. Using the form $y = 10^{ax+b}$, we find values of

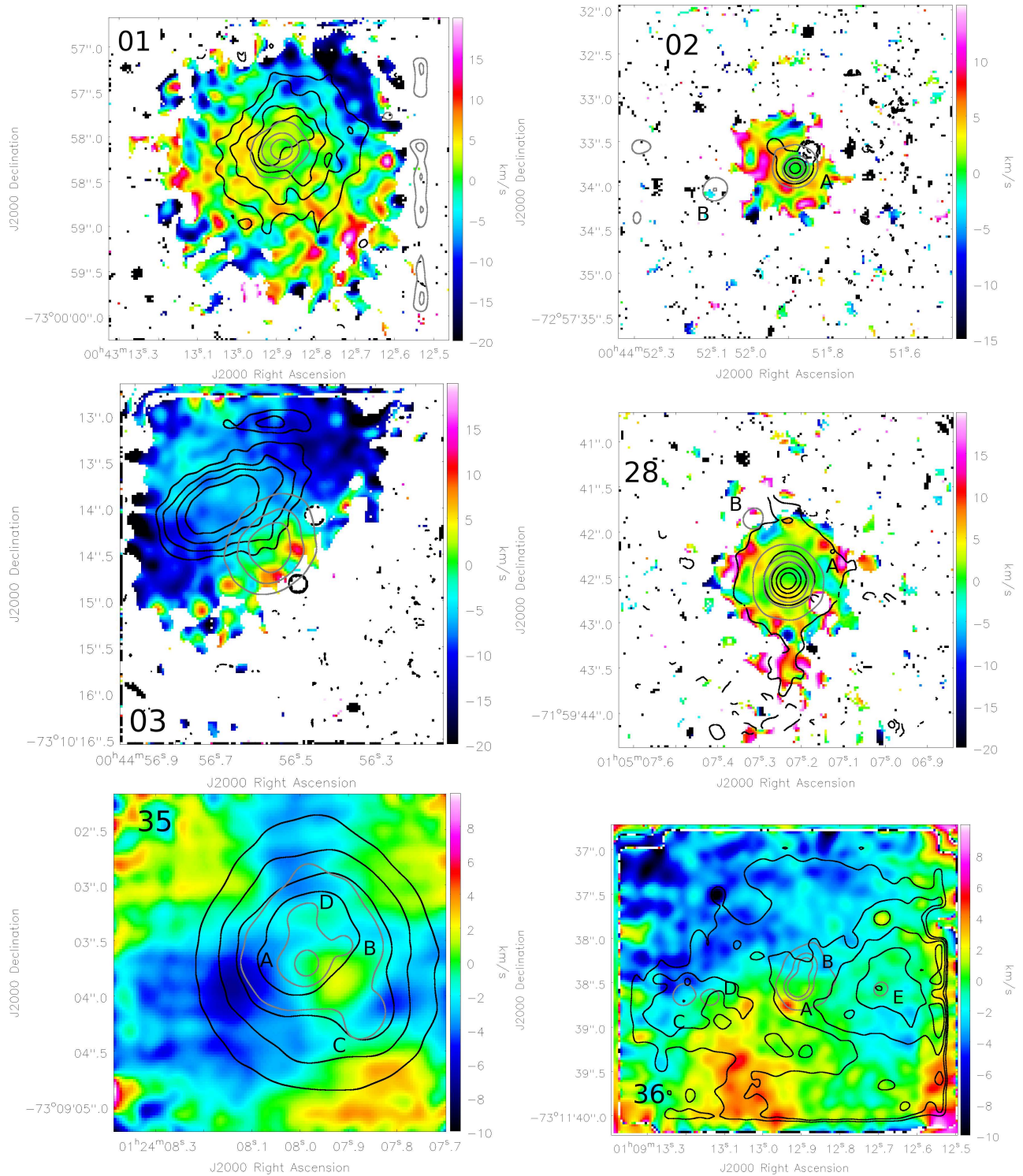


Figure 4. Br γ centroid velocity maps for sources #01, 02, 03, 28, 35 and 36. Black contours - Br γ 2.1661 μm integrated flux, grey contours - continuum flux (see Fig. 3). The black contours in source #28 trace the same emission as the black and the red contours in Fig. 3. Velocities are relative to that measured towards the brightest continuum source in the FOV.

$a_{\text{SMC}} = -0.41$ and $b_{\text{SMC}} = -3.25$ for the SMC data and $a_{\text{MW}} = -0.40$ and $b_{\text{MW}} = -3.19$ for the sample of Cooper et al. (2013). Again, we find a stronger correlation for the Galactic sources than the SMC sources with $\tau_{\text{SMC}} = -0.48$ whilst $\tau_{\text{MW}} = -0.78$. Similarly the probability of a correlation is higher in the Galactic sample with values of

$p_{\text{SMC}} = 0.03$ and $p_{\text{MW}} = 9 \times 10^{-7}$, indicating probabilities that the magnitude and He I luminosities are correlated of 97% and >99% for the SMC and the Milky Way, respectively.

The morphology and kinematics of the He I 2.059 μm emission has been mapped for five sources for which the

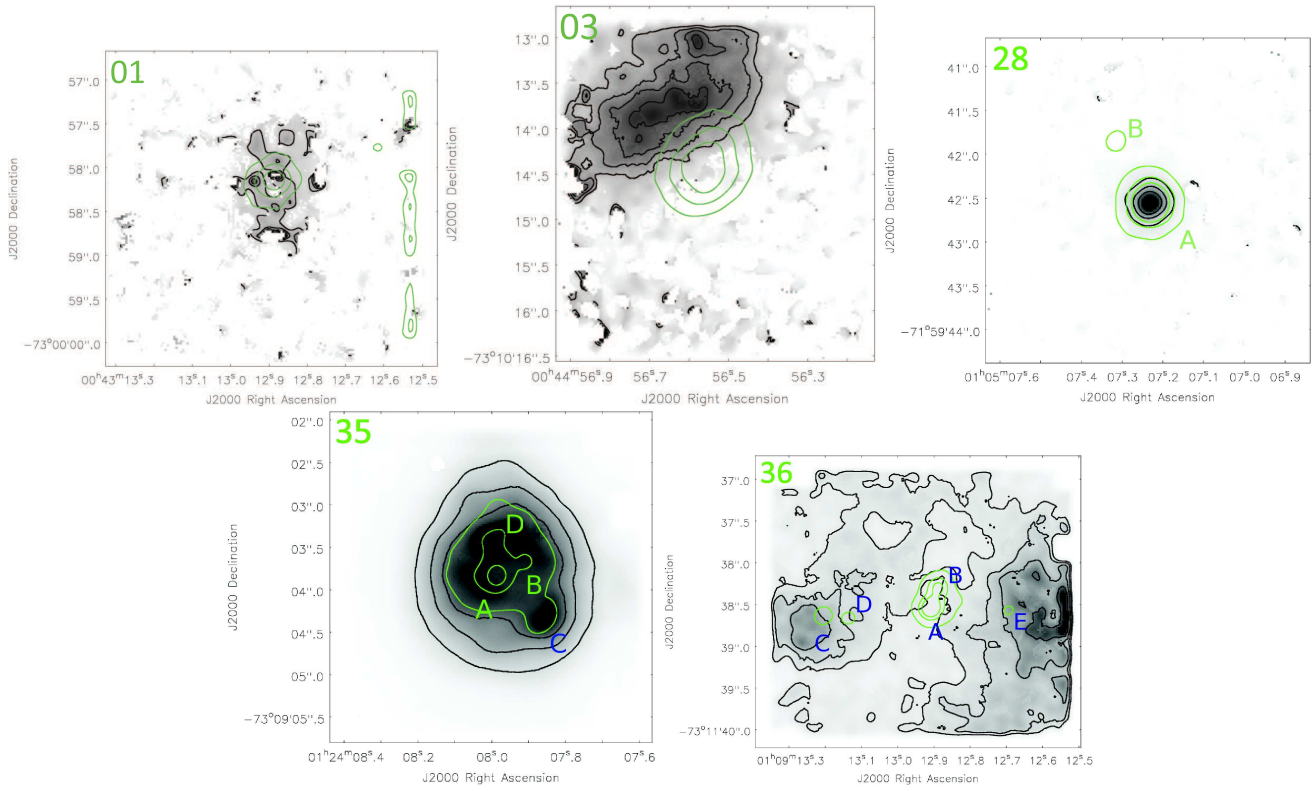


Figure 6. He I emission line morphologies for sources #01, 03, 28, 35 and 36. Black contours - $[0.2, 0.4, 0.6, 0.8] \times$ maximum He I $2.059 \mu\text{m}$ integrated flux, green contours - continuum flux. The continuum contour levels are as in Fig. 3.

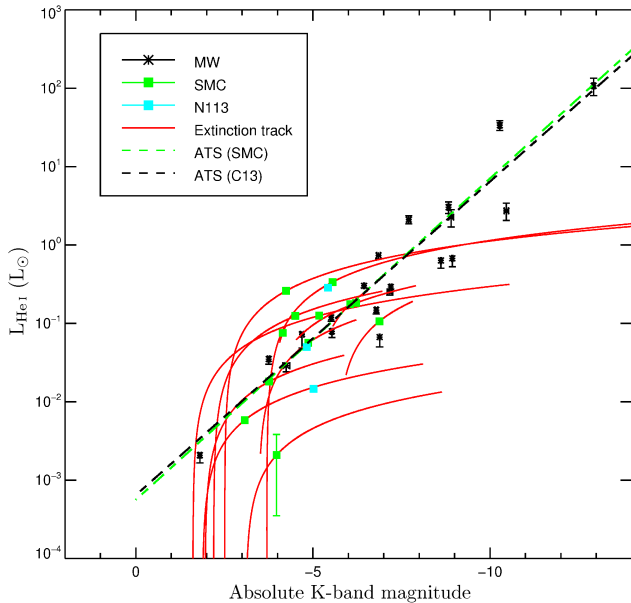


Figure 5. He I luminosity versus absolute K -band magnitude. See also caption for Fig. 2.

S/N was adequate to do so (Figs. 6 and 7). For the most part the He I emission traces the same morphological structures as the Br γ emission. For sources where line velocities could be reliably measured (#03, 28, 35, 36), the He I velocity maps trace the same velocity structures as the Br γ maps. Both the morphologies and kinematics measured support a

common physical origin of Br γ and He I emission for these four sources. The exception is source #28 A which does not exhibit the same southwards narrow jet-like structure in He I emission as in the Br γ emission.

4.3.3 H_2 emission

Molecular hydrogen emission lines in the K -band are a commonly used tracer of both shocked emission from outflows and of photo-dissociation regions (PDRs). We detect the H_2 1-0S(1) and 1-0Q(3) emission lines towards all but one of our sources (#04) whilst the remaining detected H_2 emission lines (1-0S(0), 1-0S(2), 1-0S(3), 2-1S(0), 2-1S(1), 2-1S(2), 1-0Q(1), 1-0Q(2); wavelengths are listed in Table 3) have lower rates of detection. The full list of H_2 emission line fluxes is given in Table C1, and in Fig. 8 we have plotted H_2 $2.1218 \mu\text{m}$ luminosity against that of Br γ emission. We find that the H_2 emission dominates (significantly exceeds the Br γ luminosity, $H_2/\text{Br}\gamma > 1.3$) in seven of our sources (#06, 18, 22 A, 22 B, 26, 28 B, 31) and that six sources lie close to the $H_2 = \text{Br}\gamma$ line ($H_2/\text{Br}\gamma > 0.6$; #01, 02 A, 03, 17, 28 A, 34). The remaining sources for which we measure both H_2 emission and Br γ emission appear to be dominated by Br γ emission ($H_2/\text{Br}\gamma < 0.35$).

Through comparison with grids of models simulating H_2 emission from both shock excitation and photo-excitation, it is possible to distinguish between these excitation mechanisms using the flux ratios between different emission lines. Table 3 shows the extinction corrected intensity ratios of all of the measured H_2 emission lines relative to the 1-0S(1) line with the exception of the Q-branch emission lines. Also in-

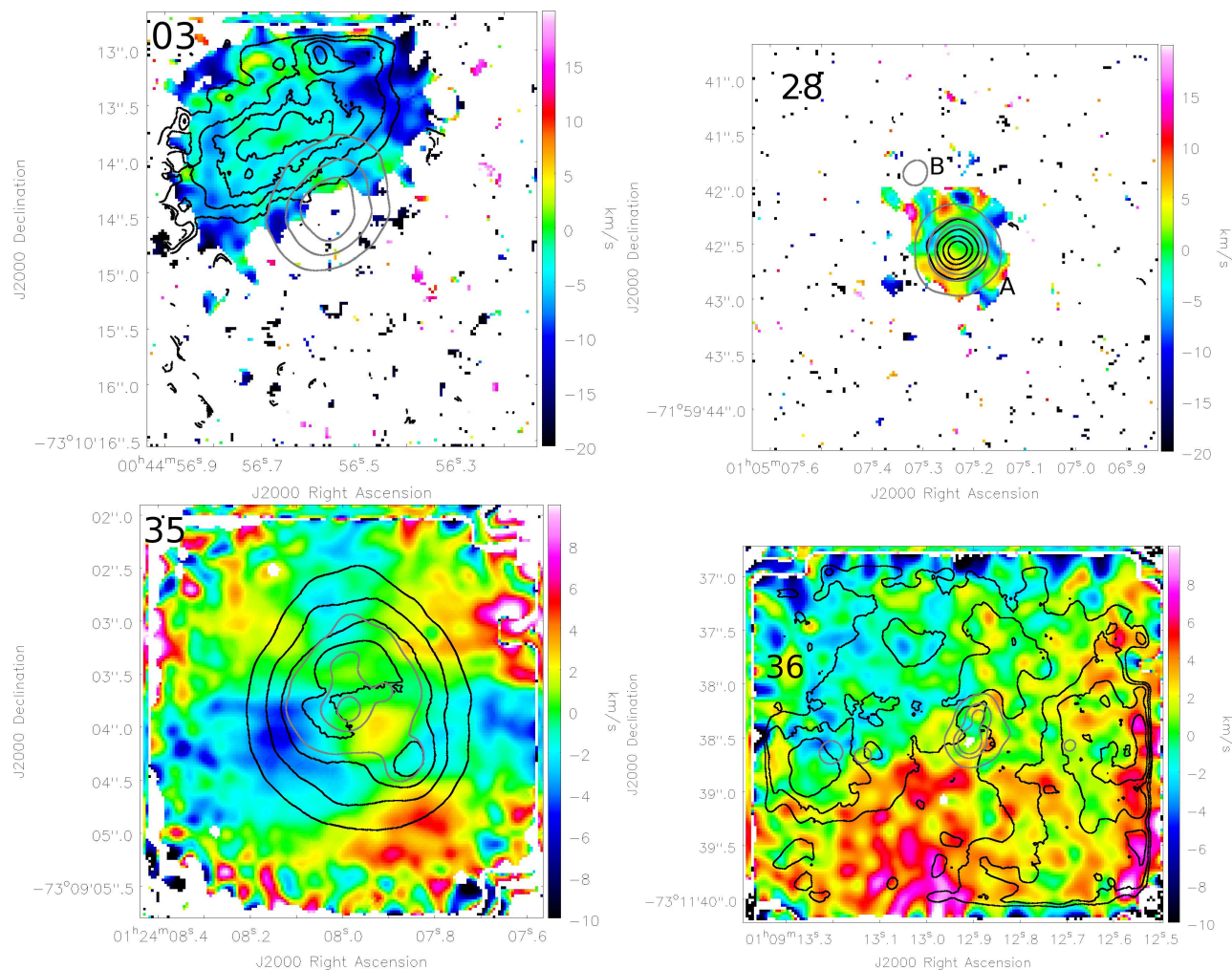


Figure 7. He I centroid velocity maps for sources #03, 28, 35 and 36. Black contours - He I $2.059 \mu\text{m}$ integrated flux, grey contours - continuum flux. See also the caption of Fig. 4. Velocities are relative to that measured towards the brightest continuum source in the FOV.

cluded are the model line ratios for photo-excitation (Black & van Dishoeck 1987) and shocked emission (Shull & Hollenbach 1978) for comparison. Particularly useful are the 1-0S(0)/1-0S(1) and 2-1S(1)/1-0S(1) emission line ratios due to the relatively high fluxes of these lines and clear distinctions between the photo-excited and shock-excited ratios (see Table 3).

Using the 1-0S(0) / 1-0S(1) and 2-1S(1) / 1-0S(1) emission line ratios, sources #03, 06, 18, 26 and 34 consistently appear to exhibit emission dominated by collisional excitation with ratio ranges of 0.14–0.27 and 0.11–0.25, respectively. Source #25 is the only source which is clearly photo-excited whilst all other sources appear to exhibit contributions from both photo-excitation and shocked excitation. For instance, whilst none of the 2-1S(1) / 1-0S(1) ratios fall within the photo-excitation range, sources #02 B, 28 B, 36 B and 36 E all have 1-0S(0) / 1-0S(1) ratios consistent with photo-excited gas (0.38–0.55) and 2-1S(1) / 1-0S(1) inconsistent with collisional excitation (0.33–0.46). It is likely that the majority of measured H_2 emission has contributions from both photo-excitation and collisional excitation as reflected in the low 2-1S(1) line strength compared to 1-0S(0) line strength which implies that the 2-1S(1) emission is pri-

marily sourced from shocked excitation whilst the 1-0S(0) emission has a larger contribution from photo-excitation.

Half of our YSO targets exhibit extended H_2 emission; the morphologies of the $2.1218 \mu\text{m}$ 1-0S(1) emission line are shown in Fig. 9. Comparing Figs. 3 and 9, it is clear that the $\text{Br}\gamma$ and H_2 emission morphologies are very different. Sources #01, 02 A, 28 A and 30 exhibit H_2 morphologies extended along a single axis, asymmetric with respect to the continuum source. Source #28 A exhibits a v-shape morphology, indicative of a cone like physical structure. Source #06 exhibits two knots of H_2 emission separated from the continuum source (0.6 arcsec and 1.4 arcsec for the southern and north-western knots, respectively), although the weaker north-western knot appears to be linked by a tenuous tail of emission to the continuum source. Sources #03 and 31 both exhibit irregular elongated emission across the continuum source with offset $\text{Br}\gamma$ emission. Bipolar extended emission is observed centred on sources #22 A and 36 B although that of 36 B appears to be slightly off-centre. Finally source #35 exhibits an arc of H_2 emission as previously studied in Testor et al. (2010), tracing the edge of the compact H II region shown in the $\text{Br}\gamma$ emission. The morphologies of the different emission lines are discussed further in Section 6.

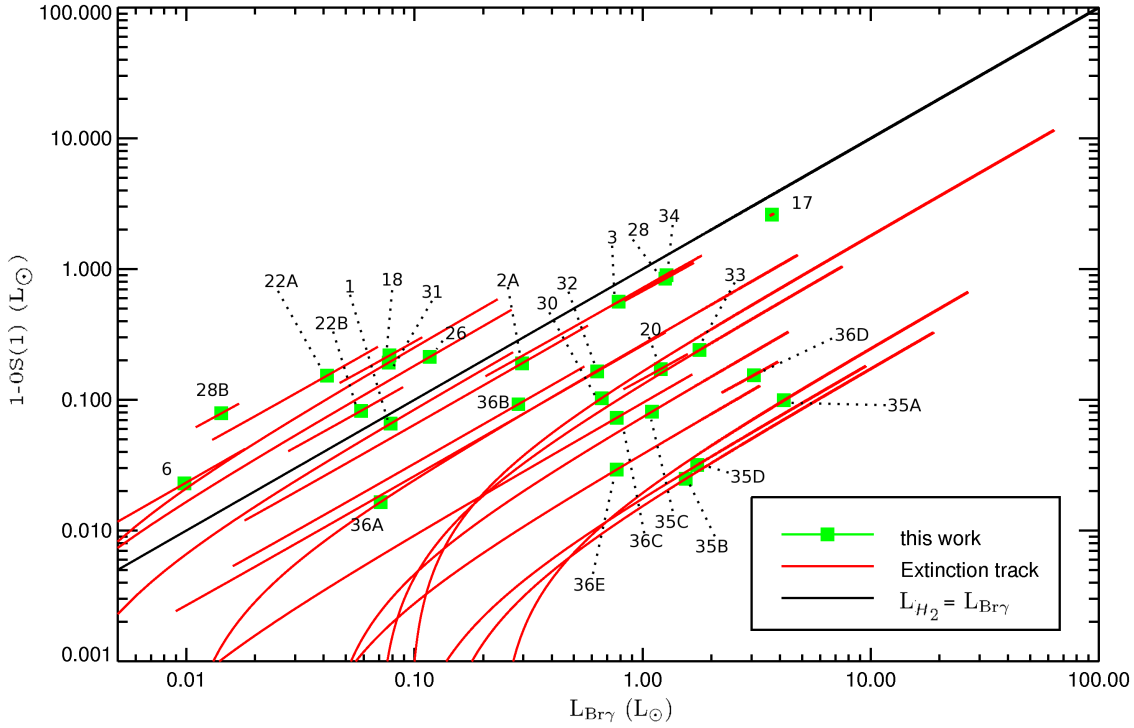


Figure 8. H₂ 2.1218 μm emission vs Brγ emission. The solid black line shows the Brγ emission line luminosity and the H₂ emission line luminosity are equal. See also the caption of Fig. 2.

The centroid velocity fields of the extended H₂ emission are shown in Fig. 10 with the exception of source #31 for which the S/N was not sufficient to measure the centroid position at each spaxel. The H₂ emission detected towards sources #01, 03 and 28 all appears to be slightly red-shifted with respect to the continuum source whilst source #02 appears to exhibit no significant velocity gradient. The H₂ emission in sources #06 and 30 appear to be blue shifted relative to the continuum source. Sources #22 A and 36 B both appear to be at the centre of bipolar outflow structures and the velocity gradients across the length of the structures certainly support this. Finally in source #35 (N88 A) there appears to be a small velocity gradient from south to north.

4.3.4 CO bandhead emission/absorption

The CO bandhead emission red-wards of 2.29 μm in the K-band is widely associated with accretion discs in YSOs (Davies et al. 2010; Wheelwright et al. 2010). Towards our targets in the SMC, only source #03 exhibits detectable CO bandhead emission as shown in Fig. 11. This emission is weak even for the v = 2–0 transition at ~2.295 μm which is not contaminated by low-J CO absorption lines between 2.32 and 2.38 μm. Whilst the detection of CO bandhead emission originating in discs is strongly dependent on geometry (Kraus et al. 2000; Barbosa et al. 2003), the detection rate towards the SMC sources presented in this work is significantly lower than the 17% of Cooper et al. (2013) and is therefore suggestive of a physical difference between this sample and that of Cooper et al. (2013).

When we restrict our comparison to only the range of bolometric luminosities of our SMC targets (1.5 × 10³–1.7 × 10⁵ L_⊙) and exclude any sources from Cooper et al.

(2013) which exhibit P-cygni line profiles (as we have not observed any in the SMC), we find the CO bandhead detection rate of Cooper et al. (2013) drops to 15%. However this is still significantly higher than the detection rate found towards sources in the SMC (5%).

The spectrum of source #02 B appears to exhibit CO in absorption (see lower panel of Fig. 11). Whilst uncommon in massive YSOs, CO absorption is commonly associated with lower mass YSOs (e.g. Casali & Eiroa 1996). Although the S/N is very poor, using the blue edge of the v=2–0 bandhead, we estimate that the measured velocity towards the CO bandhead falls in the range 60–200 km s⁻¹. This is consistent with the velocity measurements made towards source #02 A (see Section 4.4 and Table 4). This detection is discussed in more detail in Section 6.3.1.

4.4 Kinematics of molecular, atomic and excited hydrogen emission

The Gaussian profiles used to fit the emission lines towards the continuum sources in this work yield centroid wavelengths which are converted into velocities. The heliocentric centroid velocities of the measured Brγ and H₂ 2.1218 μm emission lines (with the flexure wavelength shift component subtracted; see Section 3) are shown in Table 4. Also shown in Table 4 are the most likely corresponding heliocentric velocities measured from the HI column density data cube of the SMC (Stanimirovic et al. 1999). Apertures of 2 arcmin radius centred on the coordinates of each of the *Spitzer* YSOs were used to measure the HI 21 cm velocity towards each source.

Figure 12 shows the Brγ velocity plotted against HI 21 cm velocity and H₂ 2.1218 μm velocity against Brγ ve-

Table 3. Extinction corrected H₂ emission line ratios with respect to the 1-0S(1) emission line for all continuum sources. Also included are the expected H₂ line ratios for photo-excitation (Black & van Dishoeck 1987) and shocked emission (Shull & Hollenbach 1978). The final column gives the origin of the emission for those sources for which we are confident of the diagnosis based on the H₂ emission line ratios.

Source	1-0S(0) 2.2235 μm	1-0S(2) 2.0338 μm	1-0S(3) 1.9576 μm	2-1S(1) 2.2477 μm	2-1S(2) 2.1542 μm	2-1S(3) 2.0735 μm	Origin
01	0.49 ^{+0.01} _{-0.02}	0.44 ^{+0.05} _{-0.02}	0.57 ^{+0.13} _{-0.06}	0.193 ^{+0.005} _{-0.011}	0.158 ^{+0.005} _{-0.002}	0.35 ^{+0.03} _{-0.01}	
02 A	0.36 ^{+0.01} _{-0.03}	0.39 ^{+0.07} _{-0.01}	2.09 ^{+0.22} _{-0.01}	0.115 ^{+0.010} _{-0.001}		0.19 ^{+0.21} _{-0.01}	
02 B	0.55 ^{+0.02} _{-0.07}	0.35 ^{+0.07} _{-0.05}	1.6 ^{+0.7} _{-0.17}		0.168 ^{+0.010} _{-0.008}		
03	0.23 ± 0.01	0.25 ^{+0.05} _{-0.01}	2.23 ^{+0.17} _{-0.03}	0.245 ^{+0.003} _{-0.019}	0.104 ^{+0.017} _{-0.003}	0.229 ^{+0.025} _{-0.004}	shock
04							
06	0.14 ± 0.01	0.37 ^{+0.11} _{-0.01}	1.69 ^{+0.01} _{-0.22}	0.113 ^{+0.001} _{-0.010}		0.089 ^{+0.075} _{-0.003}	shock
17		0.48 ^{+0.21} _{-0.16}	4.12 ^{+0.18} _{-0.14}	0.138 ± 0.001			
18	0.25 ± 0.01	0.38 ^{+0.03} _{-0.01}	1.09 ± 0.01	0.175 ^{+0.004} _{-0.010}	0.070 ^{+0.004} _{-0.002}		shock
20	0.23 ± 0.01	0.45 ^{+0.02} _{-0.01}	1.09 ^{+0.22} _{-0.11}				
22 A	0.38 ^{+0.01} _{-0.02}	0.40 ± 0.01	0.74 ^{+0.01} _{-0.01}	0.182 ^{+0.003} _{-0.013}	0.129 ^{+0.010} _{-0.002}	0.117 ^{+0.002} _{-0.001}	
22 B	0.59 ^{+0.01} _{-0.03}	0.37 ^{+0.03} _{-0.01}	1.87 ^{+0.04} _{-0.13}	0.281 ^{+0.006} _{-0.018}	0.265 ^{+0.018} _{-0.006}	0.218 ^{+0.038} _{-0.012}	
25	0.44 ^{+0.01} _{-0.03}			0.463 ^{+0.001} _{-0.041}			photo
26	0.22 ^{+0.03} _{-0.01}	0.31 ^{+0.01} _{-0.10}	1.14 ^{+0.21} _{-0.03}	0.251 ^{+0.038} _{-0.003}	0.103 ^{+0.002} _{-0.001}	0.189 ^{+0.001} _{-0.011}	shock
28 A	0.30 ± 0.01	0.35 ± 0.01	0.56 ^{+0.01} _{-0.03}	0.151 ^{+0.004} _{-0.008}	0.048 ± 0.001	0.126 ^{+0.007} _{-0.003}	
28 B	0.48 ^{+0.01} _{-0.02}	0.54 ^{+0.13} _{-0.07}	1.02 ^{+0.18} _{-0.11}	0.375 ^{+0.010} _{-0.016}		0.308 ^{+0.013} _{-0.008}	
30	0.31 ^{+0.03} _{-0.09}	0.39 ± 0.15	1.2 ± 1.1				
31	0.50 ^{+0.01} _{-0.02}	0.48 ^{+0.02} _{-0.05}	1.12 ^{+0.08} _{-0.24}	0.242 ^{+0.004} _{-0.010}	0.136 ^{+0.003} _{-0.001}	0.296 ^{+0.006} _{-0.018}	
32	0.29 ^{+0.01} _{-0.02}	<1.2		0.337 ^{+0.001} _{-0.030}			
33	0.30 ^{+0.01} _{-0.02}	0.23 ^{+0.02} _{-0.03}		0.270 ^{+0.001} _{-0.021}			
34	0.27 ± 0.01	0.37 ± 0.01	0.85 ^{+0.02} _{-0.05}	0.112 ^{+0.003} _{-0.006}	0.099 ^{+0.016} _{-0.006}		shock
35 A	0.37 ^{+0.01} _{-0.04}	0.30 ^{+0.03} _{-0.05}	0.92 ^{+0.22} _{-0.31}	0.332 ^{+0.004} _{-0.041}	0.116 ^{+0.006} _{-0.004}	0.195 ^{+0.012} _{-0.016}	
35 B	0.34 ^{+0.01} _{-0.05}	0.23 ^{+0.04} _{-0.05}	0.90 ^{+0.34} _{-0.41}	0.318 ^{+0.001} _{-0.058}	0.081 ^{+0.005} _{-0.004}		
35 C	0.39 ^{+0.01} _{-0.03}	0.44 ^{+0.04} _{-0.07}	1.25 ^{+0.25} _{-0.38}	0.334 ^{+0.006} _{-0.035}	0.095 ^{+0.004} _{-0.003}	0.306 ^{+0.016} _{-0.024}	
35 D	0.37 ^{+0.01} _{-0.02}	0.28 ^{+0.02} _{-0.03}	0.8 ^{+0.1} _{-0.2}	0.173 ^{+0.001} _{-0.012}	0.060 ^{+0.002} _{-0.001}	0.125 ^{+0.004} _{-0.008}	
36 A	0.29 ^{+0.01} _{-0.08}	0.37 ^{+0.13} _{-0.14}	1.2 ^{+0.9} _{-1.0}	0.400 ^{+0.001} _{-0.126}			
36 B	0.41 ^{+0.01} _{-0.03}	0.16 ^{+0.08} _{-0.01}	1.04 ^{+0.43} _{-0.01}	0.388 ^{+0.001} _{-0.034}	0.138 ^{+0.087} _{-0.002}	0.337 ^{+0.051} _{-0.001}	
36 C						0.64 ^{+0.02} _{-0.04}	
36 D			2.44 ^{+0.04} _{-0.02}				
36 E	0.38 ^{+0.07} _{-0.01}		1.13 ^{+0.03} _{-0.49}	0.333 ^{+0.072} _{-0.002}			
Photo-excitation	0.4–0.7	0.4–0.6		0.5–0.6	0.2–0.4	0.2–0.3	
1000 K shock	0.27	0.27	0.51	0.005	0.001	0.003	
2000 K shock	0.21	0.37	1.02	0.083	0.031	0.084	
3000 K shock	0.19	0.42	1.29	0.21	0.086	0.27	
4000 K shock	0.19	0.44	1.45	0.33	0.14	0.47	

locity. For all but five cases (sources #01, 03, 22 B, 26 and 33) the atomic hydrogen emission velocities agree within 1σ uncertainty. All but two of the H₂ emission velocities are consistent with the Brγ velocities within 2σ; however, on the whole the H₂ emission does appear to be slightly redshifted with respect to the Brγ emission. The linear fits to the data have the equations $v_{\text{Br}\gamma} = 1.04v_{21\text{cm}} - 5 \text{ km s}^{-1}$ and $v_{\text{H}_2} = 0.80v_{\text{Br}\gamma} + 43 \text{ km s}^{-1}$. This indicates a strong correlation of both the excited atomic gas velocities and the molecular gas velocities with the bulk motions of atomic gas in the ISM of the SMC.

5 OPTICAL SPECTRA

Optical spectra have been previously presented for all but one (#31) of these sources in Oliveira et al. (2013) and we will analyse these in more detail here. We also present the results of the new RSS spectroscopy carried out towards sources #35 and 36 (see Section 3.2). Note that for seven

sources with optical spectra, SINFONI observations are not available.

5.1 Extinction towards optical emission

Although extinction significantly impacts optical observations, it also gives an indication of where the emission originates. This is a particularly important consideration for massive YSOs because they are embedded objects and it is therefore unexpected for them to be observable in the optical regime.

We calculate values of extinction using H I emission lines comparing the attenuated ratio $[H_\alpha/H_\beta]_a$, with the expected intrinsic ratio, $[H_\alpha/H_\beta]_i$;

$$E(B - V) = \frac{\log[H_\alpha/H_\beta]_a - \log[H_\alpha/H_\beta]_i}{0.4(K_{H\beta} - K_{H\alpha})} \quad (5)$$

where $K_{H\alpha}$ and $K_{H\beta}$ are 2.535 and 3.609, respectively (Calzetti 2001). The Case B recombination intrinsic line ratio is normally $H_\alpha/H_\beta \approx 2.87$ at 10 000 K; however, this

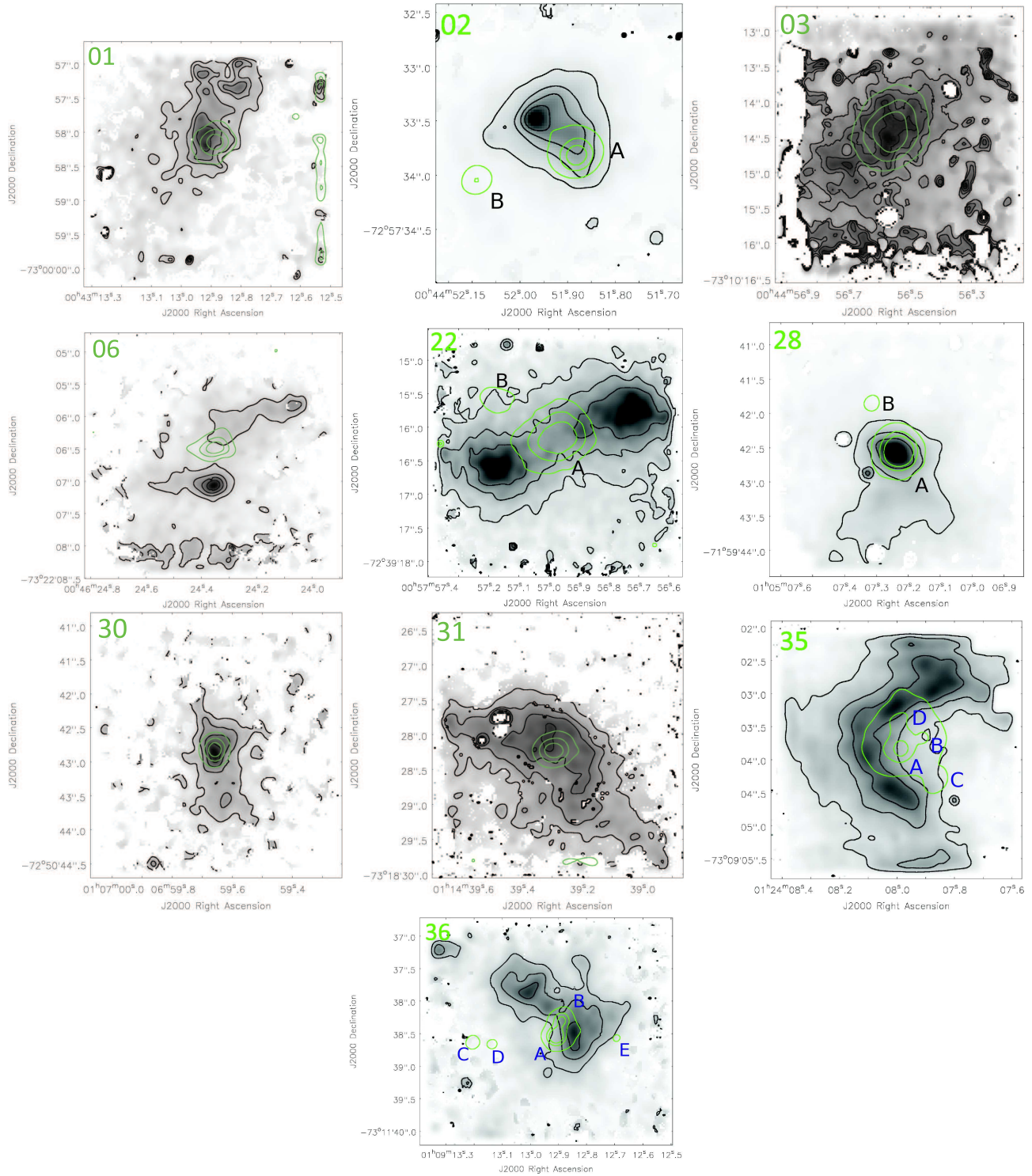


Figure 9. H₂ emission line morphologies for sources: #01, 02, 03, 06, 22, 28, 30, 31, 35 and 36. Black contours - $[0.2, 0.4, 0.6, 0.8] \times$ maximum H₂ 2.1218 μm integrated flux, green contours - continuum flux. The continuum contour levels are as in Fig. 3.

ratio can vary by 5–10% over a temperature range of 5000–20 000 K (Osterbrock & Ferland 2006). For Case A recombination the ratio is 2.86 at 10 000 K (Osterbrock & Ferland 2006) with a similar temperature dependent variance making this ratio largely independent of whether the emission is optically thick or thin. Assuming a Milky Way-like extinction curve with $R=3.1$, we obtain the extinction estimates

shown in Table 5. We find that these are significantly lower than those calculated from the K -band emission (see Section 4.2) although we are only able to calculate extinction values using both methods for 9 of our targets. For these 9 targets, the mean extinction values are $A_V = 12.4 \pm 2.4$ mag in the K -band whilst only $A_V = 1.0 \pm 0.3$ mag in the optical emission. The median values for extinction obtained for

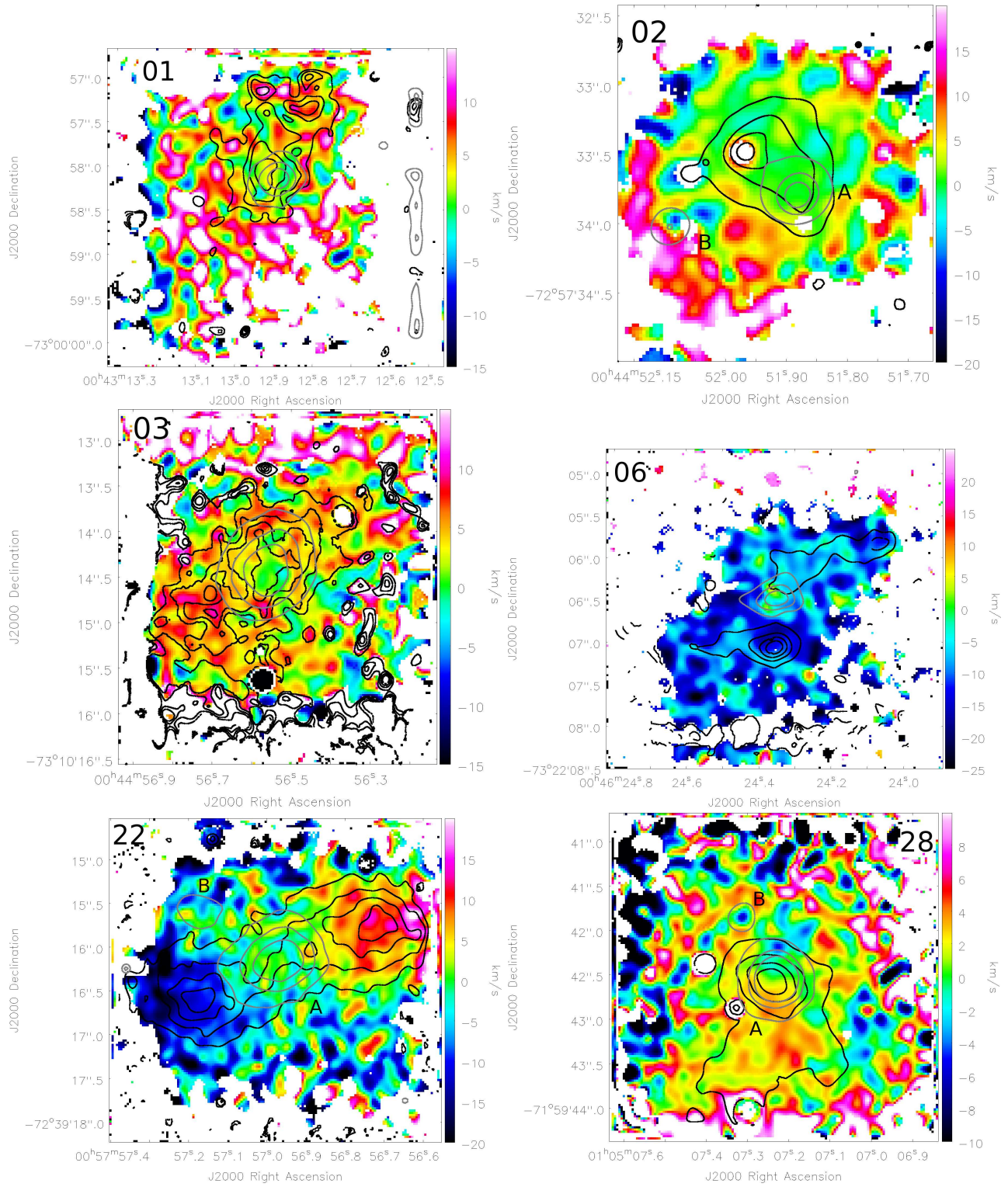


Figure 10. H_2 emission line velocity maps for sources #01, 02, 03, 06, 22, 28. Black contours - $[0.2, 0.4, 0.6, 0.8] \times$ maximum H_2 2.1218 μm integrated flux, grey contours - $[0.25, 0.5, 0.75] \times$ maximum continuum flux.

these 9 sources are $A_V = 13.3$ and 0.81 mag for the K -band and optical measurements, respectively. We use upper limits as A_V values in the optical to provide an adequate sample of extinctions derived from optical emission whilst excluding sources with limits in the K -band. The disparity between the extinction values calculated for the optical and

near-infrared emission suggests that the optical emission is in fact sampled in a much shallower region of the YSO environment rather than at the YSOs themselves and most likely close to the outer edges of the molecular clouds.

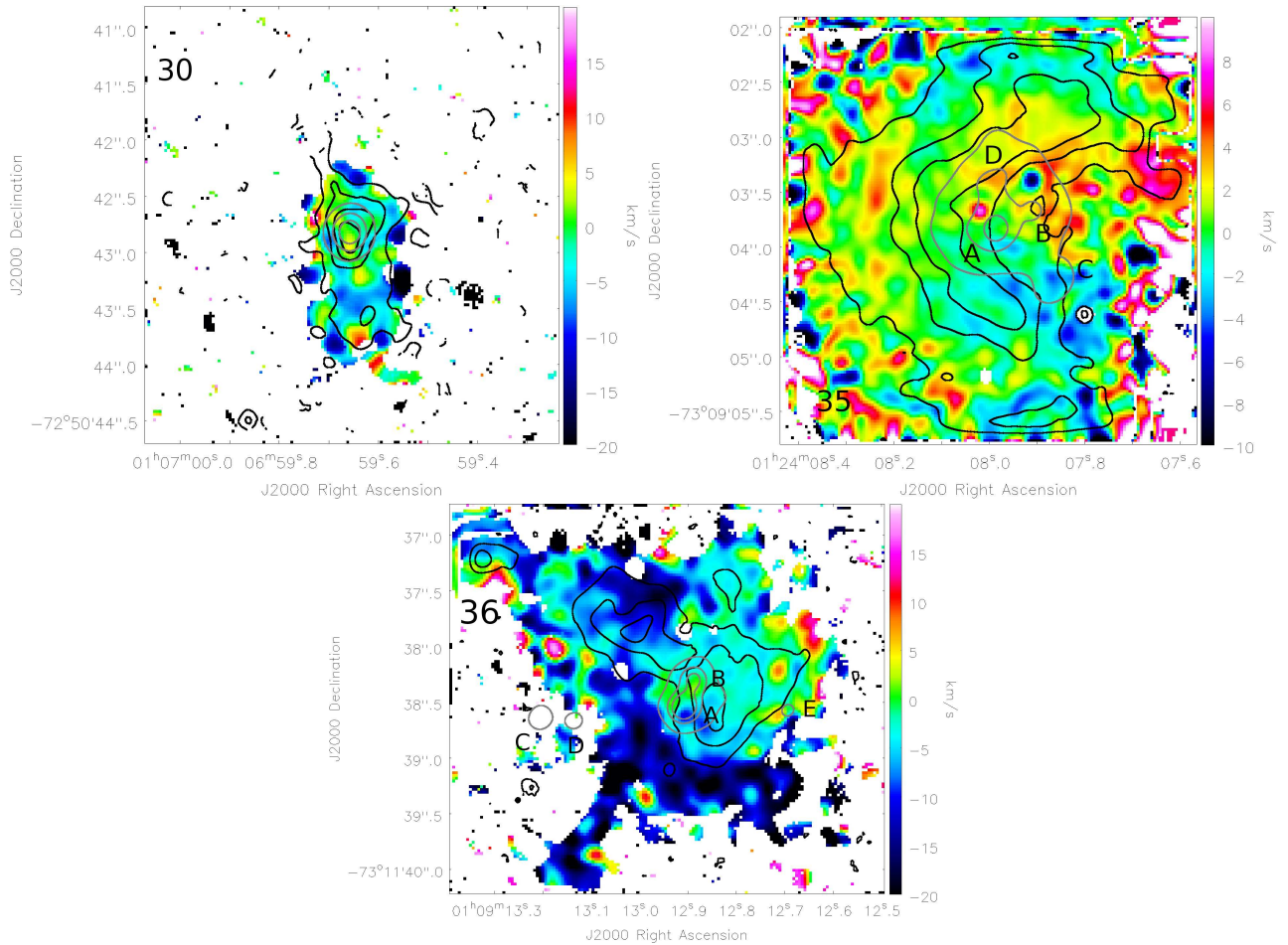


Fig 10 cont. H₂ emission line velocity maps for sources #30, 35, 36.

5.2 Nature of emission

An important consideration in the analysis of the optical emission lines we have measured is the physical process driving the emission, in particular whether the emission is photo-excited or shock excited. In order to constrain this we compare the ratios of emission lines measured in our data with those predicted by models. To investigate the source of the optical emission we use the MAPPINGS III pre-run photoionization grids (Kewley et al. 2001) and shock grids (Allen et al. 2008) to constrain the source of the emission. In Fig. 13 we plot $\log([\text{O III}]/\text{H}\beta)$ against $\log([\text{S II}]/\text{H}\alpha)$ (upper panel) and $\log([\text{O III}]/\text{H}\beta)$ against $\log([\text{N II}]/\text{H}\alpha)$ (lower panel) for all of the sources for which these emission lines could be measured, as well as predictions from the photoionization and collisional excitation grids. Also shown in both panels is the maximum starburst line from Kewley et al. (2001), a theoretical limit above which photoionization alone is not sufficient to produce the observed emission.

We find that the optical emission is not consistent with shocked excitation towards any of our sources. The majority of the sources fall close to the photoionization models with some scatter. It seems reasonable to assert that, as the emission is caused by photo-excitation and the optical extinctions are significantly lower than those measured in the *K*-band, the optical emission arises at a significant distance from the SINFONI continuum sources, in a region closer

to the surface of the molecular cloud. It is therefore also reasonable to assume that the optical emission may have contributions from stars which are outside of our SINFONI FOVs.

5.3 CLOUDY optimization

Where multiple emission lines were detected in the optical spectra we have used the CLOUDY photoionization code to fit parameters using the Tlusty grid of OB-type stellar atmosphere models and assuming abundances of Dufour (1984) where available and a metallicity of $0.2 Z_{\odot}$ for species where measured abundances are not available. When interpreting these results it should be noted that the elemental abundances of the cloud used in the CLOUDY line optimisation process have a significant impact on the results of the analysis.

For the SALT spectra we have treated the red and blue spectral regions separately, using the pg1800 grating observations for N88 A in order to resolve the [N II] emission lines at 6548 \AA and 6584 \AA which are blended with the broad H α emission line in the pg900 grating spectrum. The resulting stellar temperatures and hydrogen densities of the CLOUDY line optimization are shown in Table 6. Also given are the values of the average deviation between the observed extinction corrected line flux relative to H β (or H α where

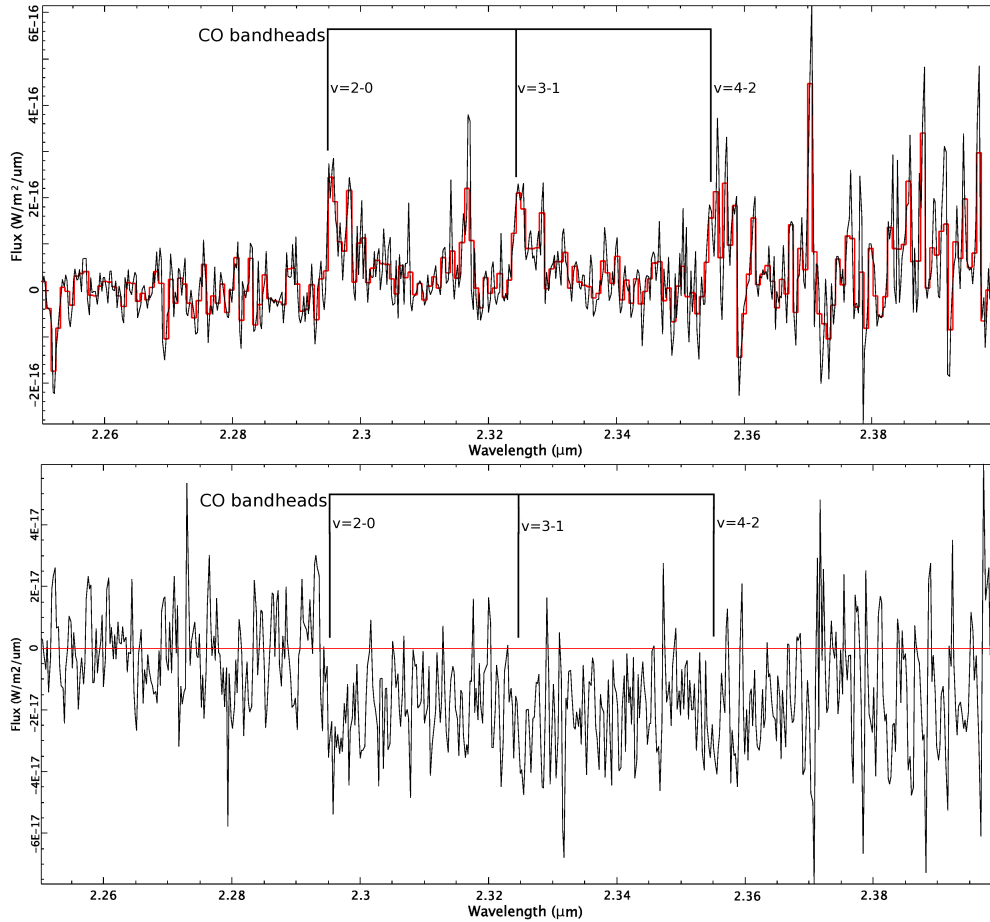


Figure 11. Upper panel: The region of the continuum subtracted spectrum of source #03 which contains CO bandhead emission. The 3-1 and 4-2 bandheads appear to be contaminated by CO absorption lines. Lower panel: Continuum subtracted spectrum of source #02B exhibiting CO absorption features. The positions of the CO bandheads are marked on both spectra.

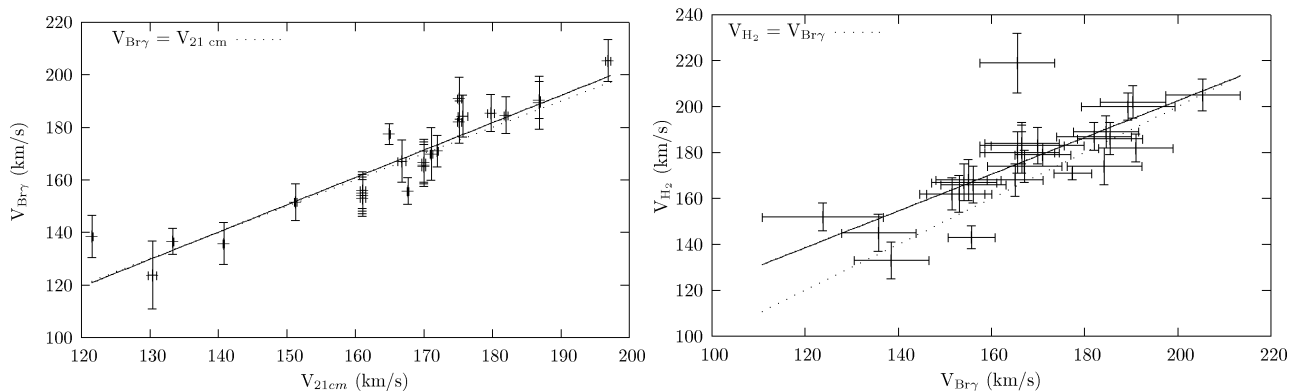


Figure 12. Left: $\text{Br}\gamma$ centroid velocity against H1 velocities as measured in data cube from Stanimirovic et al. (1999). H1 21 cm centroid velocity taken from an aperture of 2 arcmin centred on the YSO position. Right: H_2 2.1218 μm emission centroid velocity against $\text{Br}\gamma$ centroid velocity for all sources for which both can be measured. The solid lines represent a linear fit to the data whilst the dotted lines show equal velocities.

$\text{H}\beta$ is not used as an input) and the model line flux. This is expressed as a multiple of the uncertainty in the observed relative line flux and thus a number significantly less than one is desirable. The penultimate column shows the average line flux as a multiple of the uncertainty in that line flux and hence values greater than three represent 3σ measurements.

The effective temperatures obtained using CLOUDY for the majority of sources are consistent with late O-/early B-type stars. For sources #07 and 12, the uncertainties in the line flux ratios exceed the values themselves and thus these results are highly uncertain. The fits for sources #01, 03, 09 and 25 are poor: the average difference between the ob-

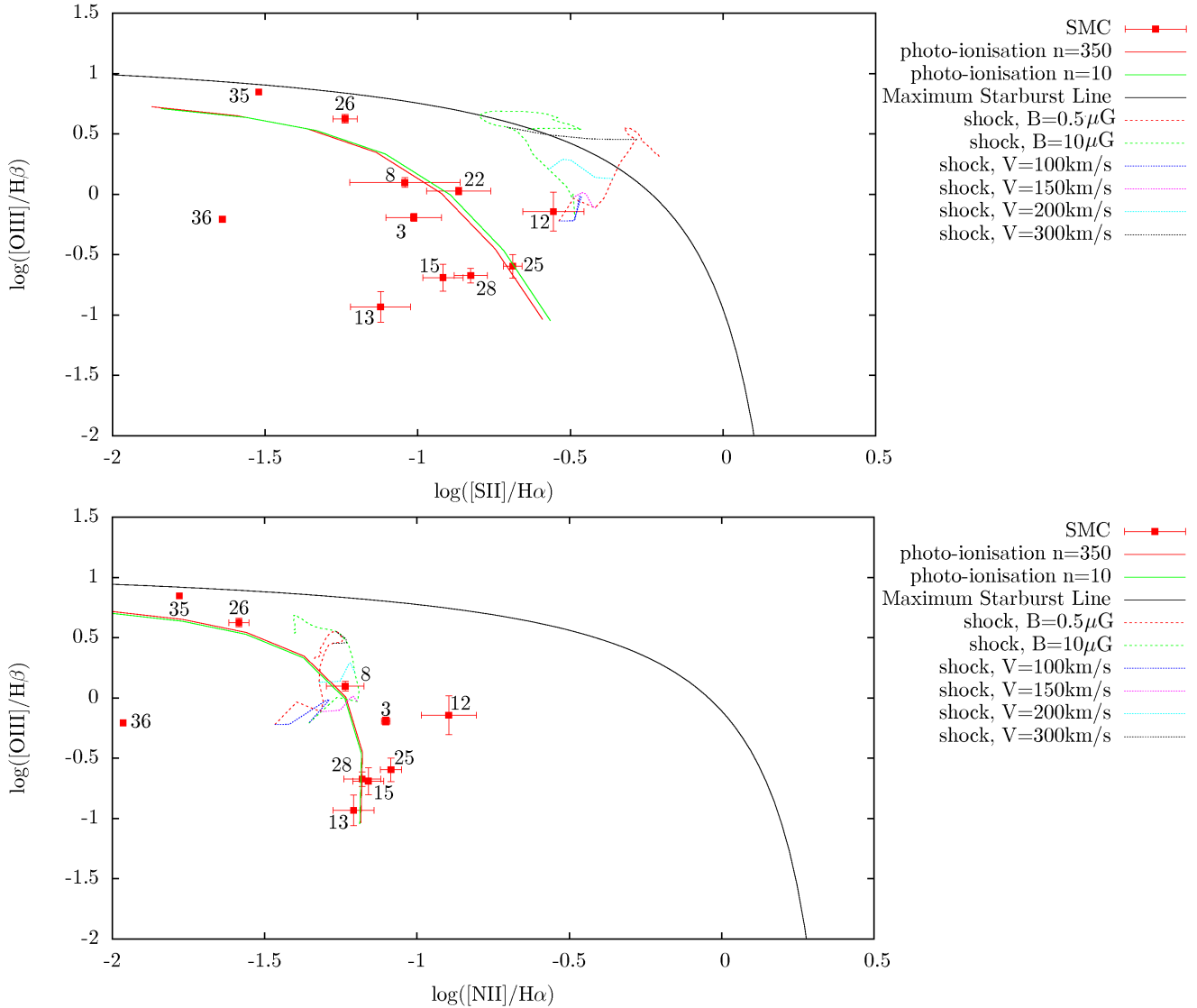


Figure 13. Upper panel: $\log([\text{O III}]/\text{H}\beta)$ vs $\log([\text{S II}]/\text{H}\alpha)$; lower panel: $\log([\text{O III}]/\text{H}\beta)$ vs $\log([\text{N II}]/\text{H}\alpha)$. Also shown are the MAPPINGS III photoionization grids (Kewley et al. 2001) and shock excitation grids (Allen et al. 2008) and the maximum starburst line (see text, Kewley et al. 2001). A metallicity of $0.2 Z_{\odot}$ was adopted for the model grids.

served and model line fluxes is close to (#09, 25) or greater than (#01, 03) the average uncertainty in the measured line fluxes despite having relatively well constrained emission line fluxes available. This may be an indication that multiple unresolved sources contribute to the excitation of the optical lines. The red sections of the spectra for sources #35 and 36 have proven particularly challenging to fit with CLOUDY. For these spectra multiple bright sources of differing spectral types fall within the 1 arcsec width of the slit. It is therefore unsurprising that it is challenging to fit a single star model to these spectra. Nevertheless these fits are consistent with excitation by O-stars as expected (see Section 2).

6 DISCUSSION

SINFONI IFU observations have revealed a total of 29 K -band sources (with obtained resolutions ranging from $\sim 0''.2$ to $\sim 1''.0$) within 19 *Spitzer* YSO candidates in the SMC. Of these $\sim 50\%$ exhibit line emission which extends beyond the full-width-half-maximum (FWHM) of the continuum emission. The emission line properties are summarised in Table 7.

6.1 $\text{Br}\gamma$ emission and accretion rates

In Section 4.3.1 we showed that the $\text{Br}\gamma$ emission line fluxes for our SMC sources are typically higher than those of Galactic massive YSOs with comparable K -band magnitudes. The ATS regressions fitted to the SMC and Galactic data sets yield the following relations between K -band magnitude and

Table 6. Results of the CLOUDY emission line optimization for optical spectra based on the Thusty grid of OB star model atmospheres (Lanz & Hubeny 2003, 2007). Shown are the emission lines used as inputs and the output stellar temperature and cloud density. Also shown are values representing the variation between the model emission line fluxes and the observed fluxes and the average line flux for each source (‘avg |mod-obs|’ and ‘avg flux’, respectively), both expressed as multiples of the uncertainty (σ). The final column gives the spectral type based on ZAMS stars of equivalent effective temperature from Hanson, Howarth & Conti (1997). Sources #07–21 were not observed with SINFONI.

Source	emission lines used	$\log(T_{\text{eff}})$ (K)	$\log(n_{\text{H}})$ (cm^{-3})	avg mod-obs (σ)	avg flux (σ)	Spectral type
01	H α , H β , [S II]6716,6731, [N II]6548,6584	4.511	3.286	1.921	11.736	B0
03	H α , H β , [S II]6716,6731, [N II]6548,6584, [O III]4959,5007	4.505	3.162	2.234	3.329	B0
04	H α , H β , [S II]6716,6731	4.495	2.670	0.540	3.425	B0
07	H α , H β , [S II]6716,6731, [N II]6584	4.517	2.586	0.143	0.964	B0 / O9.5
08	H α , H β , [S II]6716,6731, [N II]6548,6584, [O III]4959,5007	4.539	2.369	0.575	2.477	O9.5
09	H α , H β , [S II]6716,6731, [N II]6548,6584	4.513	3.029	0.958	4.631	B0
12	H α , H β , [S II]6716,6731, [N II]6584, [O III]4959,5007	4.740	1.343	0.104	0.419	<O3
13	H α , H β , [S II]6716,6731, [N II]6548,6584, [O III]4959,5007	4.521	0.106	0.544	1.981	B0 / O9.5
15	H α , H β , [S II]6716,6731, [N II]6548,6584, [O III]4959,5007	4.533	0.998	0.658	2.829	O9.5
21	H α , H β , [S II]6716,6731	4.457	3.125	0.069	1.701	B0.5
22	H α , H β , [S II]6716,6731, [O III]4959,5007	4.585	2.368	0.062	1.724	O8
25	H α , H β , [S II]6716,6731, [N II]6548,6584, [O III]4959,5007	4.534	0.009	0.991	3.263	O9.5
26	H α , H β , [S II]6716,6731, [N II]6584, [O III]4959,5007	4.551	1.171	0.445	1.935	O9
28	H α , H β , [S II]6716,6731, [N II]6548,6584, [O III]4959,5007	4.531	2.098	0.407	1.665	O9.5
35 (N88 A)	H β , [O III]4959,5007	4.63	0.46	0.015	8.854	O6
35 (N88 A)	H α , [S II]6716,6731, [N II]6548,6584	4.54	2.82	2.833	24.52	O9.5
36 (N81)	H β , [O III]4959,5007	4.58	2.96	0.670	43.167	O8
36 (N81)	H α , [S II]6716,6731, [N II]6548,6584	4.56	2.64	1.417	29.0	O8.5

Br γ emission line luminosity.

$$\log(L_{\text{Br}\gamma}(\text{SMC})) = -0.39K - 2.46 \quad (6)$$

$$\log(L_{\text{Br}\gamma}(\text{MW})) = -0.37K - 2.69 \quad (7)$$

If we assume that the same empirically derived relation between Br γ emission and accretion luminosity (Eqn. 4) holds true for both data sets and take, for example, a massive YSO of -6 mag then we arrive at accretion luminosities of $\sim 620 L_{\odot}$ and $\sim 300 L_{\odot}$ for the SMC and Milky Way, respectively. Assuming these hypothetical sources are of the same mass and evolutionary state this suggests an accretion rate in the SMC which is double that of an equivalent object in the Milky Way. Similarly, for the range of absolute K -band magnitudes from 0 to -12 the L_{acc} ratio between the SMC and the Milky Way ranges from 1.6 to 2.6. The Br γ emission measurements towards sources in N113 in the LMC ($Z_{\text{SMC}} \sim 0.4 Z_{\odot}$, Bernard et al. 2008) are on average even higher than those of the SMC sample. However, at least two of the three N113 sources exhibit compact H II regions surrounding the continuum source, contributing significant levels of Br γ emission, likely produced by stellar photons rather than as a result of the accretion shock.

It should be noted that the K -band magnitude for massive YSOs may not be the same in the SMC as in the Milky Way for a given mass and age. Additionally the uncertainties resulting from our extinction corrections for the SMC sources are large (see Fig. 2).

Nevertheless our results appear to be consistent with observations of ~ 1000 Pre-Main-Sequence (PMS) stars in the LMC by Spezzi et al. (2012) and 680 PMS stars in NGC 346 in the SMC by de Marchi et al. (2011) which suggest significantly higher accretion rates in PMS stars in the lower metallicity Magellanic Clouds. However, Kalari &

Vink (2015) analyse the mass accretion rates of PMS stars in the low metallicity ($Z_{\text{Sh}2-284} \sim 0.2 Z_{\odot}$) Galactic star forming region Sh 2-284 and find no evidence of a systematic change in the mass accretion rate with metallicity. It has been suggested that both detection issues towards the Magellanic Clouds sample and physical factors can contribute towards this discrepancy.

Whilst the results in this work allude to higher accretion rates in massive YSOs in the SMC, it is far from certain whether this effect is the result of the lower metallicity environment presented by the SMC. Addressing the question of how accretion is affected by elemental composition will require significantly improved evolutionary models for low metallicity stars for a wide variety of elemental abundances, masses and ages, as well as more extensive Galactic and Magellanic Clouds observations.

6.2 Optical spectra

From our analysis of the H α and H β emission lines we determine values of visual extinction towards the optical emission which are significantly lower than the extinction values calculated from the K -band emission features. We have also determined that, without exception, the optical emission we have measured is dominated by photo-excitation rather than shocked emission. These findings indicate that the optical emission is sourced in a much shallower region of the molecular cloud and that it is produced via the interaction of UV photons with the gas in the outer regions of the cloud. This therefore implies a large mean free path of UV photons which in turn is likely caused by a porous, possibly clumpy ISM which is consistent with the findings of Madden et al. (2006), Cormier et al. (2015) and Dimaratos et al. (2015).

Using the photoionization code CLOUDY, we have been

Table 4. Emission line centroid velocities for Br γ and H₂ 2.1218 μ m emission. Also included are the local H I 21 cm line velocities closest to those velocities measured with SINFONI. Where it is unclear which 21 cm velocity component is associated with the *K*-band emission, the closest two components are listed. The H I 21 cm data is from Stanimirovic et al. (1999), measured from a radius of 2' surrounding the YSO source.

#	Centroid velocity (km s ⁻¹)		
	Br γ	H ₂ 2.12 μ m	H I 21 cm
01	139 \pm 8	133 \pm 8	130 \pm 1
02 A	152 \pm 7	162 \pm 7	151.3 \pm 0.2
02 B		166 \pm 7	151.3 \pm 0.2
03	156 \pm 5	143 \pm 5	167.7 \pm 0.1
04	137 \pm 5		133.4 \pm 0.1
06	124 \pm 13	152 \pm 6	130.4 \pm 0.6, 159.6 \pm 0.4
17	171 \pm 6	179 \pm 5	172.0 \pm 0.1
18	170 \pm 10	183 \pm 8	171.1 \pm 0.2
20	165 \pm 6	168 \pm 7	170.0 \pm 0.3
22 A	182 \pm 8	187 \pm 6	175.2 \pm 0.3
22 B	191 \pm 8	182 \pm 6	175.2 \pm 0.3
25	167 \pm 8	174 \pm 7	166.8 \pm 0.6
26	184 \pm 8	174 \pm 8	175.7 \pm 0.7
28 A	190 \pm 7	202 \pm 7	186.9 \pm 0.1
28 B	189 \pm 10	200 \pm 6	186.9 \pm 0.1
30	185 \pm 7	186 \pm 7	179.8 \pm 0.5
31	185 \pm 7	189 \pm 7	182.0 \pm 0.3
32	136 \pm 8	145 \pm 8	140.8 \pm 0.1
33	177 \pm 4	171 \pm 3	165.0 \pm 0.1, 196.2 \pm 0.3
34	205 \pm 8	205 \pm 7	196.9 \pm 0.4
35 A	156 \pm 7	166 \pm 8	161.0 \pm 0.4
35 B	155 \pm 7	168 \pm 9	161.0 \pm 0.4
35 C	153 \pm 7	162 \pm 8	161.0 \pm 0.4
35 D	154 \pm 7	167 \pm 8	161.0 \pm 0.4
36 A	167 \pm 8	180 \pm 9	170.0 \pm 0.3
36 B	166 \pm 8	180 \pm 9	170.0 \pm 0.3
36 C	166 \pm 8	219 \pm 13	170.0 \pm 0.3
36 D	167 \pm 8	184 \pm 9	170.0 \pm 0.3
36 E	167 \pm 9	183 \pm 8	170.0 \pm 0.3

Table 5. Extinction values calculated from H I line ratios. With the exception of source #04 the sources without visual extinctions derived from *K*-band measurements have not been observed with SINFONI.

source	A _V (optical)	A _V (<i>K</i> -band)
1	1.51 \pm 0.05	2.6 \pm 10.9
3	0.98 \pm 0.18	13.7 \pm 10.8
4	3.10 \pm 0.18	
7	1.95 \pm 0.57	
8	1.15 \pm 0.21	
9	0.54 \pm 0.13	
12	0.91 \pm 0.99	
13	2.65 \pm 0.28	
15	0.86 \pm 0.19	
20	2.47 \pm 1.16	24.1 \pm 13.2
22	<0.24	9.9 \pm 6.4
25	0.47 \pm 0.18	<12
26	<0.30	14.2 \pm 16.6
28	0.81 \pm 0.35	19.5 \pm 9.3
30	2.61 \pm 0.34	13 $^{+55}_{-25}$
35	<0.09	1.2 \pm 17.0
36	<0.08	13.3 \pm 12.8
mean	1.5 \pm 0.4	12.3 \pm 2.7

able to fit excitation parameters to the optical emission based on a single OB type star in a molecular cloud with elemental abundances similar to those of the SMC. We find that the majority of optical spectra are consistent with late-O/early-B type zero-age-main sequence (ZAMS) stars, indicating mass ranges of 10–30 M_⊙ (Hanson, Howarth & Conti 1997). In the majority of cases, however, the objects in question are not straightforward systems comprising of a single ZAMS star illuminating a molecular cloud and the accretion process produces a significant amount of ionizing photons as well. As previously mentioned it is possible that multiple objects contribute to the optical emission (although the emission is still likely to be dominated by the most massive star).

6.3 Properties of massive YSOs in the SMC

Notwithstanding resolution effects (see Section 6.3.1) we expect the *K*-band emission features to reflect the spectral types outlined in Woods et al. (2011), loosely describing an evolutionary sequence. The ice-feature rich G1 type sources are predicted to be the earliest stage YSOs and as such are expected to be dominated by H₂ emission produced in the shock fronts of strongly collimated outflows. The G2 (silicate absorption) sources are expected to exhibit significant Br γ and H₂ emission resulting from UV photons originating at the accretion shock front and outflows, respectively. The later stage YSOs and compact H II regions are expected to be strong PAH emitters, falling into the G3 type. They are also both expected to exhibit strong Br γ and He I emission as a result of the strongly ionizing radiation field of the young massive star (and the shock front of any still ongoing accretion). Consistently the H₂ emission is expected to be largely photo-excited due to the broadening of outflows into lower velocity, uncollimated stellar winds and higher fluxes of energetic photons from the star itself. Compact H II regions may be distinguished by the presence of free-free radio emission produced by the large volume of ionized gas. Shock excited H₂ emission may also be present at the boundaries of compact H II regions during the expansion of the Strömgren sphere. Finally, G4 type sources are dominated by silicate emission which is observed in Galactic Herbig AeBe stars and could be expected in lower mass, later evolutionary stage objects.

Of the nine sources in the sample that exhibit infrared ice absorption features (G1 type; Woods et al. 2011), all nine exhibit H₂ emission, indicative of outflows in early stage YSOs, with extended H₂ emission in five cases. Only two G1 type sources show significant He I emission and only two exhibit free-free radio emission, more commonly found in later stage YSOs and H II regions. Nevertheless our results are largely consistent with the G1 classification representing younger sources. Likewise, of the five G3 type sources (PAH emission), four exhibit radio emission and all of them exhibit He I emission, indicating that these are indeed the more evolved sources. The two G2 type sources (silicate absorption) both exhibit H₂ emission and Br γ emission. The following equivalence can be established between Seale et al. (2009) and Woods et al. (2011): S and SE types are equivalent to G2 types, P and PE types are equivalent to G3 types and O types are equivalent to G4 types. G1 type sources

from the Woods et al. (2011) scheme do not have an analogue in the Seale et al. (2009) classifications.

It must be noted that the spatial scales probed by the *Spitzer*-IRS spectra and the radio data differ significantly from the observations presented in this work. The radio emission column in Table 1 indicates that such emission is present within a distance of 4 arcsec from the source and thus in reality may not be directly associated with the *K*-band continuum sources discussed here. Additionally the slit width of *Spitzer*-IRS varies from 3.6–11.1 arcsec depending on the spectral range, sampling a large area in complex star forming environments and making it difficult to separate the contributions of the YSO and its environment to the measured flux. It should also be noted that some of the IRS sources are resolved into multiple components in this study, demonstrating the obvious limitations of a classification scheme based on low spatial resolution observations.

6.3.1 Compact *K*-band sources

The majority (19/29) of the *K*-band continuum sources identified in this work fall within the ultra-compact regime (diameter ≤ 0.1 pc) with little or no line emission extending beyond the FWHM of the continuum source. In this section we discuss these ultra-compact sources with the exception of those in the N88 A (#35) and N81 (#36) fields which are discussed in detail in Sections 6.3.5 and 6.3.6. In the remaining FOVs we classify 11 sources as compact: #02 B, 04, 17, 18, 20, 22 B, 26, 28 B, 32, 33 and 34.

The five compact sources classified as Seale et al. (2009) S-type (silicate absorption dominated), #17, 18, 32, 33 and 34, all exhibit either $H\alpha$ only in the optical spectrum or type I/II optical spectra. None are sources of radio emission, nor do they exhibit $He\ I$ emission, indicating that these are early stage massive YSOs. Furthermore all but one of these sources (#33, a G2 type) are G1 types, exhibiting ice absorption features indicative of early-stage YSOs. Two of these sources (#18 and 34) exhibit H_2 emission line ratios consistent with shocked excitation linked to outflows whilst none exhibit photo-excitation dominated H_2 emission. They exhibit a wide range of luminosities, *K*-band magnitudes and extinctions, suggesting a wide range of physical conditions and/or masses but what seems apparent is that these make up our embedded, early stage massive YSOs.

Source #04 is a compact P-type/G3-type (Table 1) source, exhibiting a bright *K*-band continuum despite a relatively low luminosity. $Br\gamma$ and $He\ I$ emission are detected towards the source but no H_2 emission, so it is unlikely to be a very early stage YSO due to the lack of outflow indicators. On the other hand, there is no radio emission detected towards this source so identification as an ultra-compact HII region is unlikely. With a spectral type of B0 determined from the CLOUDY optimization, this source is likely to fall at the lower end of our mass range.

The only compact PE type (dominated by PAH emission with fine-structure emission), source #26, is also a G3 Woods et al. (2011) type exhibiting a fairly high luminosity ($1.2 \times 10^4 L_\odot$). It has a type V optical spectrum with a $\log([O\ III]/H\beta)$ value comparable to that of N88 A (see Fig. 13) and exhibits $Br\gamma$, $He\ I$ and H_2 emission in the *K*-band, indicative of a strongly ionizing source. It also exhibits free-free radio emission, typical of an UCHII but the H_2 emis-

sion in the *K*-band is more consistent with shocked emission than photo-excitation. It is therefore possible that the H_2 emission originates in a shock front of an expanding UCHII region.

Source #20 is the only YSO in this work that exhibits silicate emission (O type and G4 type classifications of Seale et al. (2009) and Woods et al. (2011) respectively). It is therefore likely to be lower mass than the majority of sources in this study and possibly in a later evolutionary state. The bolometric luminosity is low ($1.5 \times 10^3 L_\odot$), consistent with a Herbig Be type object and the optical type of the star (I) suggests relatively low levels of ionizing radiation. The extinction appears to be unusually high (24 ± 13 mag; c.f. Fairlamb et al. 2015) suggesting that it is more embedded than would be expected for a Herbig Be star. The high level of extinction measured in the *K*-band could be a geometric effect, for example an edge on dusty disc; however, because the object is unresolved this is only speculation.

Source #02 B exhibits a spectrum which is featureless except for H_2 emission which appears to be largely ambient (see Fig. 9) and CO absorption red-wards of $2.9 \mu\text{m}$. CO in absorption is not a common feature of massive YSOs but it has been detected towards two high confidence massive YSOs in the Milky Way (G023.6566–00.1273 and G032.0518–00.0902; Cooper et al. 2013). CO absorption is commonplace in lower mass YSOs (e.g., Casali & Eiroa 1996); however, source #02 B is relatively bright ($K = 15.75 \pm 0.1$ mag) and it is therefore unlikely to be a low mass star. The velocity range estimated for the CO absorption towards source #02 B is consistent with the line centroid measurements towards the massive YSO #02 A meaning it cannot be dismissed as an unrelated background source.

The remaining compact sources (#22 B and 28 B) exist in close proximity to a brighter *K*-band source and are unlikely to be the dominant source of the spectral properties examined by Oliveira et al. (2013). The line emission towards each of these sources appears to be ambient (see Figs 2, 6 and 9) and as such the nature of these sources remains unclear; if they are YSOs then they could be early stage and/or low mass objects.

6.3.2 Extended outflow sources

Seven sources exhibit extended H_2 emission morphologies indicative of molecular outflows: #01, 02 A, 06, 22 A, 28 A, 30 and 36 B. Two of these sources (#22 A and 36 B) exhibit clear bipolar, relatively collimated structures with a blue- and a red-shifted component (see Figs. 9 & 10) consistent with a bipolar outflow perpendicular to a disc. Source #22 A exhibits weak, compact $Br\gamma$ emission whilst the $Br\gamma$ emission detected towards source #36 B appears to be largely ambient to the region. Source #28 A (see Fig. 14) exhibits a slightly red-shifted v-shaped region of H_2 emission to the south, most likely tracing cone shaped shocked and PDR emission at the edges of an outflow. In the centre of the outflow, a low density region is formed allowing the gas there to be ionized which causes the $Br\gamma$ recombination emission (see Fig. 14). Sources #01, 02 A and 30 exhibit extended H_2 emission in a single direction from the continuum source. The last of the outflow-like morphology sources, source #06 exhibits a knot of H_2 emission to the south and a more extended emission structure to the north west. Both of these

Table 7. Observed spectral properties of all sources. For sources marked with an “E” the relevant line emission is extended beyond the FWHM of the continuum emission. “A” signifies that the emission measured is likely to be ambient whilst “?” is indicative of a high degree of uncertainty in either the measurement or the source of the emission. Also included are the mid-IR classifications (W11 type; Woods et al. 2011) and whether radio emission is detected towards the sources. The 9th column gives the optical spectrum type for each source (see Table 1) where H α indicates that only H α emission is detected. The final column is a type based on the *K*-band morphology observed in this study for each source. Compact sources (C) are discussed in Section 6.3.2 and extended outflow sources (O) are discussed in Section 6.3.3. the outflow sources #03 and 31 (O*) in which the Br γ and HeI emission line morphologies are distinctly offset from the continuum and H $_2$ emission are discussed separately in Section 6.3.4. The H II morphological classification indicates that the source is the major ionizing source of a compact H II region. The compact H II region N88 A is discussed in Section 6.3.6. and N81 is discussed in 6.3.5.

Source	H $_2$ emission	Maser emission	Br γ emission	HeI emission	CO bandhead	W11 type	Radio emission	Optical type	Morphological type
01	✓E		✓E	✓E		G3	Y	IV/V	O
02 A	✓E		✓			G1	Y	H α	O
02 B	✓								C
03	✓E	H $_2$ O	✓E	✓E	✓	G1	Y	V	O*
04			✓	✓		G3	N	II	C
06	✓E		✓	?		G1	N		O
17	✓		✓			G1	N	H α	C
18	✓		✓	✓		G1	N	H α	C
20	✓		✓			G4	N	I	C
22 A	✓E		✓			G1	N	IV/V	O
22 B	✓		✓						C
25	✓?		✓?	?		G3	Y	IV	
26	✓		✓	✓		G3	Y	V	C
28 A	✓E		✓E	✓		G2	Y	IV/V	O
28 B	✓			✓					C
30	✓E		✓			G1	N	I	O
31	✓E		✓E	✓		G3	Y*		O*
32	✓		✓			G1	N	I/II	C
33	✓		✓			G2	N	I/II	C
34	✓		✓			G1	N	H α	C
35 A	✓E		✓E	✓E				V	C/H II
35 B	✓		✓A	✓A					C
35 C	✓		✓A	✓A					C
35 D	✓		✓A	✓A					C
36 A	✓A		✓A	✓A				V	C
36 B	✓E		✓A	✓A					O
36 C			✓A	✓A					C
36 D			✓A	✓A					C
36 E	✓A		✓A	✓A					C

structures appear slightly blue shifted with respect to the continuum source.

Only a single source exhibits a 1-0S(0) / 1-0S(1) emission line ratio consistent with purely shocked emission with the majority of sources exhibiting ratios which lie between the expected ranges for shocked and photo-excited emission. On the other hand all but one 2-1S(1) / 1-0S(1) ratios (where the 2-1S(1) line is measured) are consistent with a shock excitation mechanism. We deduce therefore that, since the upper energy level of the 2-1S(1) transition (12550 K) is almost double that of the 1-0S(0) transition (6471 K), the 1-0S H $_2$ transitions are stimulated by a combination of photo-excitation from the central (proto-)star and shocks from outflows/winds whilst 2-1S transitions are dominated by shocked excitation from outflows.

As discussed previously, the observed ice features towards sources #02, 06, 22 and 30 are consistent with early-stage YSOs (sources #02 and 22 are both resolved into multiple components in the *K*-band so the origin of the ice absorption in these fields remains uncertain). Source #02 also

exhibits radio emission but the difference in spatial resolution means that the radio emission may not originate from the *K*-band sources detected in this work. Source #01 is dominated by PAH emission indicating a later stage massive YSO whilst source #28 is dominated by silicate absorption and likely is at an evolutionary state between the ice feature dominated sources and source #01.

Target #28 (see Fig. 14) is by far the most luminous of our targets with a bolometric luminosity of $1.4 \times 10^5 L_{\odot}$ and source #28 A is the dominant source of *K*-band emission in the field. Source #28 A also exhibits relatively high level of extinction in the *K*-band (for the SMC) and a low level of extinction in the optical. The results of the CLOUDY optimization for the optical spectrum of source #28 indicates excitation consistent with an O9.5 type star.

6.3.3 Sources #03 and 31

Although the H $_2$ emission line morphologies of sources #03 and 31 are consistent with the extended outflow sources,

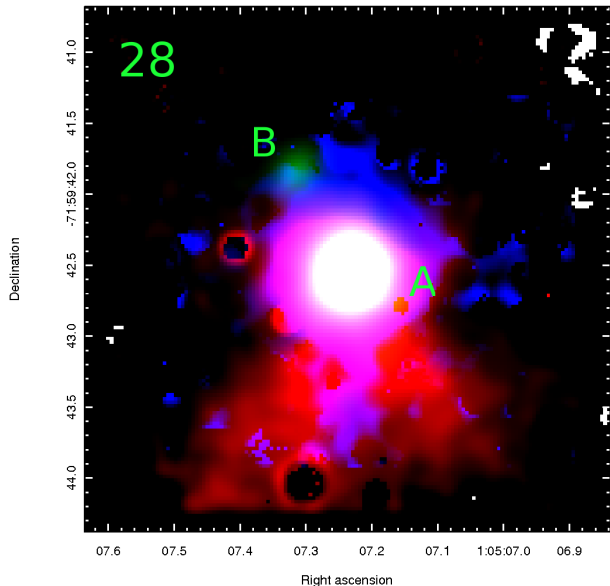


Figure 14. Three colour image of source #28. Red - H₂ 1-0S(1) emission, green - K-band continuum emission, blue - Br γ emission.

the Br γ and He I morphologies (see Figs. 3 and 6) clearly distinguish them from the rest of the sources so we discuss these sources separately in this section. In both cases the atomic emission line structures are offset significantly from both the continuum emission and the H₂ emission.

Originally classified as a planetary nebula by Lindsay (1961) and reclassified as a YSO by van Loon et al. (2010), source #03 presents a challenging morphology to interpret. A three colour image of source #03 is given in Fig. 15, showing the displacement of the Br γ emission (shown in blue) with respect to both the continuum source and the H₂ emission (in green and red, respectively). As this is the only source to exhibit CO bandhead emission, the presence of a disc is probable. The most likely origin of the extended H₂ emission and offset extended Br γ emission is a wide, relatively uncollimated outflow which is bound by the presence of a disc and has created a low density cavity along the axis of rotation in which the remaining gas is ionized. The broadening of outflows in massive YSOs leading to a low density ionized region in the centre of the outflow is predicted and modelled by Kuiper, Yorke & Turner (2015) and Tanaka, Tan & Zhang (2015), caused by continued accretion onto the central protostar in a YSO environment over time. It is therefore possible that this source represents a slightly more evolved state than that of source #28 A (Fig. 14).

A comparison of H₂ emission line ratios for the continuum source and the nearby off-source emission indicates that source #03 is dominated by shocked emission towards the continuum source itself with a much lower contribution of shocked excitation further from the continuum source. This is consistent with a photo-excitation region bordering an H II region which is ultimately powered by a broad, uncollimated outflow in the inner regions of the YSO. The kinematics of source #03 (see Table 4) indicate that the H₂ emission towards the continuum source is blue-shifted with respect to the Br γ emission and both the extended Br γ emission and

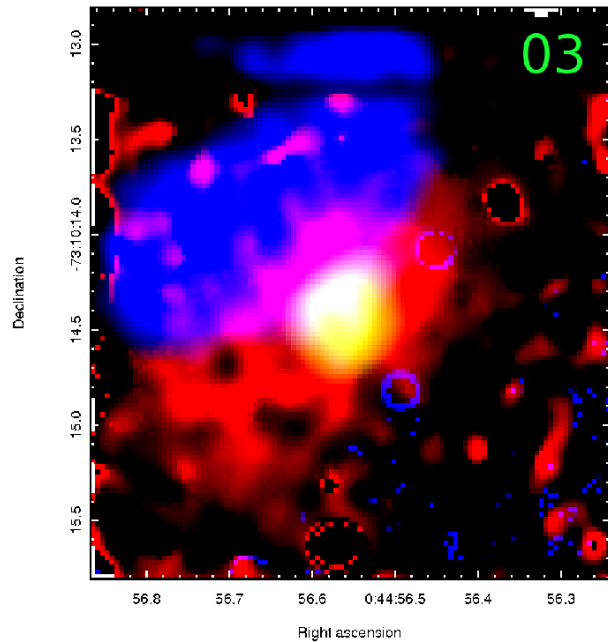


Figure 15. Three colour image of source #03. Red - H₂ 1-0S(1), green - K-band continuum, blue - Br γ .

He I emission are blue-shifted with respect to the continuum source (see Figs. 4 & 7)

Finally, source #03 lies closer to previously detected H₂O maser emission (Breen et al. 2013) than any other source within our sample. The velocity of the maser falls within the range 136.4–143.0 km s⁻¹ which is consistent with the velocities we have measured towards the K-band source. This emission is detected approximately 3.7 ± 0.5 arcsec (1.1 ± 0.1 pc) to the south of the position of the continuum source #03, outside the SINFONI FOV. Therefore the maser emission may not in fact be associated with source #03. Still if the Br γ emission represents an ionized cavity as the result of powerful outflows from the source then it is conceivable that associated maser emission may be detected at relatively large distances from the continuum source.

Source #31 exhibits similar Br γ and H₂ emission morphologies to source #03. However, the properties of these objects as determined by Oliveira et al. (2013) differ significantly. The Seale et al. (2009) classification of source #03 is an S type and that of the Woods et al. (2011) scheme is G1 whilst for source #31 they are PE and G3. Additionally source #31 has a bolometric luminosity around a tenth that of source #03 indicative of an object with a significantly lower mass. Contrary to source #03, the H₂ 1-01S(0) / 1-0S(1) emission line ratio towards source #31 is consistent with a PDR. Source #31, although apparently similar morphologically, possibly represents a much lower mass than source #03.

6.3.4 Source #35 (N88 A)

Our observations of N88 A (source #35; Fig. 16) are consistent with those by Testor et al. (2010), with the dominant source of ionization being the central bright star (star #41 in Testor et al. 2010). We consistently find that all four bright

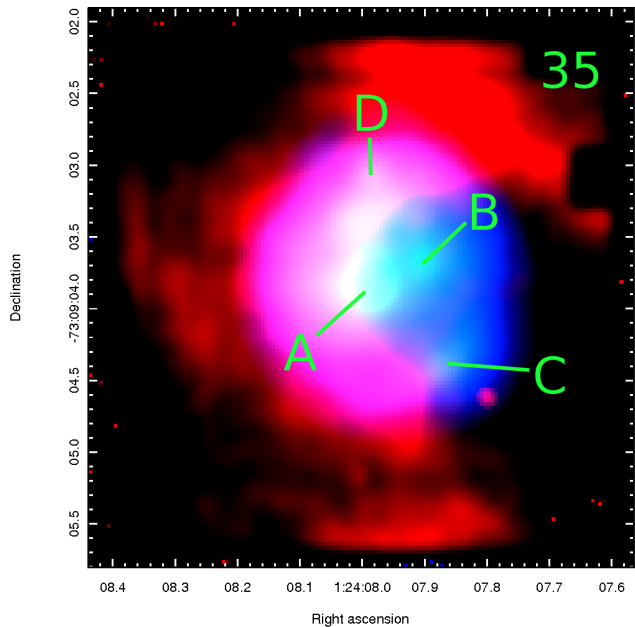


Figure 16. Three colour image of source #35 (N88 A). Red - H₂ 1-0S(1), green - K-band continuum, blue - Br γ .

stars in N88 A appear brighter in our work than Testor et al. (2010) in K-band continuum magnitude. This is most likely because we do not take into account the high levels of background nebulous emission. The measured absolute K-band magnitude of source #35 A is consistent with a ZAMS star with a temperature in excess of 50 000 K, consistent with a star which is more massive than an O3 spectral type object (Hanson, Howarth & Conti 1997). This is likely to be an overestimate of the mass of the star because the effects of any warm dust excess and nebulous emission are neglected. The resulting best fitting solution using CLOUDY is for an exciting source of spectral type O6.

Source #35 A exhibits strong Br γ emission and He I emission with some ambient H₂ emission originating in the H₂ emission arc (see Fig. 16). The remaining sources in N88 A are affected significantly by ambient emission originating from the central bright star #35 A. Peaks in both Br γ emission and He I emission also occur at the positions of sources #35 C and 35 D, which suggests that there is an additional component originating from these sources. None of the continuum sources appear to be significant sources of H₂ emission, implying that they are not early-stage YSOs. Source #35 B does not appear to exhibit any intrinsic emission but weak emission cannot be ruled out due to its proximity to source #35 A.

Towards the H₂ emission line arc we find that the measured H₂ emission line ratios suggest a combination of collisional excitation and photo-excitation where the emission from 1-0 transitions have a significantly higher contribution from photo-excitation compared to the 2-1 transitions. The collisional component is most likely caused by the impact of the expanding ionized gas on the surrounding molecular cloud, forming the H₂ emission arc observed in the east of N88 A; an additional photo-excited component is sourced from the massive stars in the centre of the region.

Rather than showing an association with the H I gas

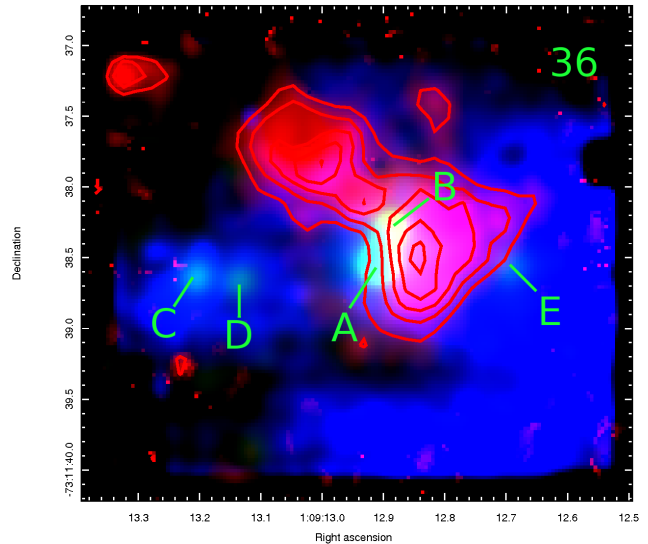


Figure 17. Three colour image of source #36 (N81). Red - H₂ 1-0S(1), green - K-band continuum, blue - Br γ . For clarity the red contours trace the H₂ emission.

component at 134 ± 9 km s⁻¹ (Testor et al. 2010), both the SINFONI velocity measurements for H I and H₂ emission and the radio H I velocities obtained from the data of Stanimirovic et al. (1999) are significantly higher than this. The H₂ velocities we measure towards the continuum sources in N88 A range from 162 to 167 km s⁻¹ with a typical uncertainty of 8 km s⁻¹, consistent with the measured 21 cm peak at 161.1 ± 0.4 km s⁻¹. It therefore appears most likely that N88 A is associated with the SMC gas component at 167 ± 8 km s⁻¹ (McGee & Newton 1981). The Br γ emission velocities range from 153 to 156 km s⁻¹ with a typical uncertainty of 7 km s⁻¹, blue-shifted with respect to the bulk motion of the gas. This is consistent with a compact H II region in which the ionized gas is expanding outwards due to radiation pressure at a velocity of ~ 10 km s⁻¹, comparable to the compact H II regions observed in LHA 120-N113 in the LMC (Ward et al. 2016).

6.3.5 Source #36 (N81)

We have resolved the central region of N81 into 5 distinct K-band continuum sources, a significant improvement on the previous highest resolution seeing limited imaging available (Heydari-Malayeri et al. 2003) which resolved only two sources. The most distinctive newly resolved feature of N81 is the bipolar H₂ emission centred on (or near to) source #36 B (Fig. 17). This bipolar morphology and the observed velocity gradient indicate a bipolar outflow centred on source #36 B, suggestive of an early stage massive YSO.

The majority of the Br γ emission towards this region appears to be ambient and is likely common to the whole N81 H II region. There may be an additional component from one or both of the fainter (and probably lower mass) sources #36 C and 36 E. A similar morphology is observed in the He I emission. Although it is the brightest continuum source in the region, emission detected towards source #36 A appears to be entirely ambient.

The velocities we have determined towards sources in

N81 from Br γ emission range from 166 to 167 km s $^{-1}$ with uncertainties of ~ 9 km s $^{-1}$. These are consistent with both the results of Heydari-Malayeri et al. (1988) determined from H β emission and the velocity determined from the radio observations (see Section 4.4) indicating a common bulk motion of the atomic and ionized gas. The H $_2$ 2.1218 μ m emission towards the same sources has been measured to be consistently red-shifted with respect to the Br γ emission.

7 CONCLUSIONS

We have performed K -band SINFONI observations for 17 of the 33 massive YSOs in the SMC presented in Oliveira et al. (2013), as well as two additional targets in N81 and N88 A, revealing a wide range of spectroscopic properties. We have also analysed optical spectra for 28 of the 33 massive YSO targets of Oliveira et al. (2013) plus sources 35 (N88 A) and 36 (N81). We summarise our conclusions below.

(i) 14 of the 17 *Spitzer* YSOs in the SMC observed with SINFONI have been resolved into single K -band continuum sources whilst three have been resolved into multiple components in the K -band. Source #35 (N88 A) has been resolved into the previously known 4 continuum components. N81 (#36), previously resolved into two components by Heydari-Malayeri et al. (2003), has now been resolved into five K -band continuum sources.

(ii) Visual extinctions have been calculated towards all K -band sources except source #04. We find a median visual extinction towards the SMC sources of $A_V = 14$ mag. The median for the Galactic sources from Cooper et al. (2013) is 44 mag and that for the three YSOs in N113 in the LMC is 20 mag (Ward et al. 2016). This seems to suggest that there is a correlation between extinction towards YSOs and metallicity as $Z_{\text{LMC}} \sim 0.5 Z_{\odot}$ and $Z_{\text{SMC}} \sim 0.2 Z_{\odot}$.

(iii) Whilst consistent with the Cooper et al. (2013) sample, Br γ luminosities are high compared with those in the Milky Way, suggesting accretion rates which are on average higher than for the Galaxy.

(iv) He I line luminosities are comparable to the Milky Way sample, indicating that the excess observed in the Br γ emission is unlikely to be related to a stronger wind component.

(v) Average velocities have been measured towards the *Spitzer* YSO sources of 169 ± 5 km s $^{-1}$ and 173 ± 4 km s $^{-1}$ for Br γ emission and H $_2$ emission, respectively. The Br γ emission line velocities are consistent with those of the H I radio observations, indicating that the average motions of the YSOs are bound to the bulk motions of the ISM.

(vi) The majority of the K -band continuum sources (11/20; excluding observations towards the H II regions N81 and N88 A) fall within the unresolved, ultra-compact regime. These sources exhibit a variety of spectral properties and include one probable UCH II region (#26), a possible Herbig Be star (#20) along with spectroscopically typical massive YSOs and two apparently featureless continuum sources (#22 B and 28 B) which may not actually be YSOs.

(vii) Seven sources with extended H $_2$ emission morphologies indicative of outflows have been identified, with velocity gradients measured towards four of these. Sources #22 A and 36 B exhibit striking examples of bipolar outflow morphologies. Our observations of the well-studied H II region

N81 are the first to identify the bipolar outflow originating from source #36 B.

(viii) Source #28 A exhibits Br γ and H $_2$ emission line morphologies indicative of an ionized cavity in the centre of the outflow. Source #03 appears to be an extremely broadened (and possibly more evolved) example of the same structure. These structures are possibly the result of the broadening of outflows in massive YSOs predicted by the models of Kuiper, Yorke & Turner (2015) and Tanaka, Tan & Zhang (2015).

(ix) CO bandhead emission (commonly used as a tracer of discs) has only been detected towards one source (#03), a detection rate of around one third of that towards massive YSOs in the Milky Way (Cooper et al. 2013) for the same range of luminosities. This could be due to either the low gas-phase CO abundance of the SMC (Leroy et al. 2007), or conditions within protostellar discs which differ significantly (such as higher temperatures or less shielding from dust) from those in the Milky Way, leading to a higher rate of CO destruction. CO absorption is somewhat tentatively observed towards one source (#02 B) which could be indicative of a dusty circumstellar environment and possibly suggests a continuum source completely obscured by an edge-on disc.

(x) Optical emission towards all sources (where it is present) appears to originate from the outer edges of the molecular clouds as the average extinction measured towards the optical emission is significantly lower than that towards the K -band emission for the same targets. The optical emission is photo-excited and is therefore unlikely to be produced by the interaction of outflows and winds with the ISM. This scenario is consistent with relatively large mean free path of high energy photons from the protostar and through the ISM, leading to a large number of UV photons leaking from the YSOs. This could occur due to a clumpy and/or torn-up circumstellar medium, consistent with expectations for a low metallicity ISM (Madden et al. 2006; Cormier et al. 2015; Dimaratos et al. 2015).

To conclude, we have presented the first study of massive YSOs in the SMC using integral field spectroscopy, studying line emission and resolving a number of our targets into multiple components in the K -band for the first time. Through comparison with existing data in the optical, infrared and radio regimes, we have been able to develop a greater understanding of these objects within an evolutionary context. Following from the work on ice chemistry by Oliveira et al. (2013), we continue to expose differences between YSO properties in our own Galaxy and the low metallicity SMC, namely those which concern accretion, potential disc properties and the YSO–ISM interplay.

ACKNOWLEDGMENTS

The authors thank the anonymous referee for his/her useful comments. JLW acknowledges financial support from the Science and Technology Facilities Council of the UK (STFC) via the PhD studentship programme. We would like to thank the staff at ESO’s Paranal observatory for their support during the observations. Some of the observations reported in this paper were obtained with the Southern African Large Telescope (SALT). This paper made use of information from the Red

MSX Source survey database at http://rms.leeds.ac.uk/cgi-bin/public/RMS_DATABASE.cgi which was constructed with support from STFC. This research has made use of the SIMBAD data base, operated at CDS, Strasbourg, France.

REFERENCES

- Akritas M. G., Murphy S. A., Lavalley M. P., 1995, *JOURNAL OF THE AMERICAN STATISTICAL ASSOCIATION*, 90, 170
- Allen M. G., Groves B. A., Dopita M. A., Sutherland R. S., Kewley L. J., 2008, *ApJS*, 178, 20
- Barbosa C. L., Damineli A., Blum R. D., Conti P. S., 2003, *AJ*, 126, 2411
- Bernard J.-P. et al., 2008, *AJ*, 136, 919
- Black J. H., van Dishoeck E. F., 1987, *ApJ*, 322, 412
- Bolatto A. D. et al., 2007, *ApJ*, 655, 212
- Breen S. L., Lovell J. E. J., Ellingsen S. P., Horiuchi S., Beasley A. J., Marvel K., 2013, *MNRAS*, 432, 1382
- Buckley D. A. H., Swart G. P., Meiring J. G., 2006, in *Society of Photo-Optical Instrumentation Engineers (SPIE) Conference Series*, Vol. 6267, *Society of Photo-Optical Instrumentation Engineers (SPIE) Conference Series*, p. 0
- Calvet N., Muzerolle J., Briceño C., Hernández J., Hartmann L., Saucedo J. L., Gordon K. D., 2004, *AJ*, 128, 1294
- Calzetti D., 2001, *PASP*, 113, 1449
- Cardelli J. A., Clayton G. C., Mathis J. S., 1989, *ApJ*, 345, 245
- Casali M. M., Eiroa C., 1996, *A&A*, 306, 427
- Charmandaris V., Heydari-Malayeri M., Chatzopoulos E., 2008, *A&A*, 487, 567
- Cooper H. D. B. et al., 2013, *MNRAS*, 430, 1125
- Cormier D. et al., 2015, *A&A*, 578, A53
- Crawford E. J., Filipovic M. D., de Horta A. Y., Wong G. F., Tothill N. F. H., Draskovic D., Collier J. D., Galvin T. J., 2011, *Serbian Astron. J.*, 183, 95
- Davies B., Lumsden S. L., Hoare M. G., Oudmaijer R. D., de Wit W.-J., 2010, *MNRAS*, 402, 1504
- Davis C. J. et al., 2011, *A&A*, 528, A3
- de Marchi G., Panagia N., Romaniello M., Sabbi E., Sirianni M., Prada Moroni P. G., Degl’Innocenti S., 2011, *ApJ*, 740, 11
- Dimaratos A., Cormier D., Bigiel F., Madden S. C., 2015, *A&A*, 580, A135
- Dufour R. J., 1984, in *IAU Symposium*, Vol. 108, *Structure and Evolution of the Magellanic Clouds*, van den Bergh S., de Boer K. S. D., eds., pp. 353–360
- Egan M. P. et al., 2003, *Air Force Research Laboratory Technical Report No. AFRL-VS-TR-2003-1589*
- Eisenhauer F. et al., 2003, in *Society of Photo-Optical Instrumentation Engineers (SPIE) Conference Series*, Vol. 4841, *Instrument Design and Performance for Optical/Infrared Ground-based Telescopes*, Iye M., Moorwood A. F. M., eds., p. 1548
- Ellingsen S. P., 2006, *ApJ*, 638, 241
- Fairlamb J. R., Oudmaijer R. D., Mendigutía I., Ilee J. D., van den Ancker M. E., 2015, *MNRAS*, 453, 976
- Galliano F., Madden S. C., Jones A. P., Wilson C. D., Bernard J.-P., Le Peintre F., 2003, *A&A*, 407, 159
- Gonzalez R. C., Woods R. E., 2002, *Digital image processing*. Prentice Hall
- Gordon K. D., Clayton G. C., Misselt K. A., Landolt A. U., Wolff M. J., 2003, *ApJ*, 594, 279
- Gordon K. D. et al., 2011, *AJ*, 142, 102
- Hanson M. M., Howarth I. D., Conti P. S., 1997, *ApJ*, 489, 698
- Helsel D. R., 2005, *Nondelects and Data Analysis; Statistics for censored environmental data*. John Wiley and Sons
- Henize K. G., 1956, *ApJS*, 2, 315
- Heydari-Malayeri M., Charmandaris V., Deharveng L., Rosa M. R., Zinnecker H., 1999, *A&A*, 347, 841
- Heydari-Malayeri M., Le Bertre T., Magain P., 1988, *A&A*, 195, 230
- Heydari-Malayeri M., Meynadier F., Charmandaris V., Deharveng L., Le Bertre T., Rosa M. R., Schaerer D., 2003, *A&A*, 411, 427
- Heydari-Malayeri M., Rosa M. R., Schaerer D., Martins F., Charmandaris V., 2002, *A&A*, 381, 951
- Hoare M. G., Kurtz S. E., Lizano S., Keto E., Hofner P., 2007, *Protostars and Planets V*, 181
- Kalari V. M., Vink J. S., 2015, *ApJ*, 800, 113
- Kewley L. J., Dopita M. A., Sutherland R. S., Heisler C. A., Trevena J., 2001, *ApJ*, 556, 121
- Kobulnicky H. A., Nordsieck K. H., Burgh E. B., Smith M. P., Percival J. W., Williams T. B., O’Donoghue D., 2003, in *Society of Photo-Optical Instrumentation Engineers (SPIE) Conference Series*, Vol. 4841, *Instrument Design and Performance for Optical/Infrared Ground-based Telescopes*, Iye M., Moorwood A. F. M., eds., pp. 1634–1644
- Koornneef J., Israel F. P., 1985, *ApJ*, 291, 156
- Kraus M., Krügel E., Thum C., Geballe T. R., 2000, *A&A*, 362, 158
- Krumholz M. R., Klein R. I., McKee C. F., 2012, *ApJ*, 754, 71
- Kudritzki R. P., 2002, *ApJ*, 577, 389
- Kuiper R., Yorke H. W., Turner N. J., 2015, *ApJ*, 800, 86
- Kurt C. M., Dufour R. J., Garnett D. R., Skillman E. D., Mathis J. S., Peimbert M., Torres-Peimbert S., Ruiz M.-T., 1999, *ApJ*, 518, 246
- Lanz T., Hubeny I., 2003, *ApJS*, 146, 417
- Lanz T., Hubeny I., 2007, *ApJS*, 169, 83
- Leroy A., Bolatto A., Stanimirovic S., Mizuno N., Israel F., Bot C., 2007, *ApJ*, 658, 1027
- Lindsay E. M., 1961, *AJ*, 66, 169
- Lumsden S. L., Hoare M. G., Urquhart J. S., Oudmaijer R. D., Davies B., Mottram J. C., Cooper H. D. B., Moore T. J. T., 2013, *ApJS*, 208, 11
- Madden S. C., Galliano F., Jones A. P., Sauvage M., 2006, *A&A*, 446, 877
- Martín-Hernández N. L., Peeters E., Tielens A. G. G. M., 2008, *A&A*, 489, 1189
- McGee R. X., Newton L. M., 1981, *Proc. Astron. Soc. Aust.*, 4, 189
- Menezes R. B., da Silva P., Ricci T. V., Steiner J. E., May D., Borges B. W., 2015, *MNRAS*, 450, 369
- Menezes R. B., Steiner J. E., Ricci T. V., 2014, *MNRAS*, 438, 2597
- Oliveira J. M. et al., 2013, *MNRAS*, 428, 3001
- Oliveira J. M., van Loon J. T., Stanimirović S., Zijlstra A. A., 2006, *MNRAS*, 372, 1509

Osterbrock D. E., Ferland G. J., 2006, *Astrophysics of gaseous nebulae and active galactic nuclei*

Peimbert M., Peimbert A., Ruiz M. T., 2000, *ApJ*, 541, 688

Porter J. M., Drew J. E., Lumsden S. L., 1998, *A&A*, 332, 999

Roche P. F., Aitken D. K., Smith C. H., 1987, *MNRAS*, 228, 269

Rubio M., Boulanger F., Rantakyro F., Contursi A., 2004, *A&A*, 425, L1

Scalise, Jr. E., Braz M. A., 1982, *AJ*, 87, 528

Seale J. P., Looney L. W., Chu Y.-H., Gruendl R. A., Brandl B., Chen C.-H. R., Brandner W., Blake G. A., 2009, *ApJ*, 699, 150

Sewilo M. et al., 2013, *ApJ*, 778, 15

Shull J. M., Hollenbach D. J., 1978, *ApJ*, 220, 525

Spezzi L., de Marchi G., Panagia N., Sicilia-Aguilar A., Ercolano B., 2012, *MNRAS*, 421, 78

Stanimirovic S., Staveley-Smith L., Dickey J. M., Sault R. J., Snowden S. L., 1999, *MNRAS*, 302, 417

Steiner J. E., Menezes R. B., Ricci T. V., Oliveira A. S., 2009, *MNRAS*, 395, 64

Tanaka K. E. I., Tan J. C., Zhang Y., 2015, *ArXiv e-prints*

Testor G., Lemaire J. L., Field D., 2003, *A&A*, 407, 905

Testor G., Lemaire J. L., Field D., Callejo G., 2005, *A&A*, 434, 497

Testor G., Lemaire J. L., Heydari-Malayeri M., Kristensen L. E., Diana S., Field D., 2010, *A&A*, 510, A95

Testor G., Pakull M., 1985, *A&A*, 145, 170

van Loon J. T., 2012, *ArXiv e-prints*, 1210.0983

van Loon J. T., Cohen M., Oliveira J. M., Matsuura M., McDonald I., Sloan G. C., Wood P. R., Zijlstra A. A., 2008, *A&A*, 487, 1055

van Loon J. T., Oliveira J. M., Gordon K. D., Sloan G. C., Engelbracht C. W., 2010, *AJ*, 139, 1553

Ward J. L., Oliveira J. M., van Loon J. T., Sewilo M., 2016, *MNRAS*, 455, 2345

Wheelwright H. E., Oudmaijer R. D., de Wit W. J., Hoare M. G., Lumsden S. L., Urquhart J. S., 2010, *MNRAS*, 408, 1840

Wong G. F. et al., 2012, *Serbian Astron. J.*, 184, 93

Wong G. F., Filipovic M. D., Crawford E. J., de Horta A. Y., Galvin T., Draskovic D., Payne J. L., 2011a, *Serbian Astron. J.*, 182, 43

Wong G. F. et al., 2011b, *Serbian Astron. J.*, 183, 103

Woods P. M. et al., 2011, *MNRAS*, 411, 1597

Zinnecker H., Yorke H. W., 2007, *ARA&A*, 45, 481

APPENDIX A: CONTINUUM IMAGES

Fig A1 shows the continuum images for all sources observed with SINFONI with the exception of source #25 (see Section 3.1 for details). Marked on the images are the positions of all *K*-band continuum sources identified in this work.

APPENDIX B: EXTRACTED *K*-BAND AND OPTICAL SPECTRA

Figure B1 shows the normalised *K*-band extracted spectra for all of the sources marked in Fig. A1 with the positions of the emission lines of interest marked. A number of sky line

residuals remain visible in many of the spectra; the positions of these are given in Ward et al. (2016). Figures B2, B3 and B4 show the optical spectra obtained with RSS at SALT for N81 and N88 A. Note that a logarithmic flux scale has been used for clarity. Emission lines of interest are marked on these spectra.

APPENDIX C: EMISSION LINE FLUXES

Tables C1 and C2 give the measured emission line fluxes for all spectra. Those for the *K*-band spectra are presented in Table C1 and those for the optical spectra are presented in Table C2. “p” indicates that an emission line is present but that a measurement cannot be obtained and “?” indicates a significant uncertainty in the identification of the emission line.

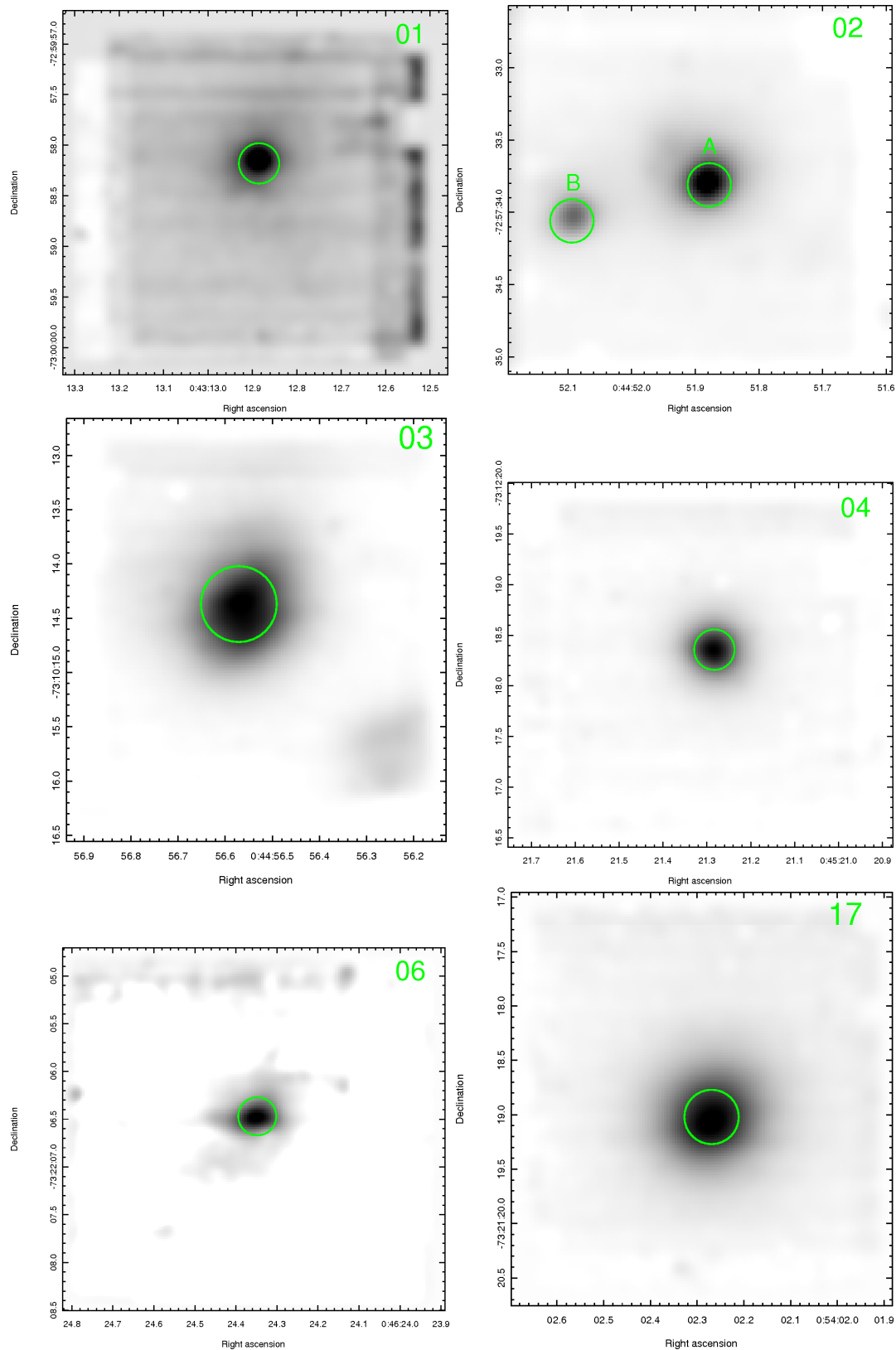


Figure A1. SINFONI *K*-band continuum images for all observed FOVs.

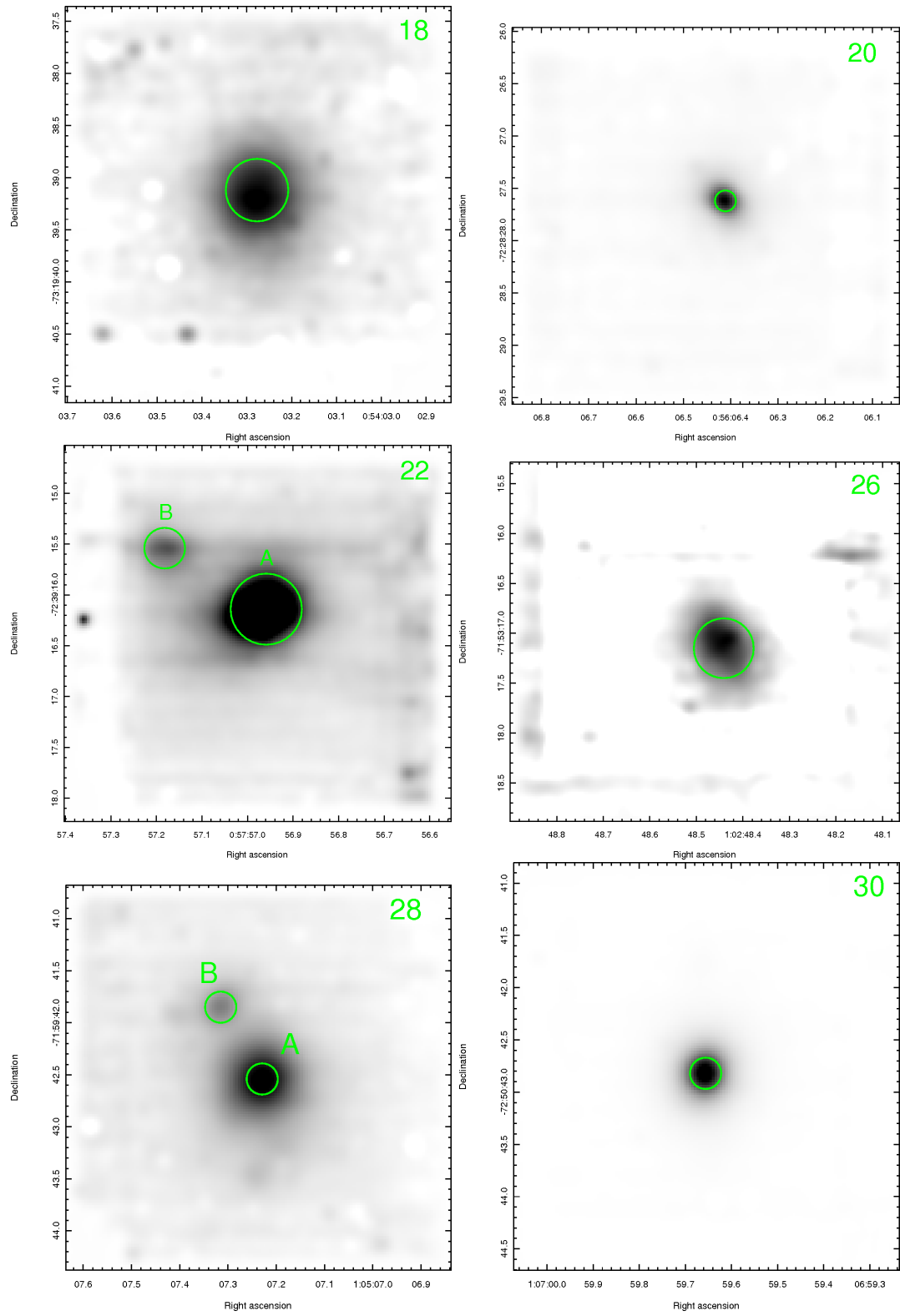


Fig. A1 cont. SINFONI *K*-band continuum images for all observed FOVs.

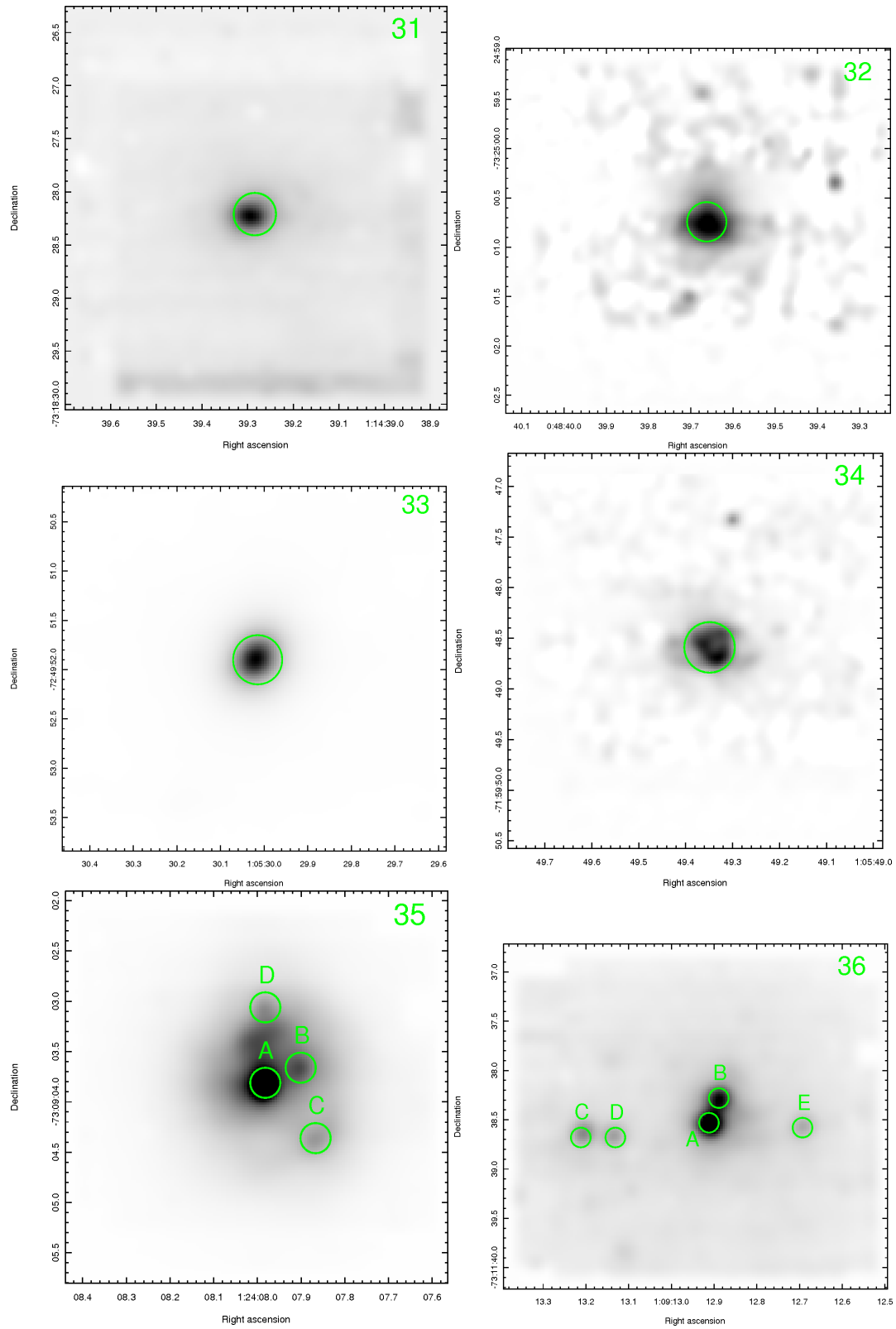


Fig. A1 cont. SINFONI *K*-band continuum images for all observed FOVs.

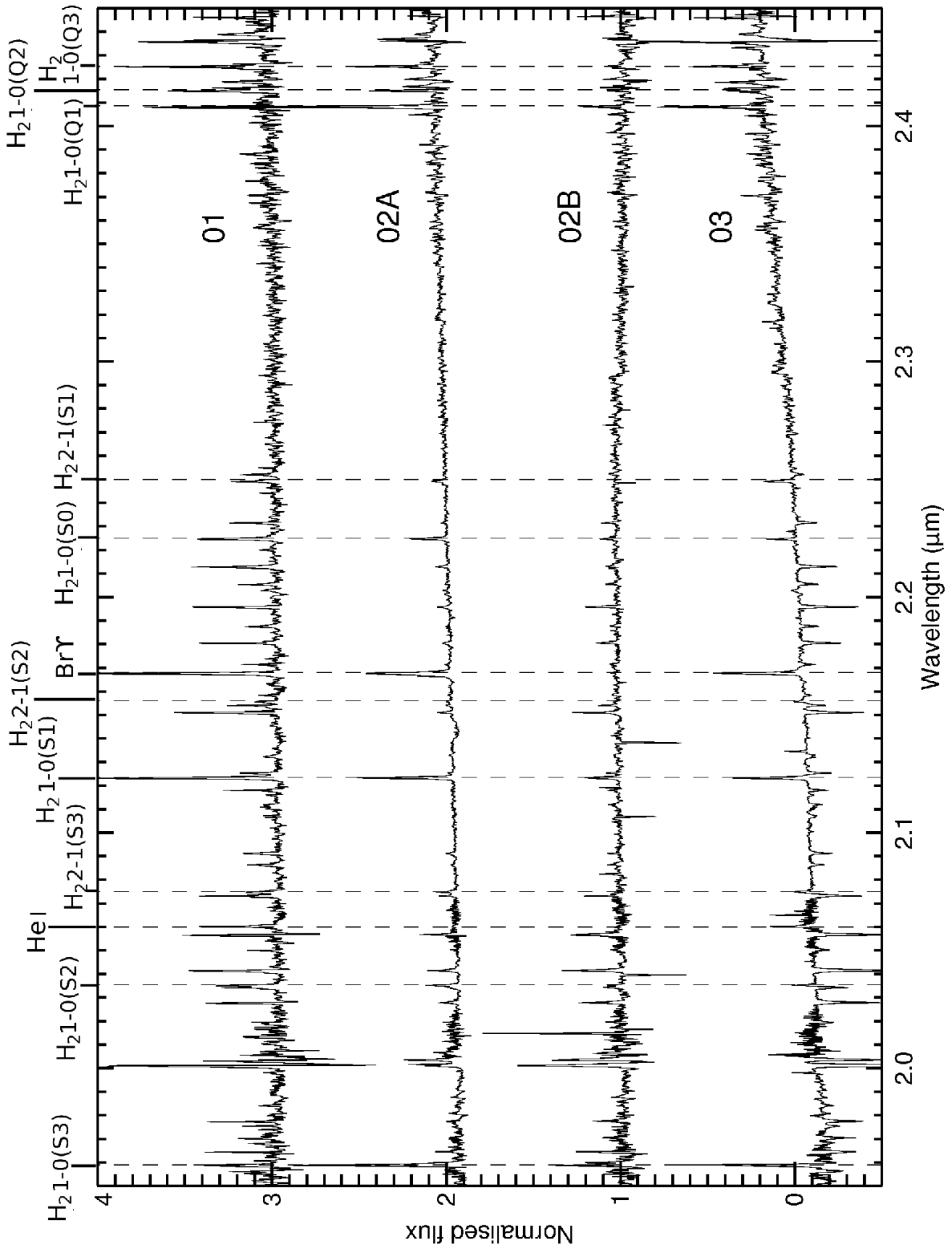


Figure B1. Continuum normalised extracted spectra towards all *K*-band continuum sources detected. Positions of the emission lines studied in this work are marked.

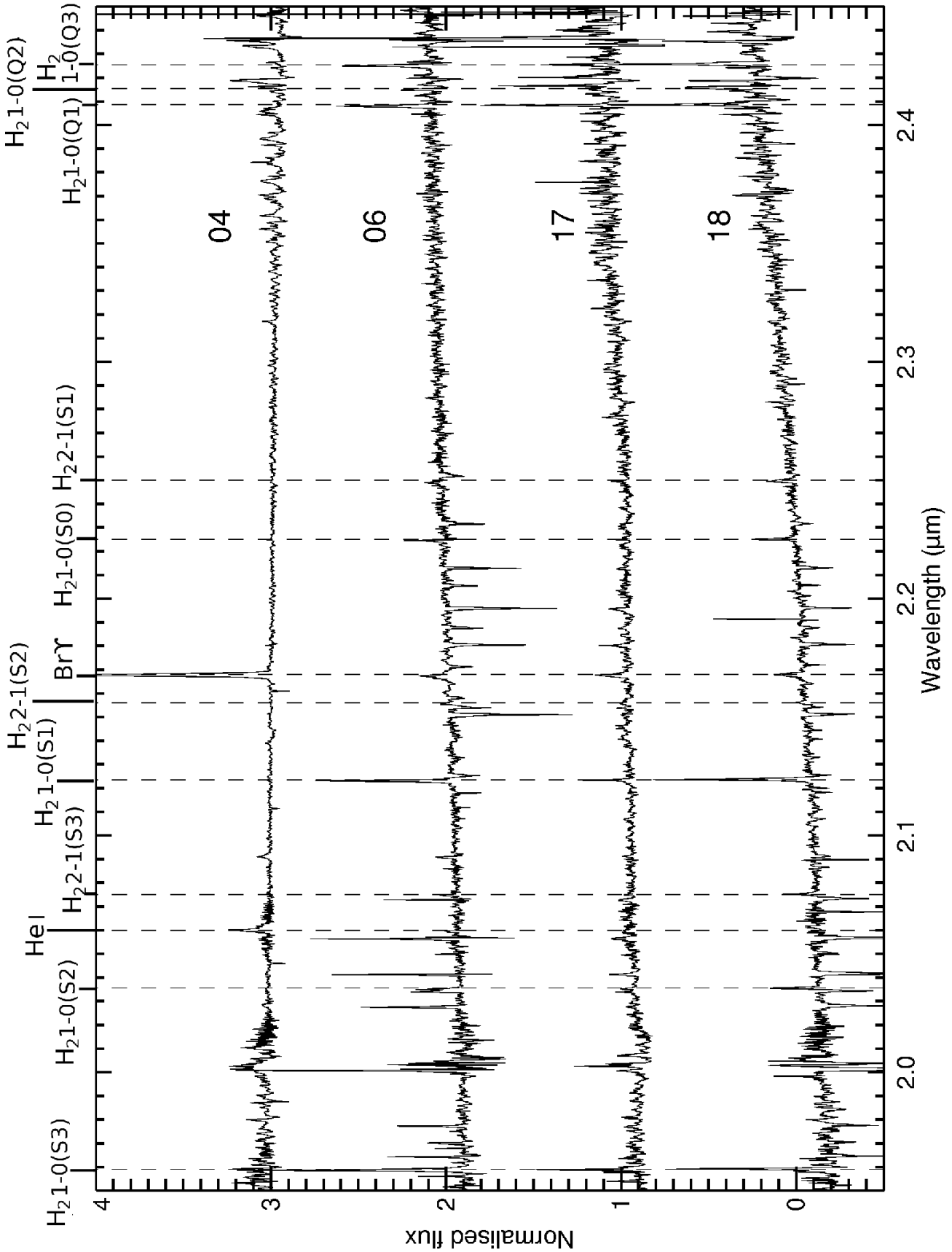


Fig. B1 cont. Extracted K-band spectra.

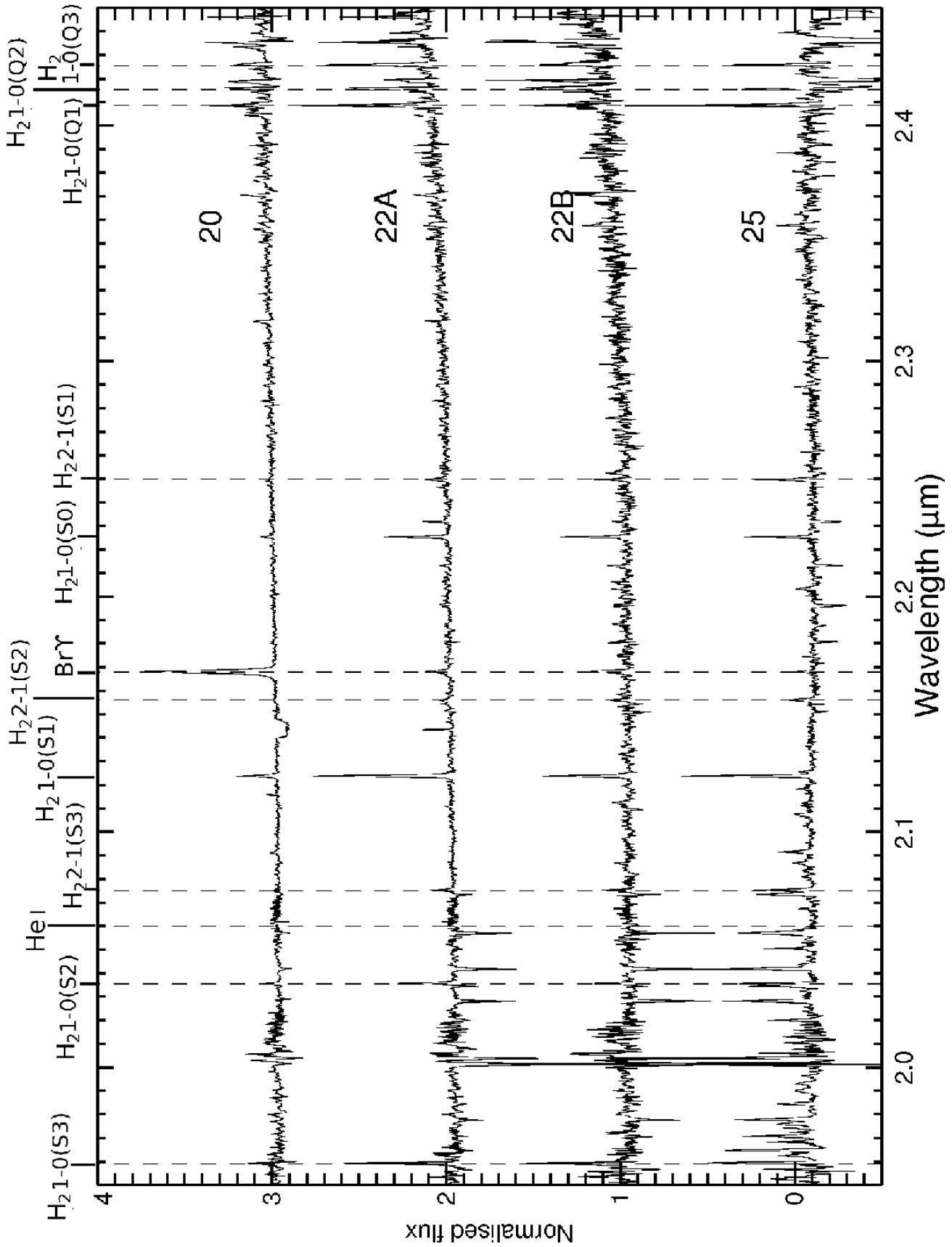


Fig. B1 cont. Extracted K-band spectra.

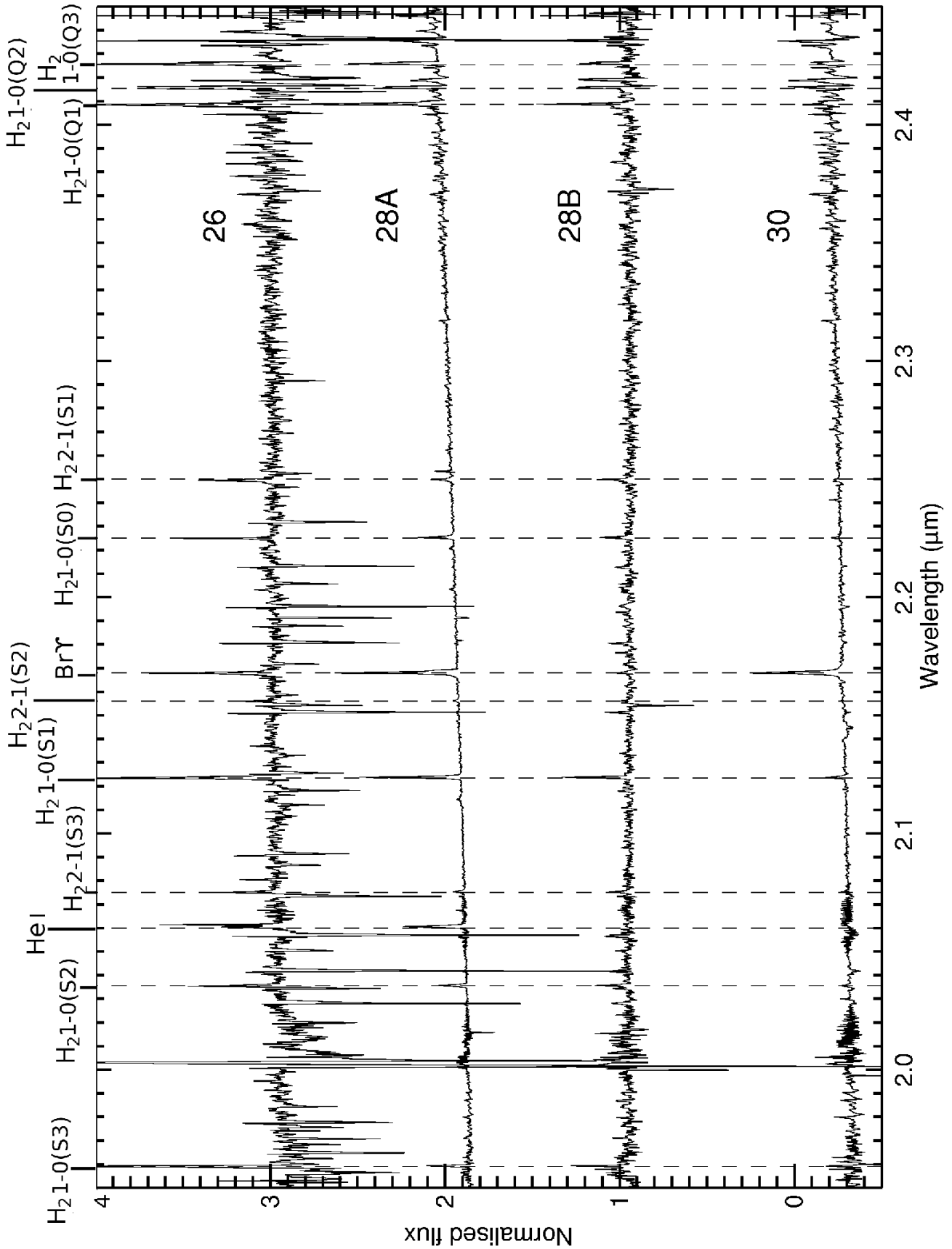


Fig. B1 cont. Extracted K-band spectra.

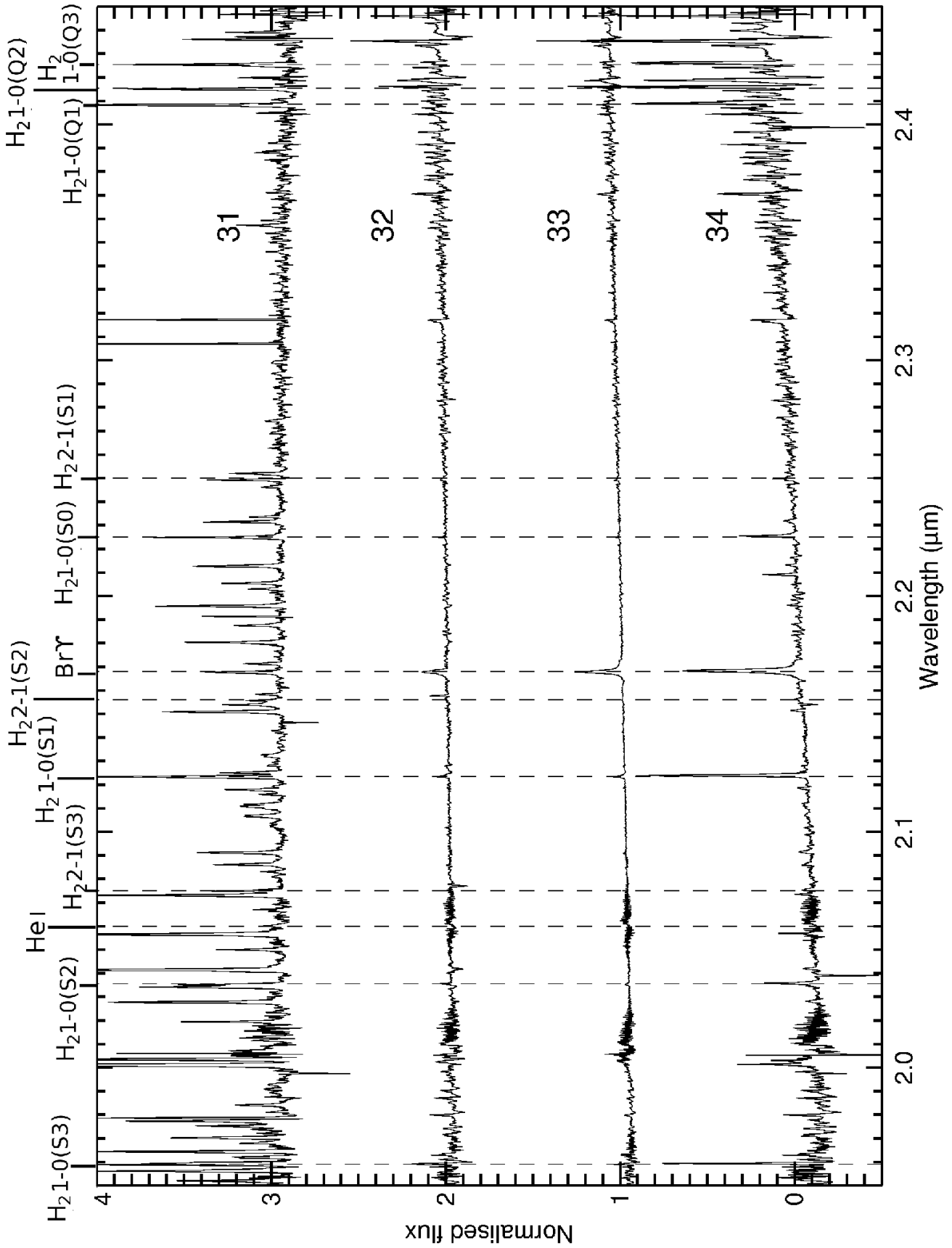


Fig. B1 cont. Extracted K-band spectra.

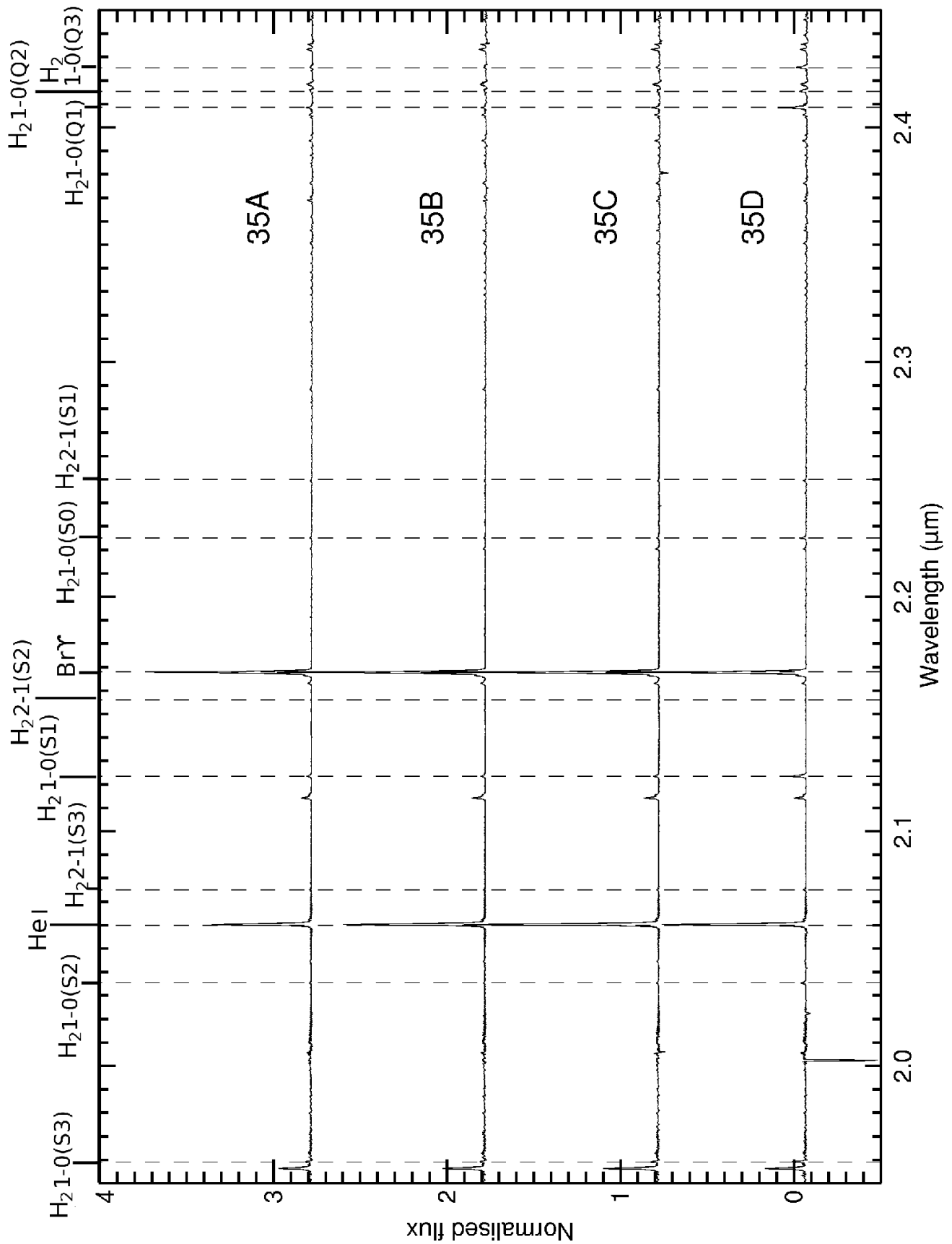


Fig. B1 cont. Extracted K-band spectra.

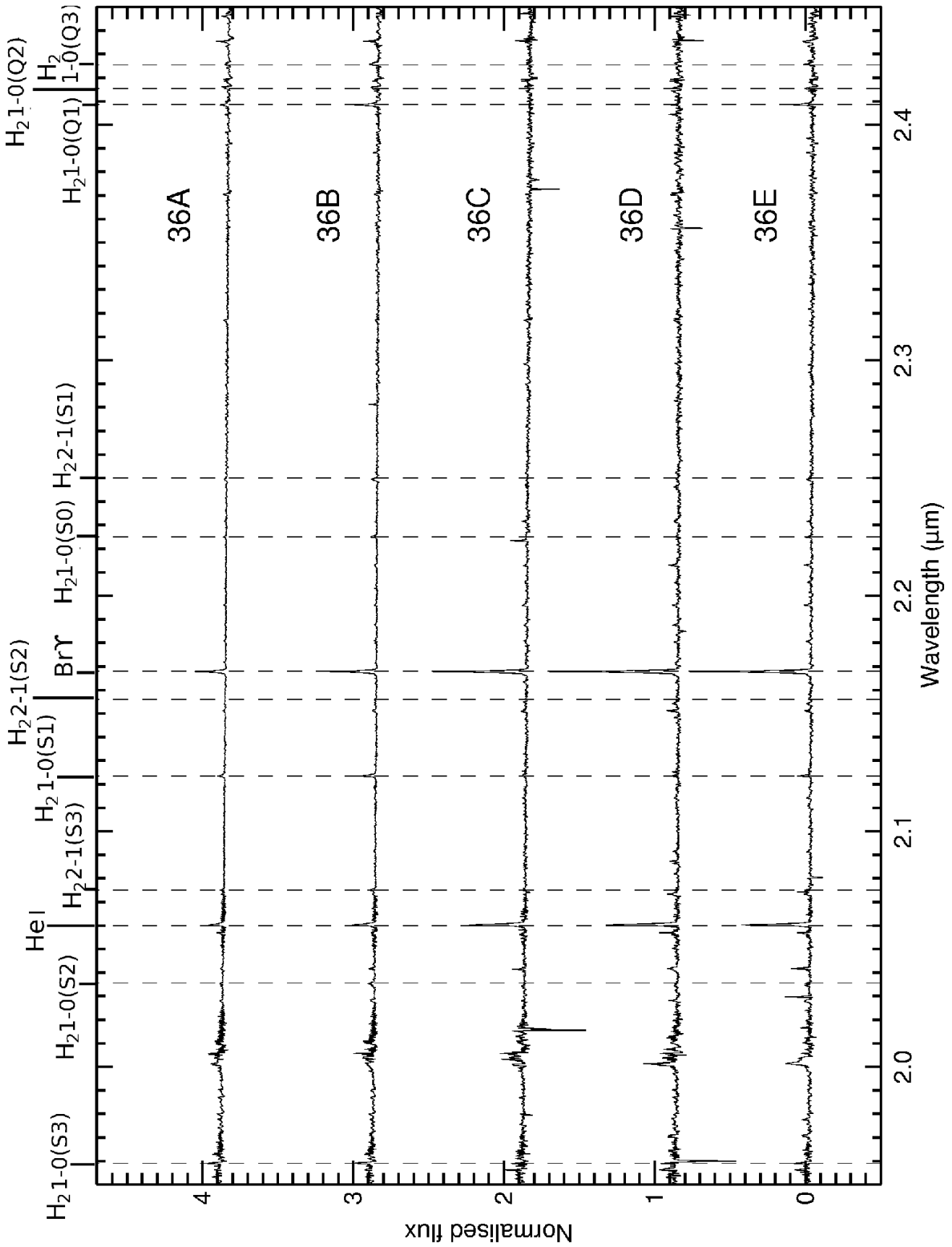


Fig. B1 cont. Extracted K-band spectra.

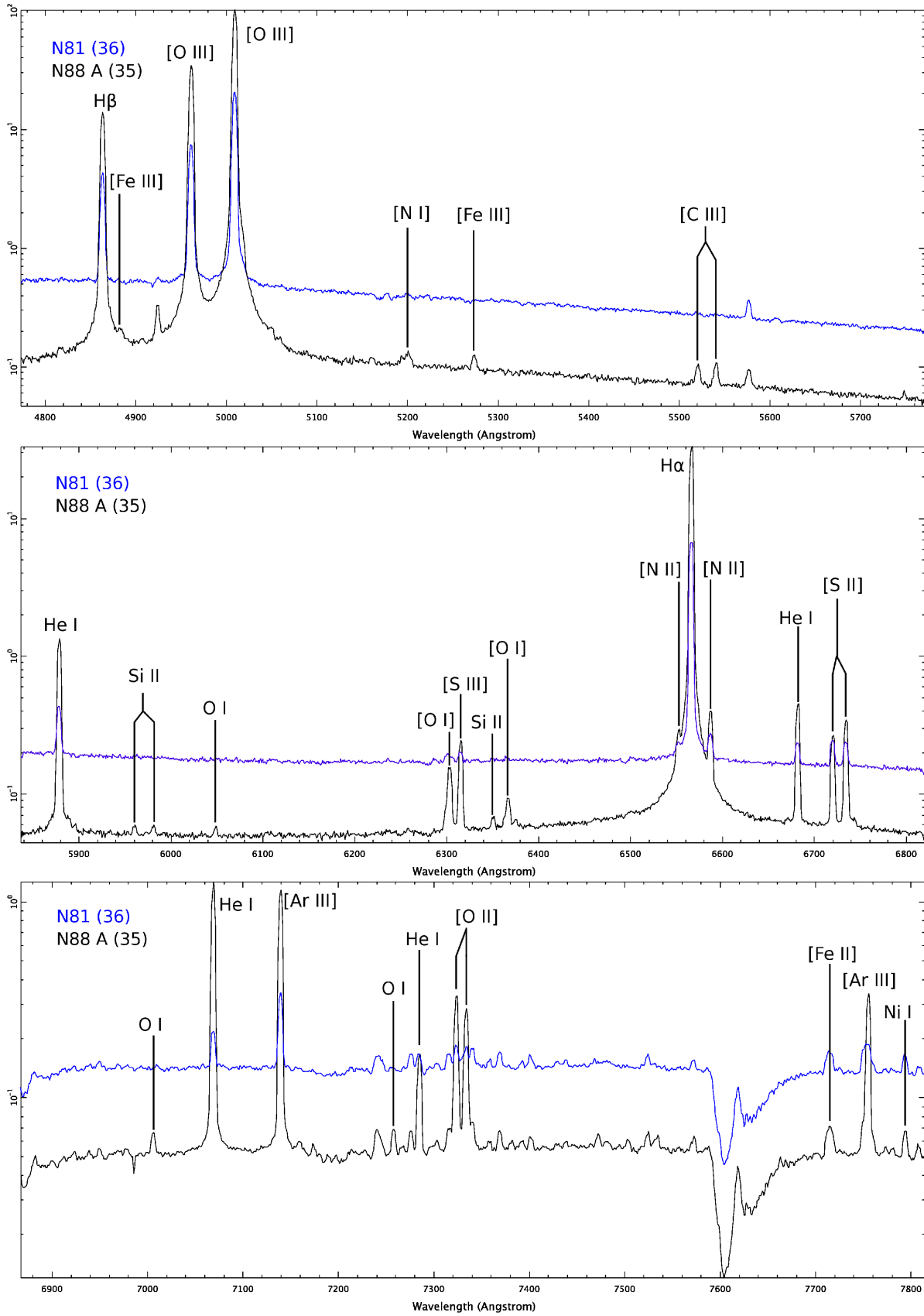


Figure B2. Low resolution optical spectra of sources 35 and 36 (N88 A and N81, respectively)

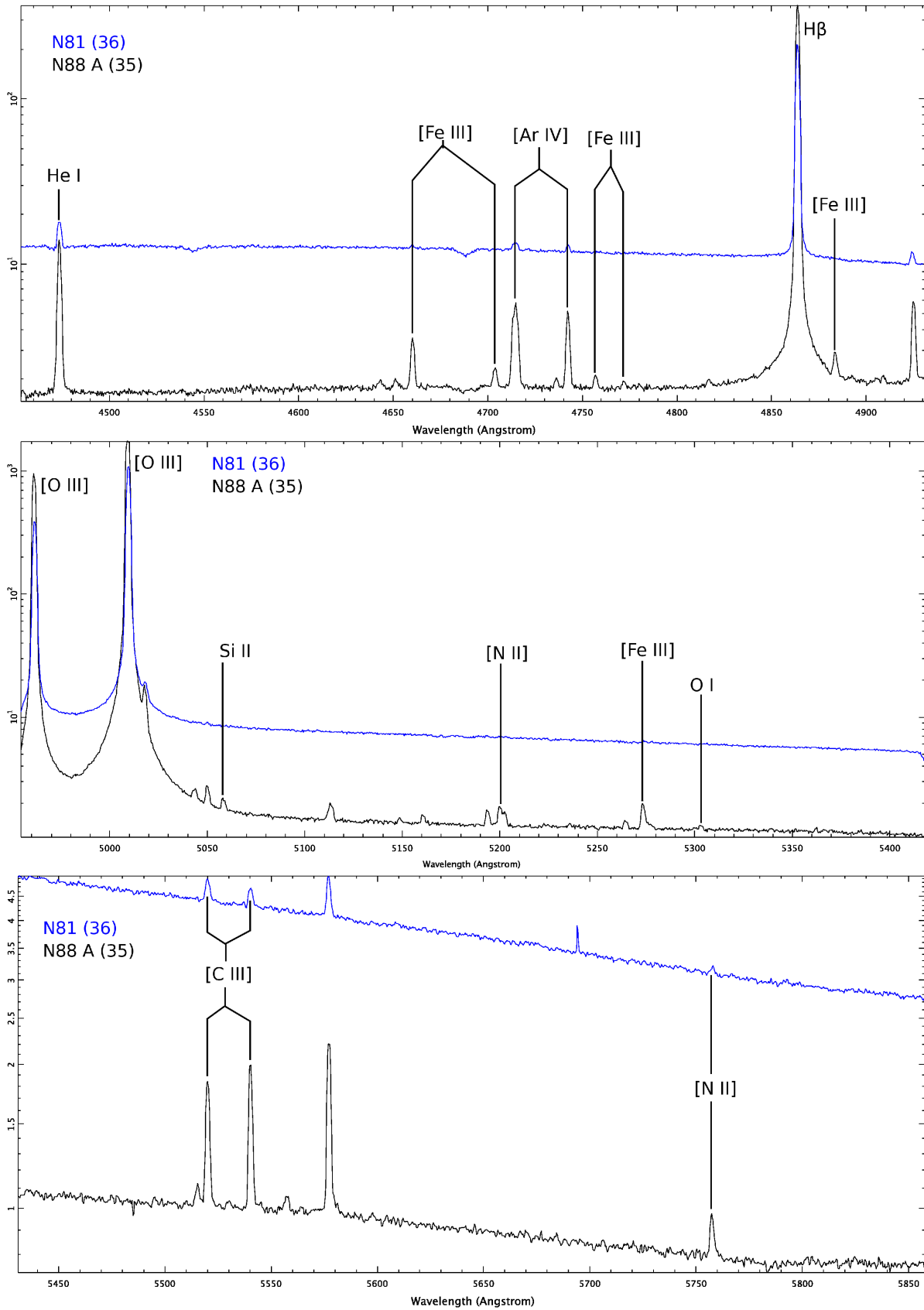


Figure B3. Medium resolution blue optical spectra of sources 35 and 36 (N88 A and N81, respectively)

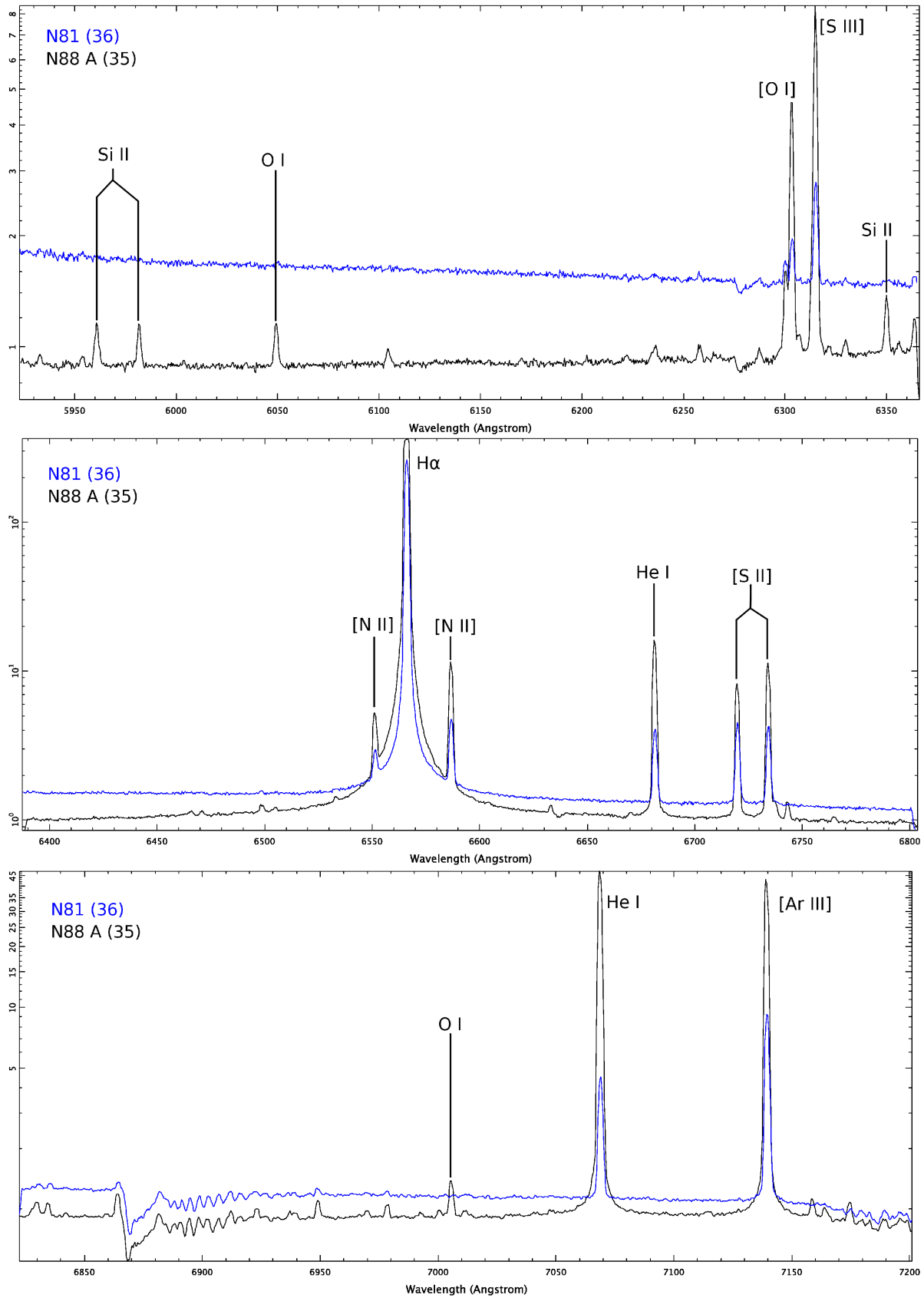


Figure B4. Medium resolution red optical spectra of sources 35 and 36 (N88 A and N81, respectively)

Table C1. K-band emission line fluxes measured towards all sources. The fluxes have not been corrected for extinction.

Source	He I (2.058 μ m) 10^{-19} W/m ²	Br γ 10^{-19} W/m ²	H ₂ 1-0(S0) 10^{-19} W/m ²	H ₂ 1-0(S1) 10^{-19} W/m ²	H ₂ 1-0(S2) 10^{-19} W/m ²	H ₂ 1-0(S3) 10^{-19} W/m ²
01	1.6 \pm 0.2	5.3 \pm 0.3	2.2 \pm 0.2	4.4 \pm 0.3	1.9 \pm 0.3	2.4 \pm 0.4
02 A		9.8 \pm 0.6	2.3 \pm 0.2	6.1 \pm 0.4	2.2 \pm 0.4	11 \pm 1
02 B			0.7 \pm 0.2	1.18 \pm 0.07	0.4 \pm 0.1	1.8 \pm 0.4
03	5.5 \pm 1.3	16.2 \pm 1.2	2.8 \pm 0.3	11.1 \pm 0.9	2.5 \pm 0.8	20 \pm 3
04	6.3 \pm 1.0	36.2 \pm 0.8				
06		0.41 \pm 0.06	0.14 \pm 0.04	0.92 \pm 0.06	0.32 \pm 0.08	1.4 \pm 0.1
17		2.0 \pm 0.1		1.2 \pm 0.2	0.4 \pm 0.2	2.4 \pm 0.4
18		0.93 \pm 0.09	0.71 \pm 0.05	2.4 \pm 0.2	0.8 \pm 0.2	2.0 \pm 0.4
20		8.1 \pm 0.2	3.0 \pm 0.4	1.1 \pm 0.1	0.40 \pm 0.08	0.8 \pm 0.3
22 A		1.3 \pm 0.1	1.86 \pm 0.09	4.5 \pm 0.2	1.7 \pm 0.2	2.9 \pm 0.2
22 B		0.46 \pm 0.05	0.43 \pm 0.04	0.60 \pm 0.04	0.19 \pm 0.05	0.8 \pm 0.1
25		0.33 \pm 0.06	1.05 \pm 0.09	2.4 \pm 0.2		
26	0.9 \pm 0.2	2.3 \pm 0.2	1.0 \pm 0.1	3.9 \pm 0.4	1.1 \pm 0.5	3.6 \pm 0.6
28 A	6.4 \pm 0.4	13.8 \pm 1.0	3.0 \pm 0.3	8.6 \pm 0.7	2.6 \pm 0.2	3.6 \pm 0.4
28 B		0.09 \pm 0.03	0.25 \pm 0.03	0.43 \pm 0.03	0.19 \pm 0.07	0.3 \pm 0.1
30		15.3 \pm 0.7	0.77 \pm 0.09	2.3 \pm 0.3	0.8 \pm 0.2	2.3 \pm 1.1
31	1.0 \pm 0.4	5.9 \pm 0.4	7.4 \pm 0.6	15 \pm 1	7 \pm 1	16 \pm 4
32		5.2 \pm 0.4	0.44 \pm 0.06	1.3 \pm 0.2	0.68 \pm 0.05	3.6 \pm 0.9
33		158 \pm 9	6.5 \pm 0.9	21 \pm 2	5 \pm 1	p?
34		20 \pm 1	4.2 \pm 0.3	13.6 \pm 0.8	4.4 \pm 0.5	9 \pm 1
35 A	197 \pm 9	326 \pm 18	2.9 \pm 0.3	7.7 \pm 0.8	2.3 \pm 0.2	7 \pm 3
35 B	91 \pm 5	138 \pm 10	0.7 \pm 0.2	2.2 \pm 0.4	0.5 \pm 0.1	2.0 \pm 0.7
35 C	100 \pm 6	127 \pm 10	0.9 \pm 0.2	2.3 \pm 0.3	1.0 \pm 0.3	2.8 \pm 0.8
35 D	68 \pm 4	98 \pm 9	2.7 \pm 0.3	7.2 \pm 0.8	2.0 \pm 0.2	5.4 \pm 1.0
36 A	3.1 \pm 0.5	6.3 \pm 0.3	0.4 \pm 0.1	1.5 \pm 0.2	0.55 \pm 0.06	1.7 \pm 0.9
36 B	3.0 \pm 0.3	6.1 \pm 0.3	0.85 \pm 0.07	1.9 \pm 0.2	0.27 \pm 0.07	1.6 \pm 0.4
36 C	4.1 \pm 0.4	6.8 \pm 0.4				p
36 D	3.6 \pm 0.3	6.2 \pm 0.4		0.27 \pm 0.04		0.39 \pm 0.09
36 E	4.4 \pm 0.4	8.2 \pm 0.7	0.32 \pm 0.06	0.72 \pm 0.07		0.6 \pm 0.2
Source	H ₂ 2-1(S1) 10^{-19} W/m ²	H ₂ 2-1(S2) 10^{-19} W/m ²	H ₂ 2-1(S3) 10^{-19} W/m ²	1-0Q(1) 10^{-19} W/m ²	1-0Q(2) 10^{-19} W/m ²	1-0Q(3) 10^{-19} W/m ²
01	0.9 \pm 0.2	0.7 \pm 0.1	1.5 \pm 0.6	2.7 \pm 0.5	2.2 \pm 0.4	3.3 \pm 0.6
02 A	0.8 \pm 0.1	p	1.1 \pm 0.4	14 \pm 1	2.7 \pm 0.4	5.2 \pm 0.8
02 B		0.2 \pm 0.1		1.5 \pm 0.3		0.9 \pm 0.3
03	3.1 \pm 0.4	1.2 \pm 0.3	2.4 \pm 0.6	15 \pm 2		10 \pm 2
04						
06	0.11 \pm 0.05	<1.0	0.08 \pm 0.03	0.76 \pm 0.09	0.23 \pm 0.06	0.75 \pm 0.08
17	p?			3.0 \pm 0.5	2.2 \pm 0.6	2.2 \pm 0.3
18	0.52 \pm 0.09	0.18 \pm 0.03	0.4 \pm 0.1	2.6 \pm 0.5	2.2 \pm 0.6	2.5 \pm 0.4
20				1.7 \pm 0.3	?	1.2 \pm 0.3
22 A	0.91 \pm 0.09	0.6 \pm 0.1	0.51 \pm 0.08	4.7 \pm 0.6	3.8 \pm 0.7	3.9 \pm 0.4
22 B	0.21 \pm 0.03	0.17 \pm 0.03	0.12 \pm 0.04	0.6 \pm 0.1	1.0 \pm 0.2	0.7 \pm 0.2
25	1.1 \pm 0.1	?	?	?	?	1.3 \pm 0.3
26	1.1 \pm 0.2	0.42 \pm 0.05	0.7 \pm 0.1	4.7 \pm 0.8	3.6 \pm 1.5	3.7 \pm 1.0
28 A	1.6 \pm 0.2	0.44 \pm 0.05	1.0 \pm 0.2	14 \pm 2	7 \pm 1	9 \pm 1
28 B	0.21 \pm 0.05		0.12 \pm 0.02	0.7 \pm 0.2	0.5 \pm 0.1	0.5 \pm 0.1
30				3.0 \pm 0.9	4 \pm 2	2 \pm 1
31	3.6 \pm 0.4	2.0 \pm 0.5	4.3 \pm 0.8	16 \pm 1	9.4 \pm 0.8	11 \pm 1
32						1.4 \pm 0.5
33	p?			14 \pm 4	p	13 \pm 2
34	1.8 \pm 0.4	1.4 \pm 0.4		13 \pm 3	14 \pm 3	13 \pm 2
35 A	2.6 \pm 0.3	0.9 \pm 0.3	1.5 \pm 0.5	11 \pm 2	7 \pm 3	6 \pm 2
35 B	0.70 \pm 0.09	0.18 \pm 0.08	p?	2.8 \pm 0.5	2.1 \pm 0.8	1.4 \pm 0.5
35 C	0.8 \pm 0.1	0.22 \pm 0.06	0.7 \pm 0.2	3.8 \pm 0.5	2.0 \pm 0.8	1.7 \pm 0.4
35 D	1.2 \pm 0.1	0.43 \pm 0.06	0.9 \pm 0.2	?	?	5.0 \pm 0.7
36 A	0.6 \pm 0.1		p?	1.9 \pm 0.4	1.3 \pm 0.6	0.9 \pm 0.5
36 B	0.8 \pm 0.1	0.27 \pm 0.07	0.6 \pm 0.1	3.2 \pm 0.5	1.5 \pm 0.5	1.7 \pm 0.4
36 C	0.29 \pm 0.06	p?	0.14 \pm 0.03	?	?	0.26 \pm 0.09
36 D				0.5 \pm 0.1	?	0.4 \pm 0.1
36 E				1.4 \pm 0.2	0.6 \pm 0.3	0.8 \pm 0.3
Source	Pf 20-5 10^{-19} W/m ²	Pf 21-5 10^{-19} W/m ²	Pf 22-5 10^{-19} W/m ²	Pf 23-5 10^{-19} W/m ²	Pf 24-5 10^{-19} W/m ²	Pf 25-5 10^{-19} W/m ²
35 A	9.7 \pm 0.6	?	5.5 \pm 0.7	5.6 \pm 0.9	3.5 \pm 1.8	6.3 \pm 0.7
35 B	4.1 \pm 0.4	5.2 \pm 1.0	2.6 \pm 0.3	2.6 \pm 0.4	1.4 \pm 0.4	2.5 \pm 0.3
35 C	3.8 \pm 0.3	4.2 \pm 0.4	2.4 \pm 0.4	2.3 \pm 0.4	1.4 \pm 0.3	2.0 \pm 0.4
35 D	3.1 \pm 0.3	4.3 \pm 1.1	1.7 \pm 0.4	1.9 \pm 0.2	7.3 \pm 0.7	1.7 \pm 0.2

Table C2. Optical emission line fluxes. Fluxes have not been corrected for extinction.

Source	H α	H β	H γ 10^{-13} erg s $^{-1}$ cm $^{-2}$	H δ 10^{-13} erg s $^{-1}$ cm $^{-2}$	H η	He I 3888 Å	He I 4464 Å
01	1.77±0.03	0.382±0.003	0.160±0.005	0.084±0.005	0.044±0.004		
02	0.072±0.003						
03	7.8±0.2	2.0±0.1	0.73±0.05	0.32±0.02	0.18±0.03	0.16±0.03	
04	1.86±0.1	0.241±0.001	0.0732±0.0008	0.030±0.003			
07	0.21±0.01	0.040±0.006					
08	0.62±0.02	0.149±0.008	0.057±0.008	0.033±0.005			
09	4.3±0.1	1.26±0.04	0.53±0.04	0.24±0.01			
10	0.050±0.009			0.02±0.01			
11	0.06±0.02						
12	0.14±0.01	0.037±0.009					
13	1.05±0.08	0.157±0.007	0.054±0.009	0.011±0.006			
14	0.28±0.04						
15	0.90±0.05	0.237±0.007	0.102±0.008	0.05±0.01	0.029±0.006	0.037±0.006	
16	0.21±0.02						
17	0.038±0.005						
18	0.07±0.02						
20	1.8±0.3	0.28±0.07		p?			
21	0.43±0.02	0.060±0.006	0.018±0.004				
22	0.54±0.04	0.19±0.01	0.07±0.01	0.024±0.004			
23	0.055±0.006						
25	1.18±0.02	0.35±0.02	0.12±0.02				
26	6.1±0.3	2.6±0.2	0.82±0.04	0.41±0.07	0.27±0.03	0.33±0.06	
27	0.07±0.01						
28	0.90±0.05	0.24±0.02	0.081±0.006	0.03±0.01			
30	0.36±0.02	0.054±0.005	0.013±0.005				
32	0.21±0.04						
33	0.20±0.07						
34	0.082±0.007			p?			
35	97±6	44±4					
36	19±1	11.9±0.3					
Source	He I 5876 Å	He I 6679 Å	He I 7066 Å 10^{-13} erg s $^{-1}$ cm $^{-2}$	[N II] 6548 Å 10^{-13} erg s $^{-1}$ cm $^{-2}$	[N II] 6584 Å	[S II] 6717 Å	[S II] 6731 Å
01				0.049±0.003	0.160±0.004	0.12±0.07	0.119±0.003
02							
03	1.14±0.02	0.033±0.004		0.19±0.02	0.62±0.01	0.4±0.1	0.38±0.03
04						0.04±0.01	0.028±0.002
07					0.023±0.009	0.021±0.004	0.020±0.001
08	0.02±0.01	0.009±0.003	0.005±0.002	0.009±0.004	0.036±0.005	0.03±0.02	0.025±0.002
09				0.13±0.02	0.43±0.03	0.35±0.09	0.30±0.02
12					0.018±0.003	0.024±0.003	0.016±0.003
13				0.014±0.005	0.065±0.008	0.04±0.01	0.044±0.006
15		0.005±0.003		0.014±0.007	0.062±0.006	0.063±0.009	0.05±0.01
16					0.009±0.003		
21					0.033±0.006	0.012±0.003	0.017±0.002
22						0.04±0.01	0.033±0.009
23							0.002±0.001
25				0.036±0.006	0.097±0.007	0.14±0.01	0.105±0.008
26	0.31±0.01	0.073±0.009	0.063±0.007		0.159±0.008	0.20±0.01	0.16±0.02
27				0.006±0.003	0.007±0.003	0.019±0.002	0.015±0.003
28	0.015±0.005	0.0027±0.0009		0.025±0.006	0.060±0.007	0.07±0.01	0.07±0.01
34							0.002±0.001
35	3.8±0.4		3.5±0.4	0.42±0.03	1.11±0.06	0.68±0.04	0.94±0.06
36			0.23±0.01	0.32±0.05	0.35±0.03	0.27±0.03	0.27±0.03
Source	[O II] 7319/7319 Å	[O II] 7330/7331 Å	[O III] 4959 Å 10^{-13} erg s $^{-1}$ cm $^{-2}$	[O III] 5007 Å 10^{-13} erg s $^{-1}$ cm $^{-2}$	[Ne III] 3869 Å	[Ar III] 7136 Å	[Ar III] 7751 Å
01	0.031±0.006						
03	0.16±0.06		0.45±0.01	1.28±0.06		0.095±0.001	0.028±0.005
08	0.021±0.004		0.054±0.008	0.19±0.01		0.010±0.003	
09	0.07±0.02						
12				0.027±0.005			
13	0.030±0.003		0.014±0.006	0.018±0.005	0.03±0.02		
15							
17							
21							
22							
25							
26							
27							
28							
34							
35	0.95±0.05	0.79±0.03	110±10	330±20		3.3±0.4	9.3±0.1
36	0.14±0.01	0.21±0.06	22.4±0.5	65±1		0.61±0.03	0.32±0.02